UNIVERSITY OF SOUTHAMPTON

Communication Applications in Silicon Waveguides

by

Iosif Demirtzioglou

Thesis for the degree of Doctor of Philosophy

in the
Faculty of Engineering and Physical Sciences
Optoelectronics Research Centre

March 2020

UNIVERSITY OF SOUTHAMPTON

ABSTRACT

FACULTY OF ENGINEERING AND PHYSICAL SCIENCES
Optoelectronics Research Centre

Doctor of Philosophy

Communication Applications in Silicon Waveguides

by Iosif Demirtzioglou

The adoption of silicon photonic technology in optical communication networks is now a commercial reality, with silicon transceiver products being incorporated into data centres. Photonic circuits fabricated on the Silicon-on-Insulator (SOI) platform enjoy the benefit of design scalability, by leveraging the immense infrastructure of the microelectronics industry that offers high production yield at low cost. This PhD project was aimed at investigating and developing a number of integrated components that perform key functionalities in communications. In particular, the reported devices cover chip-to-fibre grating couplers, electro-optic modulators and nonlinear waveguide elements, which are studied in various stages of their development cycle.

The first component reported in this thesis is a novel silicon grating coupler device that was simulated and fabricated in order to operate as a mode order converter. Coupling of the fundamental waveguide mode to a higher-order Linearly Polarised (LP_{11}) mode of a commercial two-mode fibre is successfully demonstrated to verify its operation.

The second topic that is investigated relates to electro-optic silicon modulators and their capabilities in two different applications. First, an analytic model is developed for the behaviour of a Ring Resonator Modulator (RRM) as a frequency comb generator and the concept is experimentally implemented on a fabricated device that produces a five-line comb. The second device that is studied is a linear Mach–Zehnder Modulator (MZM) that is characterised and used for data transmission in medium-reach links using Pulse Amplitude Modulation and Discrete Multitone formats (PAM-4 and DMT), while improvements of the topology in terms of linearity are theoretically studied.

The last topic of this thesis relates to the application of nonlinear silicon waveguides in all-optical signal processing. Wavelength conversion of a complex optical signal through Four-Wave Mixing in such a structure is demonstrated, while an improved design for an integrated wavelength converter device is proposed.

Contents

List of Figures

List of Tables

Nomenclature

AC	Alternating Current
ADC	Analog-to-Digital Converter
ASE	Amplified Spontaneous Emission
AWG	Arbitrary Waveform Generator
BER	Bit Error Ratio
BOX	Buried Oxide Layer
CD	Chromatic Dispersion
CMOS	Complementary Metal-Oxide-Semiconductor
CP	Cyclic Prefix
CW	Continuous Wave
DAC	Digital-to-Analog Converter
DC	Direct Current
DD	Direct Detection
DFB	Distributed Feedback
DMT	Discrete MultiTone
DUV	Deep Ultraviolet
ECL	External Cavity Laser
EDFA	Erbium-Doped Fibre Amplifier
E/O	Electro-optic
FCA	Free Carrier Absorption
FCD	Free Carrier Dispersion
FDTD	Finite Difference Time Domain
FFT	Fast Fourier Transform
FMF	Few-Mode Fibre
FSR	Free Spectral Range
FWHM	Full-Width at Half-Maximum
FWM	Four-Wave Mixing
GC	Grating Coupler
GSG	Ground-Signal-Ground
GSGSG	Ground-Signal-Ground-Signal-Ground
GVD	Group Velocity Dispersion
HD2	2nd-order Harmonic Distortion

HD3	3rd-order Harmonic Distortion
HD-FEC	Hard Decision - Forward Error Correction
HPC	High-Performance Computing
IFFT	Inverse Fast Fourier Transform
IIP	Input Intercept Point
IM	Intensity Modulated
IMD2	2nd-order Intermodulation Distortion
IMD3	3rd-order Intermodulation Distortion
ICP	Inductively Coupled Plasma
I/O	Input / Output
IR	Infra-Red
LHS	Left Hand Side
LP	Linearly Polarised
LTI	Linear and Time Invariant
MEMS	MicroElectroMechanical Systems
MFD	Mode Field Diameter
MMF	Multi-Mode Fibre
MMI	Multi-Mode Interference
MPW	Multi-Project Wafer
MZI	Mach–Zehnder Interferometer
MZM	Mach–Zehnder Modulator
NLSE	Non-Linear Schrodinger Equation
OFDM	Orthogonal Frequency Division Multiplexing
OIP	Output Intercept Point
OMA	Optical Modulation Analyser
OOK	On-Off Keying
OSA	Optical Spectrum Analyser
OSNR	Optical Signal to Noise Ratio
PAM	Pulse Amplitude Modulation
PAPR	Peak-to-Average Power Ratio
PCB	Printed Circuit Board
PM	Polarisation Maintaining
PRBS	Pseudo-Random Binary Sequence
PSD	Power Spectral Density
PSK	Phase Shift Keying
QAM	Quadrature Amplitude Modulation
QCSE	Quantum-Confined Stark Effect
QPSK	Quaternary Phase Shift Keying
RAMZI	Ring-Assisted Mach–Zehnder Interferometer
RF	Radio Frequency
RHS	Right Hand Side

RIN	Relative Intensity Noise
RR	Ring Resonator
RRM	Ring Resonator Modulator
SDM	Spatial Division Multiplexing
SE	Spectral Efficiency
SEM	Scanning Electron Microscope
SFDR	Spurious-Free Dynamic Range
SMF	Single Mode Fibre
SNR	Signal to Noise Ratio
SOH	Silicon-Organic Hybrid
SOI	Silicon on Insulator
SPM	Self-Phase Modulation
SSB	Single Sideband
TE	Transverse Electric
TIA	Transimpedance Amplifier
TOX	Top Oxide Layer
TPA	Two Photon Absorption
VOA	Variable Optical Attenuator
WDM	Wavelength Division Multiplexing
XPM	Cross-Phase Modulation

Declaration of Authorship

I, Iosif Demirtzioglou, declare that the thesis entitled *Communication Applications in Silicon Waveguides* and the work presented in the thesis are both my own, and have been generated by me as the result of my own original research. I confirm that:

- this work was done wholly or mainly while in candidature for a research degree at this University;
- where any part of this thesis has previously been submitted for a degree or any other qualification at this University or any other institution, this has been clearly stated;
- where I have consulted the published work of others, this is always clearly attributed;
- where I have quoted from the work of others, the source is always given. With the exception of such quotations, this thesis is entirely my own work;
- I have acknowledged all main sources of help;
- where the thesis is based on work done by myself jointly with others, I have made clear exactly what was done by others and what I have contributed myself;
- parts of this work have been published as listed in the List of Publications and Conference Proceedings at the end of this document;

Iosif Demirtzioglou

Date: 5th September 2019

Acknowledgements

This thesis is the culmination of my four years of work at the ORC and I would like to acknowledge the EPSRC for funding my studies and thank the people who made this possible with their help and support.

First of all, I am grateful to my supervisors, Dr. David Thomson and Prof. Periklis Petropoulos, who have always been there for me throughout my PhD studies. Their guidance was invaluable and I appreciated that their supervision was always based on good communication and aimed to help deepen my understanding of the scientific concepts. I also want to thank them for the friendly atmosphere in all our interactions and meetings, which always encouraged creativity in my research.

During the times of hard work in the laboratory, Dr. Cosimo Lacava has been my mentor in all things concerning lab practice and the scientific approach of problem solving. He has helped me gain experience in working in a research environment and I am grateful for this. I also owe my gratitude to Dr. Mohamed Ettabib who has shown great interest in helping me in my first steps into the research field of silicon photonics. I would also like to thank Dr. Kyle Bottrill for his help in the telecommunications aspects of my research experiments and for our overall discussions on science and technology that really expanded my view of our field. Lastly, I am glad for the opportunities I had to consult and collaborate, to a greater or lesser extent, with researchers at the ORC on various topics that are described in this thesis: Dr. Francesca Parmigiani, Dr. Yongmin Jung and Dr. Yang Hong.

Due to the nature of my PhD project, part of my research relied on the procurement of fabricated devices. I could not have completed a large part of my work without the crucial involvement of Dr. David Thomson and Dr. Abdul Shakoor in the fabrication of the silicon photonic components, as well as without the help of Dr. Li Ke who offered me valuable insight in the field of circuit design. I would also like to thank the Silicon Photonics group that gave me the opportunity to participate in their collaboration with Peking University and carry out part of the experiments in their lab in China. Lastly, I want to thank Angelos Xomalis for our collaboration in the work related to metamaterials that brought me in contact with fields of research different from my own.

I would also like to express my thanks to all my friends in Southampton and in Greece who made everyday life happier for me during these four years through the discussions and quality time we enjoyed together. My special appreciation goes to my dearest friend, Stergios Aidinlis, with whom we shared the experience of studying abroad, each in their own career path. Finally, my deepest gratitude goes to my family, to whom I dedicate this thesis. Without the love and continuous support from my parents and my brother, I would not have completed this journey.

Chapter 1

Introduction

Optical fibre communications are currently the dominant technology driving the exchange of data traffic around the world. The use of the silica glass fibre as a medium for data transport has gone through numerous stages of evolution since its first report by Charles Kao and George Hockham [1], resulting in the current widespread deployment of fibre optic cable bundles for long-distance transmission links. Over the decades, there have been several milestones in this evolution, which include the demonstration of the single-mode optical fibre with a loss approaching the minimum theoretical value in bulk silica ($\sim$0.2 dB/km) [2], the invention of the erbium-doped fibre amplifier (EDFA) in the late 1980s [3, 4], the technique of dispersion management [5] and the introduction of advanced modulation formats [6] to implement coherent modulation and detection in optical systems [7, 8]. Thanks to the aforementioned technological innovations that enabled augmentation of the link capacity, optical networks have always adapted to increasing traffic demands. Maintaining the balance in this supply-and-demand relation is still the target in today's research on optical communications [9], with the challenge of the current era involving the substantial modification of the existing physical network infrastructure, potentially through the introduction of Spatial Division Multiplexing (SDM) [10–12], in order to keep up with the rapidly growing datarate requirements of today's applications.

In addition to the fibre-based systems, the development of photonic components on the Silicon-on-Insulator (SOI) platform has seen a rapid growth in the form of commercial devices for the data centre and High-Performance Computing (HPC) markets. Research in the field of silicon photonics first started in 1985 [13, 14], while commercialisation started shortly after [15, 16], with the main target being sensor applications. Nowadays, the market of silicon photonic devices is predominantly directed by the demand for low-cost short-range optical interconnects in data centres and the computing industry [17]. The popularity of the technology is proven by the amount of transceiver products that have been developed commercially by companies such as Intel [18], Luxtera [19], Acacia [20] and others. A number of key components for telecommunication

applications have successfully been developed in silicon in order to achieve this level of commercialisation [21], however improvements in the cost, power consumption and manufacturing robustness are still being studied. Modulators have been designed either using doped silicon sections in Mach–Zehnder-based configurations or by leveraging electroabsorptive mechanisms (in SiGe or III-V materials), while photodetectors have been most commonly based on the use of germanium. Components with several functionalities that accommodate communication applications (such as multiplexers) have also been designed. Bonding between silicon chips enables packaging photonic and electronic circuits together, while gratings or edge-coupling are used to realise the connection to optical fibres. Lastly, the biggest challenge has been the design of an efficient light emitter in the silicon platform because the indirect bandgap of the material prohibits such an implementation, however on-chip light sources have so far been built using III-V-based lasers that are bonded to the SOI chip.

Although there is a number of alternative materials provided for integration, including Indium Phosphide (InP), Gallium Arsenide (GaAs) and Lithium Niobate ($LiNbO_3$), the choice of silicon is justified by a number of reasons. Firstly, the foundries based on the Complementary Metal-Oxide-Semiconductor (CMOS) technology that already serve the microelectronics industry can be leveraged to offer scalable manufacturing for silicon photonic devices, therefore lowering their cost. Secondly, the structures that are fabricated on the SOI platform exhibit strong light confinement because of the high refractive index contrast between the silicon core and its SiO_2 surroundings, thus enabling the design of devices in the submicrometer scale. Lastly, optical components can be monolithically integrated in silicon along with electronic components and microelectromechanical systems (MEMS) at high density, allowing for convenient copackaging with control circuits.

This PhD project was conducted as part of the Silicon Photonics for Future Systems (SPFS) project (funded by the Engineering and Physical Sciences Research Council (EPSRC) in the UK). The specific objective of SPFS that this project has related to is the development of silicon photonic transceivers for high-capacity applications. The work reported in this thesis studied the development of various components in such a transceiver, spanning from device design and simulation to fabricated component characterisation and data transmission experiments. The work was carried out within the groups of Optical Fibre Communications and Silicon Photonics at the Optoelectronics Research Centre (ORC), while some of the experiments were conducted on the optical communications testbed of the State Key Laboratory of Advanced Optical Communication Systems and Networks of Peking University in China, as part of their collaboration with the Silicon Photonics group in the University of Southampton. The stages in the development procedure of a silicon photonic component consist of the modelling and simulation of the device using software tools, the fabrication processes conducted in appropriate cleanroom facilities, the characterisation of the manufactured device through

laboratory measurements and the evaluation of its performance in an experimental data transmission link, in the case of telecommunications components. The author of this thesis was involved in activities relating to all of the above stages except for the fabrication process, which was conducted by members of the Silicon Photonics group with the appropriate expertise. The work presented in the thesis covers a variety of topics that correspond to different components of a SOI-based telecommunications transceiver: the design and characterisation of grating couplers for mode order conversion, the modelling and experimental generation of a frequency comb using a Ring Resonator Modulator, the characterisation of a Mach–Zehnder Modulator which is used to transmit high-spectral-efficiency data and the design of linear modulator configurations and finally, the implementation of wavelength conversion through the use of a nonlinear waveguide and the design of a fully integrated wavelength converter. A comprehensive description of the thesis structure is provided in the following section.

1.1 Thesis Outline

This thesis is divided into 7 chapters, which first describe all the necessary theoretical elements relating to the technology of silicon photonics and optical communications and then elaborate on the contributions of this project to scientific research. The contents along with the new contributions to the state-of-the-art are outlined in this section.

Chapter 1 provides general context about the field of research that is related to this thesis, while describing the main aspects of the presented work and the topics that it covers.

Chapter 2 presents the basic theoretical concepts behind the research topics investigated in the rest of the thesis. A description of light propagation in silicon waveguides is first presented, with an elaborate analysis of the nonlinear effects present in such structures. Then, the silicon-fibre interface through gratings is described by elaborating on the concept of out-of-plane coupling. The next topic in the chapter concerns electro-optic modulation in silicon and the physical mechanisms that are used to implement it, with a focus on the plasma dispersion effect. Lastly, a description of the most common configurations of silicon modulator devices is presented, namely the Mach–Zehnder Modulator (MZM) and the Ring Resonator Modulator (RRM), while the analytic models for their transfer functions are studied. This section finishes with an outline of the typical performance metrics considered in the design of an electro-optic modulator.

Chapters 3 - 6 describe the design and experimental work conducted by the author under this PhD project and present the results. Chapter 3 reports the simulation-based design of a grating coupler that implements mode order conversion at the chip-fibre interface and presents characterisation results on a fabricated device. The main measured properties that are reported include the power profile at the output of the

grating as well as the efficiency of coupling to a commercial two-mode fibre. The results of this work were presented at the Conference on Lasers and Electro-Optics in 2019 (CLEO 2019) [22] and published in the Photonics Research journal [23].

Chapter 4 investigates the generation of a frequency comb by a Ring Resonator Modulator (RRM) which is driven by sinusoidal electrical signals. An analytic model is provided to study the behaviour of the RRM as a comb generator and a fabricated device is subsequently used to generate a five-line optical frequency comb. The experimental results of this work were published in Optics Express [24].

The topic of Chapter 5 is the use of linear modulators for the transmission of information using advanced modulation formats. A fabricated Mach–Zehnder Modulator (MZM) is characterised in terms of linearity and is then used to transmit data modulated using the Pulse Amplitude Modulation and Discrete MultiTone formats (PAM-4 and DMT respectively) in a medium-reach optical link. The results of this experiment were presented in the European Conference on Optical Communications in 2017 (ECOC 2017) [25] and published in Optics Express [26]. The last section of this chapter investigates the design of a MZM configuration termed Ring-Assisted Mach–Zehnder Interferometer (RAMZI) Modulator which is optimised for linearity, while measurements are reported on a preliminary version of a fabricated device.

Lastly, Chapter 6 describes the characterisation of a fabricated silicon waveguide in terms of its nonlinearity and its use for the Four-Wave-Mixing-based wavelength conversion of data modulated with a 16-Quadrature Amplitude Modulation (16-QAM) format through Bit Error Ratio (BER) measurements. These results were presented at the European Optical Society Biennial Meeting (EOSAM) 2016 [27]. Its last section describes a design for a fully integrated wavelength converter device that includes on-chip pump and signal filtering, with modelling results of different types of ring filters.

Chapter 7 summarises the topics investigated in this thesis, outlines the main results and scientific contributions and discusses the potential future steps in the presented research activities.

Chapter 2

Background

2.1 Silicon Photonic Devices

2.1.1 Propagation in silicon waveguides

A silicon photonic circuit is typically written on a Silicon-on-Insulator (SOI) wafer, which contains the semiconductor material that is the foundation of integrated circuits in the microelectronics industry. The composition of such a wafer is illustrated in Fig. 2.1, where the material layers are presented in a cross-sectional view. At the bottom lies a 725-μm-thick silicon substrate, on which a buried oxide layer (SiO_2 BOX) of a 2-μm thickness forms the base for the silicon layer that hosts the photonic circuit. The crystalline silicon layer (SOI) in which the components are written is usually 220-nm-thick, although different thicknesses are also commercially available. The 220-nm specification is widely used in multi-project wafer (MPW) foundries, while a cladding layer made of SiO_2 is also deposited on top to provide symmetry in the optical surroundings of the circuit, enable the fabrication of metal electrodes above the photonic components, as well as protect them from mechanical damage.

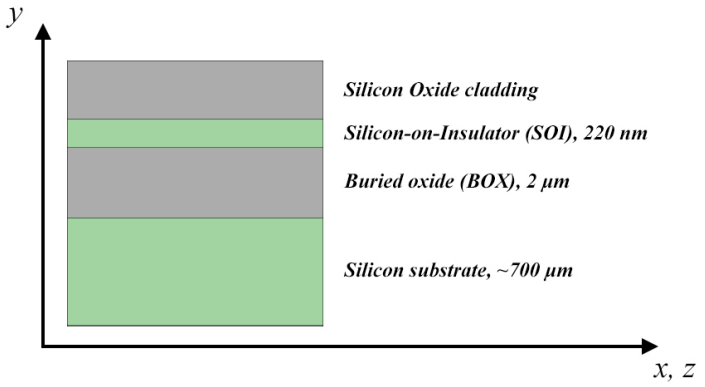

FIGURE 2.1: Composition of a Silicon-on-Insulator (SOI) wafer (not to scale).

The fundamental building block of any silicon photonic component is the waveguide structure. The two types of structures that are typically used to guide light in silicon photonic design are strip and rib waveguides. A strip waveguide is the result of a full etch of the silicon layer (220 nm etching depth), whereas a rib geometry results from a partial etch (e.g. 120 nm etching depth). Scanning Electron Microscope (SEM) pictures of the cross-sections of these waveguide types along with their corresponding simulated mode field profiles are illustrated in Fig. 2.2. The mode confinement is stronger in strip waveguides and this can favour applications that require structures with tight bend radii or make use of nonlinearity, while rib types enable electro-optic functionalities because the geometry allows electrical access to the waveguide from its sides. It is noted that in order for these waveguides to be single-mode in the wavelength range typically used for telecommunications applications (C-band, 1530 - 1565 nm), their width is usually selected to be ∼500 nm.

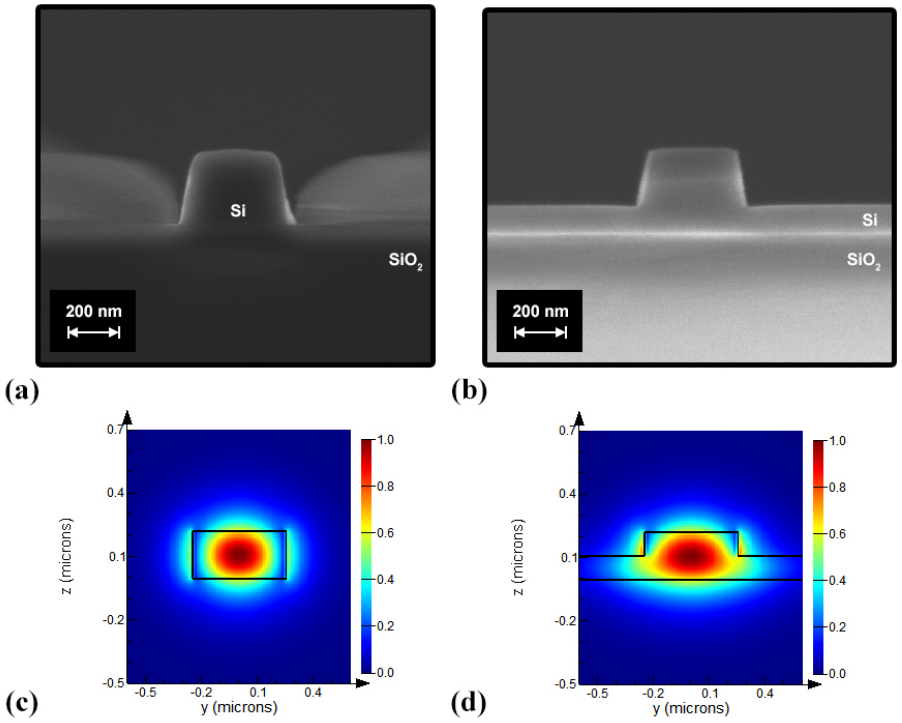

FIGURE 2.2: SEM cross-section images of (a) a strip waveguide and (b) a rib waveguide written on a SOI wafer. (c), (d) Mode profiles (electric field component E_y) for the strip- and rib-type respectively, as simulated in MODE Solutions by Lumerical^{TM}.

The measure of the guiding capability of such silicon waveguides is the propagation loss they exhibit. Like in the case of optical fibres, the optical power attenuation in a silicon waveguide is exponential with propagation length and is expressed by the following equation [28]:

$$P_{out} = P_{in} e^{-\alpha z} \tag{2.1}$$

where α is the attenuation constant, P_{in} is the power launched inside the waveguide and P_{out} is the power at its output, after propagation over a distance z. The attenuation constant is usually expressed in units of dB/cm as per the following relation:

$$\alpha_{dB/cm} = -\frac{10}{L} log(\frac{P_{out}}{P_{in}}) = 4.343\alpha_{cm^{-1}} \tag{2.2}$$

where a reference propagation length L (in cm) was assumed. The attenuation constant comprises the total loss in power experienced by the propagating light. The main sources of optical loss in a silicon waveguide are [29]:

1. Material loss, which is negligible in the case of passive structures at low input optical power levels. However, this factor can contribute greatly to the total loss in the case of active structures, where silicon is doped and free carriers can cause absorption effects, as well as in the case of operation at high optical power levels where the effect of two-photon absorption (TPA) is present.

2. Sidewall scattering loss, which is the main source of optical loss in silicon waveguides. The roughness present on the sidewalls of an etched structure can cause radiation outwards [30], as well as reflections and phase perturbations across its length (Fig. 2.3). Increasing the waveguide width can alleviate the problem, however the potential excitation of undesired higher-order modes has to be taken into account.

3. Metal proximity loss, in the case of devices that contain electrodes to implement some functionality such as heating or biasing a p-n junction and their metallic components contribute to absorption.

From the point of view of optical telecommunication applications, loss is not the only factor that contributes to the deterioration of an optical signal. Dispersion and nonlinearity are significant parameters of a waveguide that can be undesirable or leveraged in order to implement some function, depending on the application.

Regarding dispersion, it has been shown that modifying the transverse dimensions (height, width) as well as the structure type of a waveguide (rib or strip) can affect its Group Velocity Dispersion (GVD) [31, 32]. This is because the total dispersion of the waveguide is dependent on the confinement of the optical mode and it has therefore led to the development of dispersion engineering methods. In particular, it has been shown that strip-type waveguides, where the mode is strongly confined, can exhibit anomalous dispersion in the C-band, whereas their rib-type counterparts generally show smaller amounts of anomalous dispersion or even exhibit normal dispersion in the same band, for common structures of a 300-nm height and a 500-nm width [31].

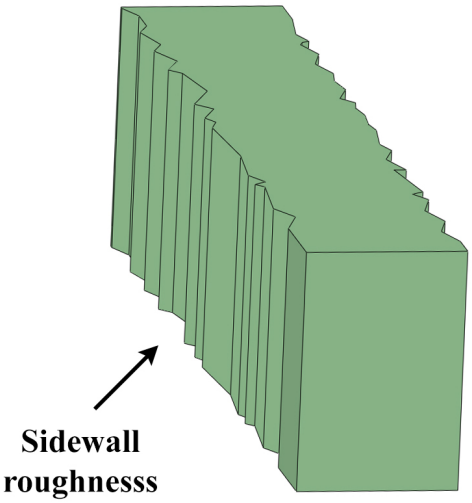

FIGURE 2.3: Schematic of a waveguide at an angled perspective. The roughness of its sidewall is visible (not drawn to scale).

The following section focuses on nonlinearity, as its role in optical signal processing applications is investigated in the experimental part of this thesis (Chapter 6).

2.1.2 Nonlinearity in silicon waveguides

To describe the effects of nonlinearity in silicon waveguides, an analysis of the evolution of the optical field as it propagates inside a nonlinear medium is first provided. Next, the specific effects exhibited in silicon structures are outlined and described. For this purpose, the wave equation is used as the starting point [33]:

$$\nabla^2\mathbf{E} - \frac{1}{c^2}\frac{\partial^2\mathbf{E}}{\partial t^2} = \mu_0\frac{\partial^2\mathbf{P}}{\partial t^2} \tag{2.3}$$

where $\mathbf{E}$ represents the electric field vector, c is the speed of light in vacuum, μ_0 is the vacuum magnetic permeability and $\mathbf{P}$ represents the induced electric polarisation vector. The wave equation is used here to describe the propagation of light in a silicon waveguide. Assuming that the medium is homogeneous, stationary and spatially non-dispersive, the relation between $\mathbf{P}$ and $\mathbf{E}$ can be expressed as:

$$\mathbf{P} = \epsilon_0\Big(\chi^{(1)}\cdot\mathbf{E} + \chi^{(2)}\colon\mathbf{EE} + \chi^{(3)}\vdots\mathbf{EEE} + ...\Big) \tag{2.4}$$

where ϵ_0 represents the vacuum electric permittivity and $\chi^{(n)}$ is the n-th order electric susceptibility which is mathematically represented as a $(n+1)$-rank tensor comprising complex components. The first term on the right-hand side of eq. (2.4), $\chi^{(1)}$, represents

the linear susceptibility of the medium, which relates to its linear response. This term essentially determines the relative permittivity of the medium $\epsilon(\omega)$ through the relation:

$$\epsilon(\omega) = 1 + \tilde{\chi}^{(1)}(\omega) \tag{2.5}$$

In this equation, $\tilde{\chi}^{(1)}(\omega)$ represents the complex susceptibility in the frequency domain and the use of the angular frequency variable ω indicates the frequency dependence of the permittivity $\epsilon(\omega)$. The properties of refractive index $n(\omega)$ and linear absorption coefficient $\alpha(\omega)$ of the medium are related to the permittivity (or dielectric constant) through the expression:

$$\epsilon = (n + i\alpha c/2\omega)^2 \tag{2.6}$$

and by combining eq. (2.5) with eq. (2.6), the following expressions for $n(\omega)$ and $\alpha(\omega)$ are derived:

$$n(\omega) = 1 + \frac{1}{2} Re[\tilde{\chi}^{(1)}(\omega)] \tag{2.7}$$

$$\alpha(\omega) = \frac{\omega}{nc} Im[\tilde{\chi}^{(1)}(\omega)] \tag{2.8}$$

where the mathematical symbols Re and Im represent the real and imaginary parts respectively.

The above analysis treated the medium response which is related to the linear susceptibility term $\chi^{(1)}$. This is sufficient to describe light propagation in silicon in cases where the amplitude of the electric field is relatively small. However, in the cases of large intensity levels of optical excitation in silicon structures, the nonlinear susceptibility terms need to be taken into account to accurately describe light guidance. As silicon is a centro-symmetric material, the second-order susceptibility term is absent, and the effects commonly used in nonlinear applications are related to the third-order term [34].

This section briefly outlines the concepts related to all the non-negligible effects encountered in silicon waveguides in nonlinear applications. The main concepts introduced are the optical Kerr effect, the effect of two-photon absorption (TPA) and the effects of free carrier dispersion (FCD) and free carrier absorption (FCA). Mathematically, these effects correspond to coefficients similar to the linear refractive index and the linear absorption coefficient, however their different roles will be made clear through their inclusion in the nonlinear Schrödinger (NLS) equation which is introduced below.

The phenomena that are present in the propagation of an optical mode inside a silicon waveguide can be described by appropriately modifying the wave equation. By including the induced polarisations associated with the third-order nonlinearity ($\tilde{P}_i^{(3)}(\mathbf{r},\omega)$) and free carriers ($\tilde{P}_i^{f}(\mathbf{r},\omega)$) in the wave equation, it can be written in the frequency domain in the following form [34]:

$$\nabla^2\tilde{E}_i(\mathbf{r},\omega)+\frac{\omega^2}{c^2}n_0^2(\omega)\tilde{E}_i(\mathbf{r},\omega)=-\mu_0\omega^2[\tilde{P}_i^{f}(\mathbf{r},\omega)+\tilde{P}_i^{(3)}(\mathbf{r},\omega)] \tag{2.9}$$

where $\tilde{E}_i(\mathbf{r},\omega)$ represents the Fourier transform of the i-th component of the electric field ($i=1,2,3$ for the x, y, z components respectively) and n_0 is the material refractive index which is generally different for the core and cladding layers of the waveguide.

Because the induced polarisations are considered as small perturbations to the linear wave equation, it can be assumed that the waveguide modes are not affected by them. Therefore, the electric field can be written in the form:

$$\tilde{E}_i(\mathbf{r},\omega)\approx\tilde{F}_i(x,y,\omega)\tilde{A}_i(z,\omega) \tag{2.10}$$

where $\tilde{F}_i(x,y,\omega)$ describes the mode profile in the transverse plane and $\tilde{A}_i(z,\omega)$ describes the mode evolution along the propagation direction z. By substituting eq. (2.10) into eq. (2.9), multiplying by $\tilde{F}_i^*$, integrating over the transverse plane, the following expression is obtained:

$$\frac{\partial^2\tilde{A}_i}{\partial z^2}+\beta_i^2(\omega)\tilde{A}_i=-\mu_0\omega^2\frac{\int\int\tilde{F}_i^*[\tilde{P}_i^{f}+\tilde{P}_i^{(3)}]dxdy}{\int\int|\tilde{F}_i|^2dxdy} \tag{2.11}$$

where $\beta_i(\omega)$ is the propagation constant. Then, by exploiting the Slowly Varying Envelope Approximation, it can be proven that the following expression is derived for the field amplitude [34]:

$$\frac{\partial A}{\partial z}+\underbrace{i\beta_2\frac{\partial^2A}{\partial T^2}}_{Dispersion}=-\underbrace{\frac{1}{2}\alpha_0A}_{Linear\ Loss}-\underbrace{\frac{1}{2}\alpha_fA\frac{n_0}{n}}_{FCA}-\underbrace{i\frac{\omega_0}{c}n_fA\frac{n_0}{n}}_{FCD}+\underbrace{i\gamma_{Re}|A|^2A}_{Optical\ Kerr}-\underbrace{\frac{1}{2}\frac{\beta_{TPA}}{A_{eff}}|A|^2A}_{TPA} \tag{2.12}$$

Eq. (2.12) is referred to as the Nonlinear Schrödinger (NLS) equation and it describes all the effects that occur in a silicon waveguide during the propagation of a monochromatic field at a carrier frequency ω_0. The effects associated with the imaginary terms are responsible for phase changes to the optical mode, while the real terms express amplitude changes and therefore correspond to effects that act as sources of attenuation

(loss). All the variables and parameters present in this equation are defined in the following paragraphs, while the physical effects associated with each term are described accordingly.

Loss

In the above equation, α_0 is the attenuation coefficient of the waveguide that represents the optical loss per unit of propagation length mainly caused by the light scattering on its sidewalls. This type of loss is present in a waveguide structure even at relatively low power levels (where nonlinear effects are negligible) and scales linearly with the propagated distance, as is evident from the term in the differential equation. The parameters n_0 and n represent the material refractive index and the effective refractive index of the waveguide respectively.

Dispersion

Regarding the phase change constant $\beta(\omega)$ in the derivation of the above equation, it was expanded in a Taylor series around ω_0, with β_i representing the expansion coefficients (not to be confused with the indexing convention used in eq. (2.11)). It should be noted that by transferring the wave propagation equation back to the time domain to derive eq. (2.12), a frame of reference moving at the carrier group velocity v_g was also used for the evolution of the optical field, through the transformation $T = t - z/v_g = t - \beta_1 z$. As a result, only the β_2 coefficient is present in the equation, which represents the second-order dispersion in the propagating signal, while β_3 and β_4 were considered to be negligible in this derivation.

In the cases of high level of optical input power to the waveguide, the effects that arise can be divided into two categories: (a) effects related to the Kerr nonlinearity of silicon, which induce changes in the effective refractive index and the attenuation (two-photon absorption) associated with the propagating optical mode, and (b) effects that are related to the free carriers generated by the aforementioned two-photon absorption. These free-carrier effects also cause variations in both the phase (free carrier dispersion) and the intensity (free carrier absorption) of the propagating light. The parameters in eq. (2.12) that are related to the two categories of effects are described below.

Kerr nonlinearity

The $\chi^{(3)}$-related nonlinearity is related to phenomena that are exhibited in silicon when the intensity of the incident light is relatively high and they include two types of effects: the Kerr effect, which induces an intensity-dependent phase change, and the two-photon

absorption (TPA) phenomenon which induces an intensity-dependent loss due to the simultaneous absorption of two photons by the material. The coefficients in the NLS equation that define the strength of these effects form together the complex nonlinear parameter γ [34]:

$$\gamma(\omega) = \gamma_{Re} + i\gamma_{Im} = \frac{\omega n_2}{cA_{eff}} + i\frac{\beta_{TPA}}{2A_{eff}} \tag{2.13}$$

where the Kerr coefficient n_2 is given by the expression [34]:

$$n_2 = \frac{3\chi^{(3)}_{Re}}{4\epsilon_0 c n^2} \tag{2.14}$$

and the TPA coefficient β_{TPA} is given by the expression [34]:

$$\beta_{TPA} = \frac{3\omega\chi^{(3)}_{Im}}{2\epsilon_0 c^2 n^2} \tag{2.15}$$

In both of these equations, n is the effective refractive index of the mode, $\chi^{(3)}_{Re}$ and $\chi^{(3)}_{Im}$ are the real and imaginary parts of the $\chi^{(3)}$ susceptibility, while A_{eff} is a parameter that is related to the field distribution of the mode and expresses the average mode area [34]:

$$A_{eff} = \frac{\left(\int\int |\tilde{F}_i|^2 dxdy\right)^2}{\int\int |\tilde{F}_i|^4 dxdy} \tag{2.16}$$

It is noted that, based on this definition of the complex nonlinear parameter, any free carrier effects are not included in $\gamma(\omega)$; rather, they are treated as separate terms in the NLS equation, as described in the following paragraphs.

Free carrier effects

Given that the TPA process cannot be considered as negligible in silicon waveguides, the effects related to the free carriers TPA produces are also taken into account in the NLS equation. TPA can generate a considerable number of free electrons and holes in the waveguide region, that not only absorb light but also alter the mode propagation by inducing changes to the material refractive index. These two types of effects, Free Carrier Absorption (FCA) and Free Carrier Dispersion (FCD) are expressed in eq. (2.12) through the following two coefficients [34]:

$$n_f(\omega, N_e, N_h) = -\frac{q^2}{2\epsilon_0 n_0 \omega^2}\left(\frac{N_e}{m_e^*} + \frac{N_h}{m_h^*}\right) \tag{2.17}$$

$$\alpha_f(\omega, N_e, N_h) = \frac{q^3}{\epsilon_0 c n_0 \omega^2}\left(\frac{N_e}{\mu_e m_e^{*2}} + \frac{N_h}{\mu_h m_h^{*2}}\right) \tag{2.18}$$

n_f is the refractive index change caused by the presence of free carriers, while α_f is the corresponding absorption coefficient. In eqs. (2.17) and (2.18), q is the electron charge, N_e and N_h are the densities of free electrons and holes respectively, m_e^* and m_h^* are the effective masses of electrons and holes respectively and μ_e and μ_h are the electron and hole mobilities respectively. These expressions are derived through the use of the Drude model which describes well the dynamics of free carriers in the case of silicon waveguides [35]. One useful observation related to the FCA and FCD terms of eq. (2.12) is that the $\frac{n_0}{n}$ coefficient signifies the appearance of stronger free-carrier-related effects in a waveguide structure compared to the case of propagation in a bulk material, because in the former case the effective refractive index n is smaller than the material index n_0 due to mode confinement.

One nonlinear effect that is extensively used for nonlinear applications in Silicon Photonics is Four-Wave Mixing (FWM). As it is the fundamental concept behind applications such as wavelength conversion, which is the topic of Chapter 6 in this thesis, a brief description of the FWM effect is provided in the next section.

2.1.2.1 Four-Wave Mixing in silicon waveguides

Four-Wave Mixing occurs when three different optical waves are launched to a medium exhibiting nonlinearity of the third order and a fourth wave (known as idler) is generated as a result. In practice, FWM can even occur when the input to the nonlinear structure consists of a strong pump wave at a frequency ω_p, along with a weaker signal wave at ω_s, resulting in the generation of an idler wave at ω_i, which constitutes the partially degenerate case of FWM where only three waves are present.

Depending on the application, FWM can either be useful or undesirable. In the case of transmission links that carry wavelength-division-multiplexed (WDM) signals, the frequency generation phenomenon can lead to cross-talk between different channels. On the other hand, the capability of controlling the generation of the idler wave through an optical signal at another wavelength opens the way for the development of all-optical signal processing applications. FWM can also be used as a basis for measurement techniques that evaluate the nonlinearity or the chromatic dispersion of a waveguide [36, 37].

The FWM effect in silicon waveguides can be highly efficient, due to the strong mode confinement. However, since TPA and free-carrier-related effects cannot be neglected at high intensity levels of incident light in these structures, they can be detrimental to the FWM efficiency. Therefore, the following analysis of FWM takes into account all these effects in order to accurately describe how it manifests in silicon photonic devices.

Assuming the presence of three monochromatic waves in a waveguide, their evolution is described by the following three coupled equations [34]:

$$\frac{\partial A_p}{\partial z} = \left[i(\beta_p+\beta_p^f)-\frac{1}{2}\alpha_0\right]A_p+i\gamma\left(|A_p|^2+2|A_s|^2+2|A_i|^2\right)A_p+2i\gamma A_s A_i A_p^* e^{i\kappa z} \quad (2.19)$$

$$\frac{\partial A_s}{\partial z} = \left[i(\beta_s+\beta_s^f)-\frac{1}{2}\alpha_0\right]A_s+i\gamma\left(|A_s|^2+2|A_p|^2+2|A_i|^2\right)A_s+i\gamma A_p^2 A_i^* e^{-i\kappa z} \quad (2.20)$$

$$\frac{\partial A_i}{\partial z} = \left[i(\beta_i+\beta_i^f)-\frac{1}{2}\alpha_0\right]A_i+i\gamma\left(|A_i|^2+2|A_p|^2+2|A_s|^2\right)A_i+i\gamma A_p^2 A_s^* e^{-i\kappa z} \quad (2.21)$$

where the subscripts p, s, i refer to the pump, signal and idler waves respectively. β_u and β_u^f represent the linear propagation constant and the free-carrier-related complex propagation constant for each of the waves respectively, with the subscript u indicating the wave to which they correspond. The equation for the idler wave describes the new frequency generated by the FWM process. The last four terms on the right hand side of equations (2.19) - (2.21) represent the nonlinear effects of Self-Phase Modulation (SPM), Cross-Phase Modulation (XPM) and Four-Wave Mixing (FWM), where the latter is expressed by the last term. In practice the pump wave is much more intense than the signal and idler waves, therefore pump depletion as well as SPM and XPM effects produced by the signal and idler can be ignored. As a result, eqs. (2.19) - (2.21) take the following form [34]:

$$\frac{\partial A_p}{\partial z} = \left[i(\beta_p+\beta_p^f)-\frac{1}{2}\alpha_0\right]A_p+i\gamma|A_p|^2A_p \quad (2.22)$$

$$\frac{\partial A_s}{\partial z} = \left[i(\beta_s+\beta_s^f)-\frac{1}{2}\alpha_0\right]A_s+i2\gamma|A_p|^2A_s+i\gamma A_p^2 A_i^* e^{-i\kappa z} \quad (2.23)$$

$$\frac{\partial A_i}{\partial z} = \left[i(\beta_i+\beta_i^f)-\frac{1}{2}\alpha_0\right]A_i+i2\gamma|A_p|^2A_i+i\gamma A_p^2 A_s^* e^{-i\kappa z} \quad (2.24)$$

It can be seen that the FWM terms are accompanied by a coefficient that includes the parameter of phase mismatch κ. In order for the FWM process to be efficient, phase matching among the interactive waves is required. This concept is related to the momentum conservation among the four photons involved in the FWM process. It can be proven from the derivation of eqs. (2.22) - (2.24) that the total phase mismatch is [34]:

$$\kappa = \Delta\beta + \Delta\beta_f + 2P_p Re(\gamma) \tag{2.25}$$

where the first term represents the linear phase mismatch $\Delta\beta = \beta_s + \beta_i - 2\beta_p$, the last term is the nonlinear phase mismatch related to the Kerr nonlinearity, while the second term represents the phase mismatch induced by free carriers and is equal to [34]:

$$\Delta\beta_f = Re(\beta_s^f + \beta_i^f - 2\beta_p^f) = \frac{N_{avg}\sigma_{np}\omega_p^2}{c^2}\left(\frac{n_{0s}}{\beta_s} + \frac{n_{0i}}{\beta_i} - 2\frac{n_{0p}}{\beta_p}\right) \tag{2.26}$$

given that the free-carrier-related complex propagation constant β_u^f is given by [34]:

$$\beta_u^f = \frac{n_0(\omega)}{n(\omega)}\left[\frac{\omega}{c}n_f(\omega) + i/2a_f(\omega)\right] \tag{2.27}$$

In eq. (2.26), σ_{np} is the coefficient linking the refractive index change n_f to the average density of free carriers N_{avg} according to the formula $n_f = \sigma_{np}N_{avg}$.

The free-carrier-induced phase mismatch $\Delta\beta_f$ acts as an added second- and higher-order dispersion and it can be verified [34] that its quantities in the telecom band are relatively small, therefore the total phase mismatch in a silicon waveguide is dominated by the terms related to the linear mismatch and the Kerr nonlinearity contribution. Regarding the linear phase mismatch, it can be observed that it can be minimised by either reducing the wavelength difference between the pump and the signal or by setting the pump wavelength close to the zero-dispersion point. This last method is clear when $\Delta\beta$ is expressed as [33]:

$$\Delta\beta = -\frac{8\pi f_p^2}{c}D(f_p)(f_s - f_p) \tag{2.28}$$

where $D(f_p)$ represents the dispersion parameter at the pump wavelength.

2.1.3 Interface with fibre systems – Grating Couplers

The waveguides that comprise a silicon photonic circuit are much smaller than an optical fibre, owing to the strong mode confinement that is facilitated by the high refractive index difference between its core and cladding ($n_{Si} = 3.47$ and $n_{SiO_2} = 1.44$ at a wavelength of 1550 nm for a silicon waveguide in silica surroundings). Therefore, the coupling of an integrated circuit to a fibre system requires the implementation of a technique designed to match the mode sizes of the two media.

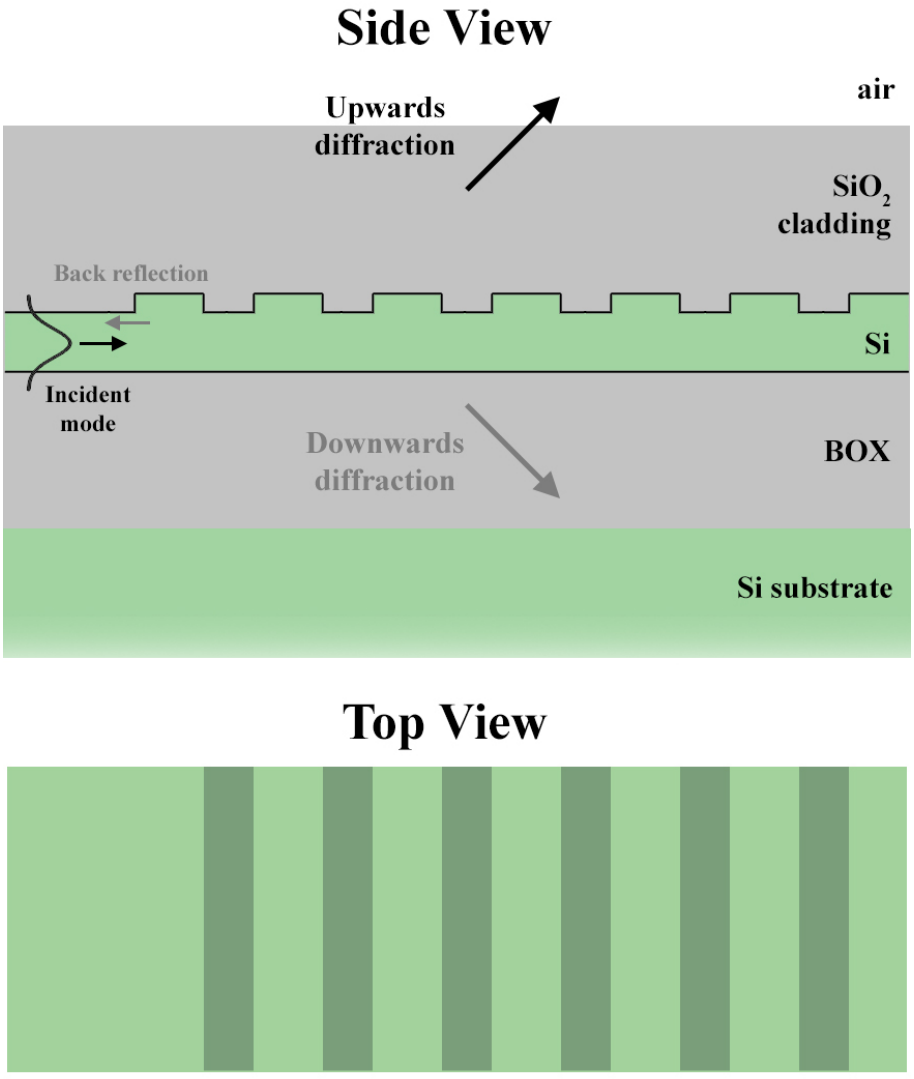

FIGURE 2.4: Schematic representation of a SOI grating coupler. Top: Side view and layer configuration, Bottom: Top view.

The solutions that are widely used in fabrication facilities and multi-project-wafer (MPW) foundries consist of two proposed techniques: the edge-coupling and the out-of-plane-coupling configurations. Edge-coupling involves aligning the optical axes of a fibre and a waveguide so that they lie on the same plane and bringing the fibre facet in close proximity to the side of the chip that contains the end point of the waveguide. By

means of an integrated spot size converter that is drawn at the edge of the waveguide, coupling can be achieved with an insertion loss of less than 0.5 dB [38, 39]. The second technique involves the design of a grating structure in the same layout as the rest of the circuit. The grating is written on the silicon layer of the wafer by selectively etching the waveguide to create a periodic pattern of trenches. The top and side views of a grating coupler are illustrated in Fig. 2.4. An optical mode propagating in-plane along the waveguide changes direction when it interacts with the pattern and can radiate upwards through the silica cladding and the air to couple to a fibre through its facet.

The edge-coupling solutions generally exhibit larger values of coupling efficiency to fibres, larger bandwidths of operation and no polarisation dependent loss, while recent research in the field has moved towards interface with common single-mode fibres (SMFs) with 10-μm mode-field diameters (MFDs), thus expanding the initial studies which involved only lensed fibres [40]. However, their requirements for high-quality facet polishing and high-resolution optical alignment have led the research community to also acknowledge the importance of the alternative grating coupler solutions. Gratings can be positioned anywhere in the photonic circuit and coupling through this technique exhibits lower sensitivity to the fibre alignment, compared to the edge-coupling method. As a result, in cases of fabrication foundries which target mass production of components and wafer-scale testing is important, this implementation of fibre-to-waveguide coupling is sometimes preferred. The principle of operation and design considerations of grating couplers is described in further detail in this section.

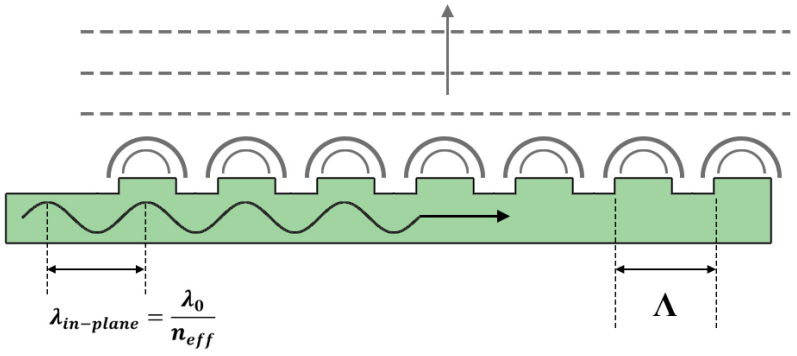

FIGURE 2.5: Vertical coupling concept illustration based on the Huygens-Fresnel principle.

The operation of a vertical coupler based on an etched grating pattern can be understood through the Huygens–Fresnel principle. An in-plane optical mode incident on the grating pattern experiences diffraction by each trench, which can be considered as a point scatterer and therefore a source of a new spherical wavelet. This is illustrated in Fig. 2.5 where a number of individual spherical waves are generated by the grooves of the grating. The interference of these wavelets forms an upwards-radiating wavefront, whose propagation angle is determined by the type of interference. In the case where the

in-plane mode encounters each trench after a phase delay of 2π, the output wavefront propagates perpendicularly to the chip plane. This is equivalent to the groove periodicity Λ being equal to the mode wavelength $\lambda_{in-plane} = \frac{\lambda_0}{n_{eff}}$, where λ_0 is the free-space wavelength and n_{eff} is the effective refractive index of the in-plane mode.

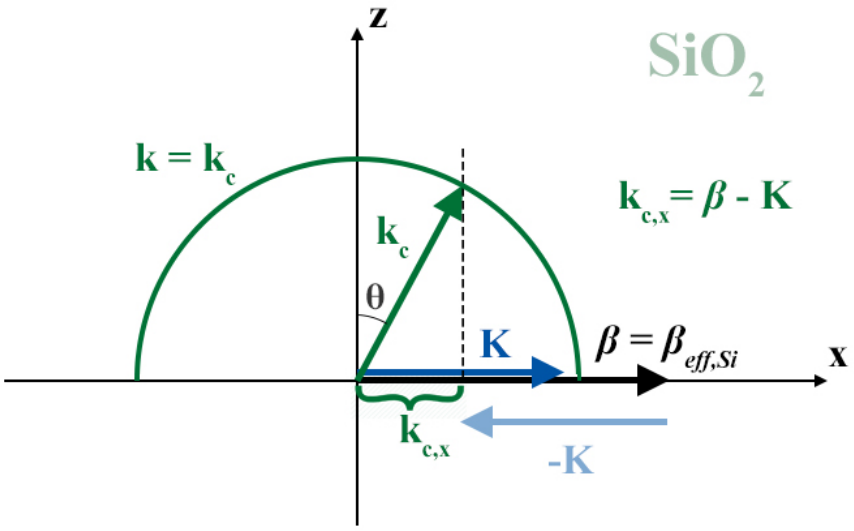

FIGURE 2.6: Graphical representation of the Bragg condition through the Ewald circle corresponding to a grating coupler.

Another approach to the diffraction phenomenon which can offer more insight into the operation of out-of-plane couplers that cause radiation at an angle is the consideration of the corresponding Ewald sphere [41]. Given that the pattern exhibits periodicity in only one direction, the grating is one-dimensional and therefore the Ewald sphere degenerates into a circle, as shown in Fig. 2.6. The x-z plane represents the spatial frequency domain, or k-space, of the system, and the k-vectors drawn on it correspond to spatial frequency components along the in-plane direction of propagation (x-axis) and the direction that is perpendicular to the chip (z-axis). The in-plane wave that travels along the grating section of the waveguide is represented by the vector in black which has a magnitude of $\beta = n_{eff}k_0$, while the periodicity of the grating is represented by the vector in blue which has a magnitude of $K = \frac{2\pi}{\Lambda}$. β and K therefore express the spatial frequencies of the wave and the etched pattern respectively. According to the theory of Fourier optics, the wave resulting from the first-order diffraction of the propagating wave by the grating pattern is the one represented by the green k-vector in Fig. 2.6. For a silica-cladded grating, the magnitude of this vector is equal to $k_c = n_c k_0$, where $n_c = n_{SiO_2}$, and its x-component is given by $k_{c,x} = \beta - K$. This determines the angle of radiation $\theta = sin^{-1}\frac{k_{c,x}}{k_c}$. It is noted that because light propagation in the x-axis occurs in a different material and structure (Si waveguide) than in the x-z upper half-plane (SiO_2), the radius of the Ewald circle $n_c k_0$ is different from the magnitude of the in-plane wave vector $n_{eff}k_0$. The above relations are summed up in the equation that expresses Bragg's law:

$$n_{eff} - n_c sin\theta = \frac{\lambda_0}{\Lambda} \tag{2.29}$$

Eq. 2.29 relates the pattern periodicity of a grating coupler to its angle of radiation, given the material and operating wavelength of the system. Therefore, it is the fundamental tool in the design of silicon photonic gratings.

The most important parameter in grating coupler design is the coupling efficiency between the waveguide and the optical fibre. As this can be directly related to the insertion loss of the grating coupler device, it is important to identify the sources of optical loss related to such a component. The types of loss are outlined below:

1. Loss due to back reflection: When the optical mode propagating in the waveguide encounters the etched trenches, part of the light is reflected due to the high refractive index difference and counter-propagates inside the waveguide. When this effect is present in both input and output gratings, part of the light can be trapped inside the waveguide due to successive reflections at both ends. Thus, a Fabry-Pérot-type cavity is formed, which results in the transmitted power showing a sinusoidal relation to optical wavelength at the output of the silicon photonic device [42, 43]. The effect of back reflection can also appear when light launched from a fibre is incident on the grating, leading to optical power being sent back to the input fibre. Shallow etching of the trenches can mitigate the effect of back reflection. Additionally, light can experience higher orders of diffraction (up to the second order in commonly used designs) that can contribute to a loss of optical power. In particular, in the case of perfectly vertical coupler designs, the second-order Bragg diffraction component essentially contributes to back reflection, therefore it is often preferable in practice to design gratings that operate at an angle [29].

2. Penetration loss: As light encounters the grating pattern, part of it can be scattered downwards to the SiO_2 substrate. This can be alleviated by the use of shallow-etched trenches as mentioned above and by introducing reflectors under the grating devices [44–48].

3. Mismatch between radiated profile and fibre mode: The part of the light that is radiated upwards towards the fibre exhibits a power profile determined by the strength of the scattering effect caused by the grating grooves. In a uniform pattern where the periodicity and trench width are constant across the length of the grating, most of the optical power is scattered by the first teeth with which the mode interacts. Therefore, the radiated power shows an exponential-decay profile, which has a low overlap with the Gaussian shape of an optical fibre mode. As a result, only part of the upwards-propagating light couples into the fibre and this mismatch can effectively be considered as a source of loss. The coupling

efficiency can be increased by adopting an apodised grating design, where the trench width (and even the periodicity) is varied across the device length, resulting in a Gaussian-shaped radiated profile [44, 47–50]. A uniform and an apodised grating along with their respective radiated power profiles are illustrated in Fig. 2.7.

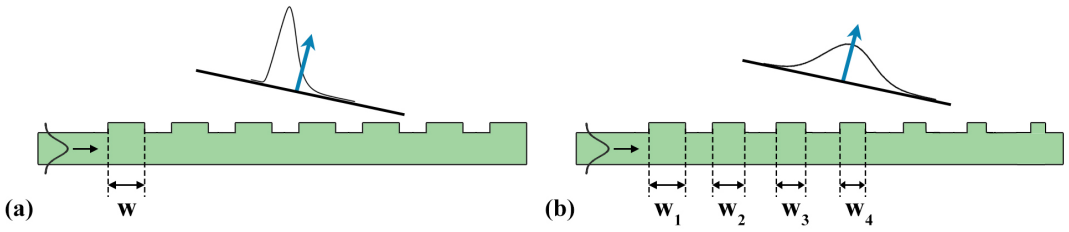

FIGURE 2.7: Side view of (a) a uniformly etched grating coupler and (b) a grating with an apodised etching pattern, along with the respective radiated power profiles.

2.1.4 Electro-optic components

The application of silicon photonics in telecommunication environments is directly related to the development of the fundamental optical transmitter and receiver units. The design of a silicon photonic transceiver system involves the development of a variety of components that provide all the required functionalities. The most important role in this set of devices is occupied by the electro-optic modulator.

Electro-optic modulation involves a change caused to the optical mode by an applied electric field [51]. The effect on the mode is expressed mathematically by a change to the complex effective refractive index $\tilde{n}_{eff} = n_{eff} + i\alpha$, which contains information about the phase velocity in the waveguide (real part, n_{eff}) and the propagation loss (imaginary part, α). Based on the property that the electric field modifies, the electro-optic effects can be categorised in electro-refractive (when the change relates to the real part of $\tilde{n}_{eff}$) and electro-absorptive (when the change relates to the imaginary part of $\tilde{n}_{eff}$).

The electro-optic effects that are commonly used in the design of silicon modulators are summarised here, with an emphasis on the plasma dispersion effect, which is the mechanism employed for modulation in all the fabricated devices reported in this thesis.

2.1.4.1 Thermo-optic effect & Plasma dispersion effect

The most efficient mechanisms enabling electro-optic modulation in silicon at the telecommunications wavelengths of 1550 nm and 1310 nm involve either the thermo-optic coefficient of the material or the plasma dispersion effect. Although the former can exhibit sufficient values of modulation depth, the speed of the thermo-optic effect does not

support the high datarates required in telecommunications systems [52]. For this reason, it finds applications in switching configurations that do not require operation at high speed. Modulation targeting the conversion of fast electrical signals to the optical domain is mainly served by plasma-dispersion-based components.

The plasma dispersion effect describes the change in the complex refractive index of silicon $\Delta\tilde{n}$ caused by a change in the concentration of free carriers in the material. The relation between these properties was studied and quantified by Soref and Bennett in 1987 [35]. Since free carriers in silicon can consist of both electrons and holes, the expressions relating the change in refractive index and absorption due to changes in the concentration of both types of carriers when the operating wavelength is 1550 nm are the following [35]:

$$\Delta n = \Delta n_e + \Delta n_h = -[8.8 \cdot 10^{-22} \cdot \Delta N_e + 8.5 \cdot 10^{-18} \cdot (\Delta N_h)^{0.8}] \tag{2.30}$$

$$\Delta \alpha = \Delta \alpha_e + \Delta \alpha_h = 8.5 \cdot 10^{-18} \cdot \Delta N_e + 6.0 \cdot 10^{-18} \cdot \Delta N_h \tag{2.31}$$

where Δn_e and Δn_h represent the changes in the refractive index due to the concentration change relating to electrons and holes respectively, while $\Delta \alpha_e$ and $\Delta \alpha_h$ are the variables corresponding to absorption change, where the subscripts again represent the source of the effect. ΔN_e and ΔN_h describe the changes in the concentration of free electrons and free holes respectively in silicon. The expressions corresponding to a wavelength of 1300 nm are given below [35]:

$$\Delta n = \Delta n_e + \Delta n_h = -[6.2 \cdot 10^{-22} \cdot \Delta N_e + 6.0 \cdot 10^{-18} \cdot (\Delta N_h)^{0.8}] \tag{2.32}$$

$$\Delta \alpha = \Delta \alpha_e + \Delta \alpha_h = 6.0 \cdot 10^{-18} \cdot \Delta N_e + 4.0 \cdot 10^{-18} \cdot \Delta N_h \tag{2.33}$$

Equations (2.30) - (2.33) show that for carrier density changes of the order of $5 \cdot 10^{17}$ cm^{-3}, the refractive index change Δn can reach values of $-1.66 \cdot 10^{-3}$ and $-1.18 \cdot 10^{-3}$ for wavelengths of 1550 nm and 1300 nm respectively.

Building a silicon modulator based on the plasma dispersion effect involves designing components that can manipulate free carriers in silicon. Doped silicon waveguides are used for this purpose and the three main structures that are used to form modulators are presented in Fig. 2.8. All three types consist of rib waveguides with highly doped regions of silicon on both sides, on which the electrical signal is applied through metallic vias. The behaviour of these structures when voltage is applied to the p+ and n+ sections can affect the concentration of free carriers in the part of the waveguide that overlaps

with the propagation mode. Fig. 2.8 (a) shows a carrier-accumulation device, where a thin layer of SiO_2 lies in the middle of the silicon waveguide to provide insulation and therefore act as a capacitor. Fig. 2.8 (b) depicts a structure based on carrier injection, where a forward bias causes free electrons and holes to enter the 'intrinsic' region in the middle of the waveguide, which consists of undoped silicon. Finally, Fig. 2.8 (c) shows a carrier-depletion device, which operates in reverse bias. In this case, p- and n-doped regions cover the entirety of the waveguide, forming a p-n junction that naturally contains a depletion area. The width of this depletion area can change based on the applied reverse bias voltage and its overlap with the optical mode determines the strength of the modulation effect.

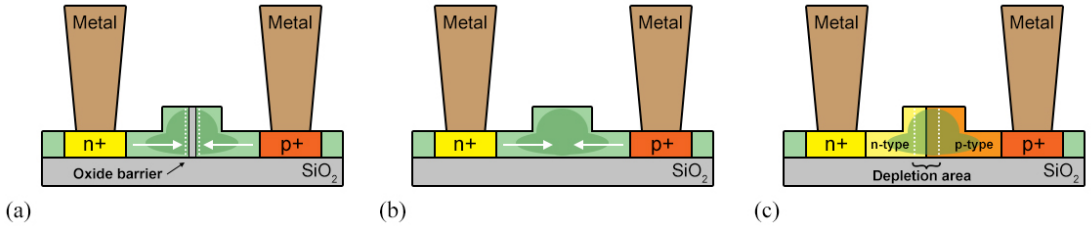

FIGURE 2.8: Cross-sections of typical modulator structures based on the plasma dispersion effect: (a) carrier accumulation, (b) carrier injection and (c) carrier depletion types.

2.1.4.2 Other effects

It should be noted that the effects that are primarily considered for electro-refraction and electro-absorption in semiconductors are the Pockels effect and the Franz-Keldysh effect. The reason that the plasma dispersion effect is usually preferred in silicon photonics is that the aforementioned mechanisms are weak in crystalline silicon at the wavelengths of interest. However, alterations in the structure and fabrication technique of the waveguides have indeed been considered to leverage some of these effects and achieve efficient electro-optic conversion. These effects require the combination of silicon with other materials in the same structure which raises the complexity of the design process and fabrication.

In particular, the Quantum-Confined Stark Effect (QCSE) enables the design of electro-absorption modulators in germanium quantum well structures [53, 54], while in bulk SiGe structures this is enabled by the Franz-Keldysh effect [55]. The inclusion of germanium, another CMOS-compatible Group IV material, has seen significant progress since the demonstration of the first modulator designs [56, 57]. Lastly, Pockels modulators have also been reported as this effect can appear through the application of mechanical strain on silicon [58] or silicon nitride [59].

2.1.5 Modulator devices

Since the electro-optic components that are most commonly used are based on the plasma dispersion effect, the fundamental devices composed of p- and n-doped silicon waveguides function as phase modulators, due to the electro-refractive nature of this mechanism. However, in a transmitter unit, the fundamental electro-optic device is usually an intensity modulator, therefore specific photonic circuits must be constructed around the aforementioned electro-refractive components to form devices that manipulate the output optical intensity. The most common of these configurations are the Mach–Zehnder Interferometer and the Ring Resonator. Intensity modulation is achieved by modifying the refractive index in certain waveguide sections of these topologies. This section describes their analytic transfer functions, while discussion and comparisons are provided regarding their modulation properties, such as the modulation depth and bandwidth.

2.1.5.1 Mach–Zehnder Modulators

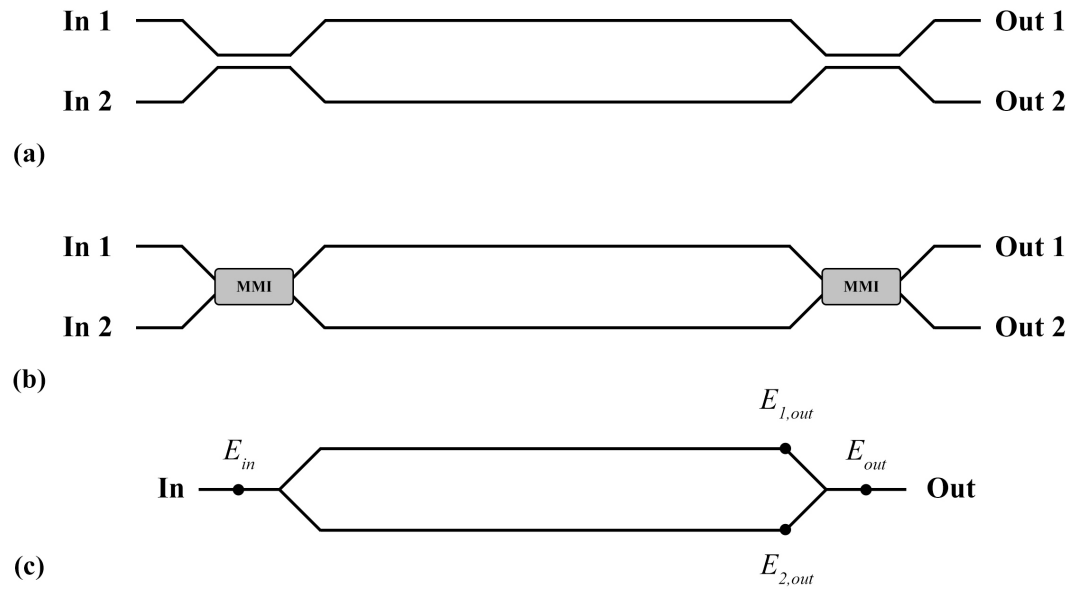

FIGURE 2.9: Schematic representation of the Mach–Zehnder Inteferometer topology implemented with (a) evanescent-wave couplers, (b) multi-mode interference (MMI) couplers, (c) Y-junctions.

One common waveguide topology that relates optical phase variations to intensity changes is the Mach–Zehnder Interferometer (MZI). As the name suggests, it is based on the concept of interference between two input waves and a schematic of such a device is illustrated in Fig. 2.9 (a). It consists of two optical coupler components that perform inverse operations: the first one splits the input beam to send its components into two different waveguides, whereas the second one combines the beams and produces two different results that can be collected from the end waveguides. Even though this is

a 2 × 2 structure, it is commmon to use a single output port for a given input and as a result, other implementations of the MZI include multi-mode interference (MMI) couplers (Fig. 2.9 (b)) or Y-junctions (Fig. 2.9 (c)) to realise the splitting and joining functions. For the purpose of presenting the operating principles behind the fabricated modulators described in the experimental section, the following analysis only treats the single-input single-output configuration.

In order to analyse the Mach–Zehnder modulator, the transfer function of the optical interferometer without any electro-optic functionality is first extracted. Based on Fig. 2.9 (c), the expressions for the electric field in the two MZI arms $E_{1,out}$ and $E_{2,out}$ after the splitter component and after propagation over the full MZI arm length are given by [29]:

$$E_{1,out} = \frac{E_{in}}{\sqrt{2}}\alpha_1 e^{-j\beta_1 L_1} = \frac{E_{in}}{\sqrt{2}}\alpha_1 e^{-jk_0 n_{eff,1} L_1} \tag{2.34}$$

$$E_{2,out} = \frac{E_{in}}{\sqrt{2}}\alpha_2 e^{-j\beta_2 L_2} = \frac{E_{in}}{\sqrt{2}}\alpha_2 e^{-jk_0 n_{eff,2} L_2} \tag{2.35}$$

where L_1 and L_2 are the lengths of the MZI arms, k_0 is the free-space wavenumber, $n_{eff,1}$ and $n_{eff,2}$ are the effective refractive indices in each of the arms and α_1 and α_2 represent the optical loss accumulated after propagation over the full length of the MZI arms. It is noted that the parameters α_1 and α_2 here do not represent the attenuation constant as it was defined in eq. (2.1). Their relation to the attenuation constants of the MZI arms which are represented here by a_1 and a_2 is given by the equation $\alpha_i = e^{-a_i L_i}, i = 1, 2$, therefore they take values between 0 and 1 (with 0 corresponding to the full attenuation of the electric field after propagation in the MZI arm and 1 corresponding to no attenuation). The division of the electric field by $\sqrt{2}$ in eqs. (2.34) - (2.35) results from the assumption that a 50:50 power splitter is used. The electric field at the output of the full device is then calculated to be:

$$E_{out} = \frac{E_{1,out}}{\sqrt{2}} + \frac{E_{2,out}}{\sqrt{2}} = \frac{E_{in}}{2}(\alpha_1 e^{-jk_0 n_{eff,1} L_1} + \alpha_2 e^{-jk_0 n_{eff,2} L_2}) \tag{2.36}$$

based again on the assumption of a 50:50 power coupler. Since the property of interest when calculating the device transmission is optical power rather than electric field, the following expression for the output intensity is more useful for the purposes of this analysis:

$$I_{out} = |E_{out}|^2 = \frac{I_{in}}{4}\left[\alpha_1^2 + \alpha_2^2 + 2\alpha_1\alpha_2 cos(k_0\big(n_{eff,1}L_1 - n_{eff,2}L_2\big))\right] \tag{2.37}$$

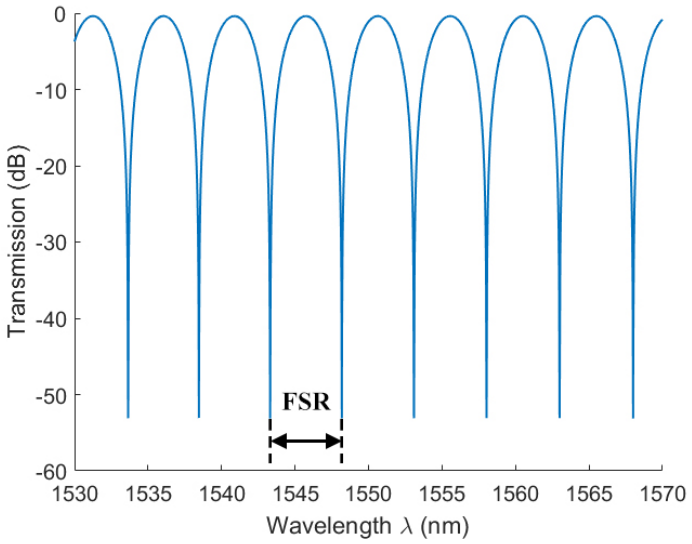

FIGURE 2.10: Transmission of a Mach–Zehnder interferometer with arm lengths $\{L_1, L_2\} = \{1.8 \text{ mm}, 2 \text{ mm}\}$ (calculated in MATLAB from eq. (2.37)).

Then, the transmission (or equivalently the intensity transfer function) is given by the ratio $\frac{I_{out}}{I_{in}}$. This transfer function is plotted with respect to wavelength in dB scale in Fig. 2.10 for an unbalanced MZI, which is the configuration that comprises arms of different lengths. It is clear that there is a sinusoidal relation to the operating wavelength. This arises from eq. (2.37), where the variable λ that signifies the wavelength is present through its relation to the wavenumber, $k_0 = \frac{2\pi}{\lambda}$. The period of this function, termed its Free Spectral Range (FSR), is given by the following expression:

$$FSR = \frac{\lambda^2}{n_g|L_1 - L_2|} \tag{2.38}$$

where n_g represents the group refractive index of the waveguide, defined as $n_g = n_{eff} - \lambda\frac{\partial n_{eff}}{\partial \lambda}$.

It is clear from eq. (2.37) that a change in the effective refractive index of one of the arms can alter the transmission function. In particular, Fig. 2.11 depicts the change of the transfer function when the n_{eff} of one of the arms is varied. The effect is a shift in the wavelength axis which causes the optical output at a specific wavelength to traverse through the peak and trough values of the sinusoidal transfer function. If peaks and troughs correspond to ON and OFF states respectively, it is clear how an electro-optic component (e.g. a doped waveguide) incorporated into one of the MZI arms can turn the MZI circuit into an intensity modulator.

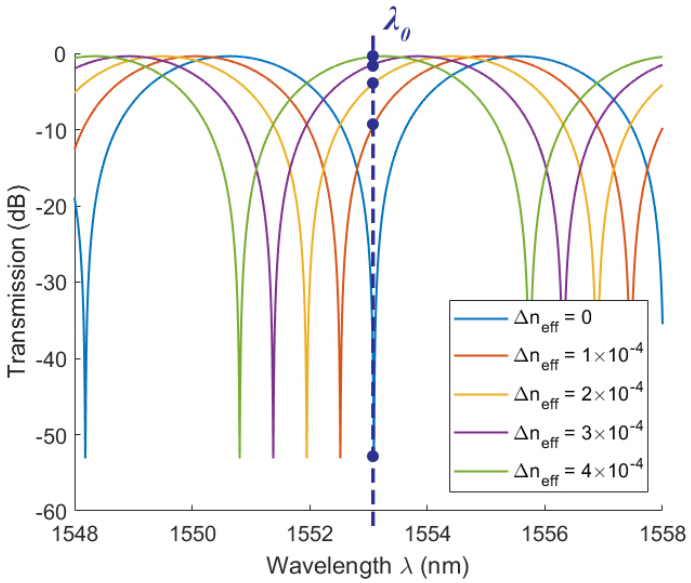

FIGURE 2.11: Transmission of a Mach–Zehnder interferometer for different effective refractive index changes applied to one arm $\left(\{L_1, L_2\} = \{1.8 \text{ mm}, 2 \text{ mm}\}\right)$ (calculated in MATLAB from eq. (2.37)).

2.1.5.2 Ring Resonator Modulators

The Ring Resonator (RR) is another configuration that can act as an intensity modulator when an electrorefractive component is incorporated into it. A schematic of a ring structure coupled to a bus waveguide is shown in Fig. 2.12, where the arrows represent the propagation direction of light. The electric fields at different points of the structure are also marked and help to analyse it and extract its transfer function.

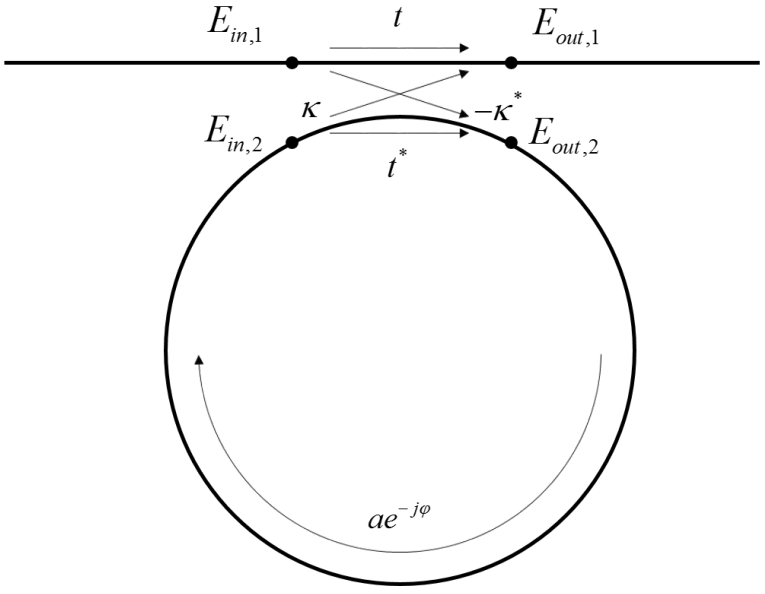

FIGURE 2.12: Schematic representation of a ring resonator structure.

The first component that is important in this analysis is the optical coupler that connects the bus waveguide to the ring structure and essentially provides the excitation to the ring. Such a coupler is realised by two waveguide structures that are in close proximity with each other and utilise the concept of evanescent-wave coupling. As a 2×2 component, it is mathematically expressed by [60]:

$$\begin{bmatrix} E_{out,1} \\ E_{out,2} \end{bmatrix} = \begin{bmatrix} t & \kappa \\ -\kappa^* & t^* \end{bmatrix} \begin{bmatrix} E_{in,1} \\ E_{in,2} \end{bmatrix} \tag{2.39}$$

where t is the through coupling coefficient, representing the ratio between $E_{out,1}$ and $E_{in,1}$ in the presence of evanescent-wave coupling when there is no input $E_{in,2}$, while κ is the cross-coupling coefficient that relates $E_{out,2}$ to $E_{in,1}$ under the same conditions. The two coefficients are related to each other through the expression $|\kappa|^2 + |t|^2 = 1$.

Next, the round-trip propagation inside the ring can be described by the equation:

$$E_{in,2} = \alpha e^{-j\phi} E_{out,2} \tag{2.40}$$

where α is the total attenuation the electric field experiences during a round-trip and ϕ represents the accumulated phase over the same propagation length. This phase is equal to $\phi = \frac{2\pi}{\lambda} n_{eff} L$, where λ is the free-space wavelength of the light, n_{eff} is the effective refractive index of the propagation mode, while L represents the circumference of the ring. From eq. (2.39) and eq. (2.40), we derive the expression:

$$E_{out,1} = \frac{t - \alpha e^{-j\phi}}{1 - \alpha t e^{-j\phi}} E_{in,1} \tag{2.41}$$

for the output electric field at the through port of the structure. The ratio $\frac{E_{out,1}}{E_{in,1}}$ represents the transfer function of the device relating to the electric field, therefore it contains information about the ring resonator system both in relation to optical intensity and to phase. In particular, the expression for the output optical intensity is the following [60]:

$$I_{out} = \frac{|t|^2 + \alpha^2 - 2\alpha|t|cos(\phi + \theta)}{1 + \alpha^2|t|^2 - 2\alpha|t|cos(\phi + \theta)} I_{in} \tag{2.42}$$

where θ is the phase of the complex transmission coefficient t.

The intensity transfer function with respect to wavelength is plotted in Fig. 2.13. Similarly to the MZI case, the function shows periodicity and troughs are observed at the resonance wavelengths, for which light completes the largest number of round-trips inside the ring and consequently the optical intensity inside the resonator structure takes its maximum value. The resonance wavelengths λ_{res} are the ones that satisfy the condition

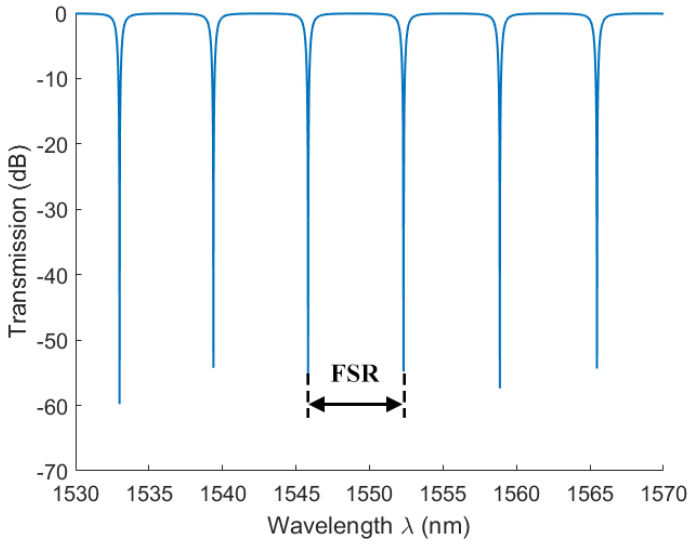

FIGURE 2.13: Transmission of a 24-μm-diameter ring resonator with parameters $\{\alpha, t\} = \{0.8897, 0.8895\}$ (calculated in MATLAB from eq. (2.42)).

$\frac{\lambda_{res}}{n_{eff}} = \lambda_{prop} = m \cdot L$, $m = 1, ...,$ where λ_{prop} represents the wavelength of the propagation mode. This condition describes a case where an integer number of propagation wavelengths can 'fit' inside the ring circumference, corresponding to the constructive interference of $E_{in,1}$ and $E_{in,2}$ at the input point of the ring structure. This leads to the coupler consecutively routing all the optical power to the resonator, which eventually accumulates inside the ring. The spacing between two such resonance wavelengths (again termed Free Spectral Range, FSR) is given by:

$$FSR = \frac{\lambda^2}{n_g L} \tag{2.43}$$

where n_g represents the group refractive index of the waveguides comprising the ring structure.

As indicated by eq. (2.42), the ring resonator transmission is dependent on the refractive index and waveguide length parameters, like the Mach–Zehnder Interferometer configuration. However, it involves two additional design parameters, namely the α and t variables, which essentially determine the coupling condition of the ring. This provides additional degrees of freedom in the design of a ring resonator and it is useful to analyse the effect of different $\{\alpha, t\}$ combinations on the shape of the RR transfer function.

The α and t parameters are directly related to the total loss light experiences in a round-trip and the coupling strength between the bus waveguide and the ring structure respectively. Based on the relation between α and t, three coupling regimes can be identified [61], which are illustrated in Fig. 2.14 through geometry layouts and the phase and intensity transfer functions to which they correspond, plotted for a wavelength range

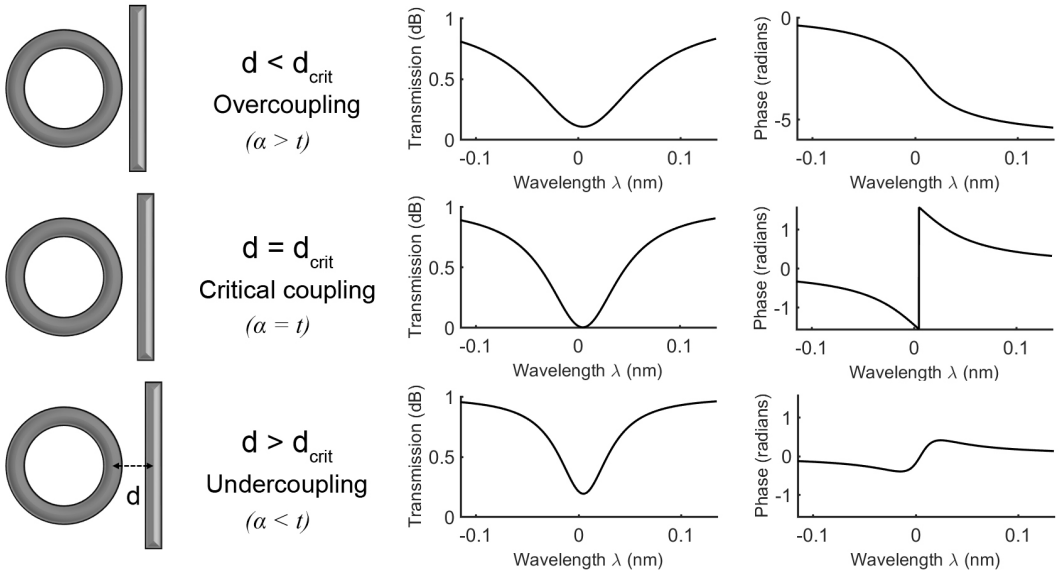

FIGURE 2.14: Coupling regimes and respective theoretical transfer functions of a ring resonator around the resonance wavelength (calculated in MATLAB from eq. (2.41)).

around the resonance point. The tunable parameters in the actual design process are related to the geometry of the device, therefore the description of the regimes below approaches different ring configurations that correspond to different $\{\alpha, t\}$ combinations. As shown in Fig. 2.14, for a given ring diameter and propagation loss per length (therefore fixed round-trip loss α), there exists a bus-ring gap d_{crit} for which light stays inside the ring structure the longest, completing the maximum number of round-trips. This gap corresponds to a t value which is equal to the value of α. This critical coupling condition ($\alpha = t$) is described by an ideally zero power level at the device output for the resonance wavelengths, while the phase experiences an abrupt π-radian phase shift. In the overcoupling ($\alpha > t$) or the undercoupling condition ($\alpha < t$), where the bus-ring gap is smaller or larger than d_{crit} respectively, the transmission trough is shallower at the resonance wavelengths, never reaching the zero value. As for the phase response, overcoupling corresponds to a π-radian delay, while undercoupling leads to a wiggle (Fig. 2.14).

Regarding the design of a modulator based on the ring resonator, an electro-refractive component can be incorporated in the waveguide section that forms the ring circumference. This enables modifying the effective refractive index n_{eff} through the application of voltage and the result of this variation is illustrated in Fig. 2.15. The transfer function is shifted in the wavelength axis as the values of n_{eff} are varied and therefore for a fixed-wavelength optical excitation to the ring system, the corresponding optical output can traverse through different intensity levels. The structure can thus function as an intensity modulator.

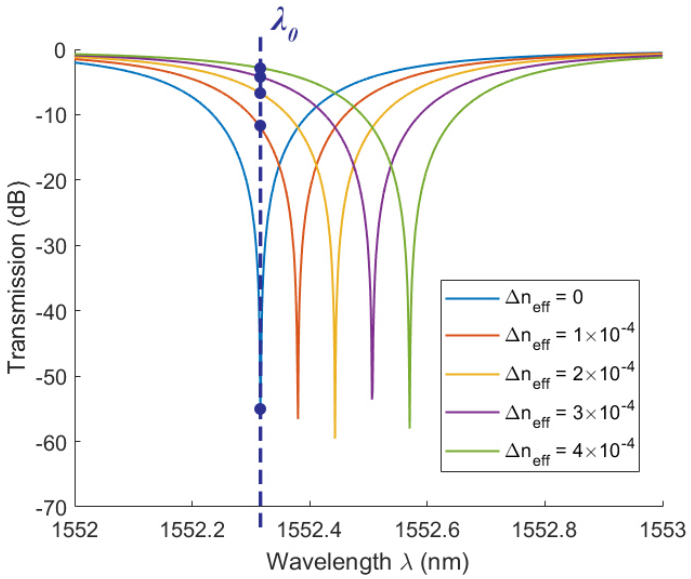

FIGURE 2.15: Transmission of a 24-μm-diameter ring resonator for different effective refractive index changes applied $\left(\{\alpha, t\} = \{0.8897, 0.8895\}\right)$ (calculated in MATLAB from eq. (2.42)).

2.1.5.3 Modulator performance metrics

In the previous sections, a thorough analysis of the optical components used to form intensity modulators was presented. It is however useful to also identify the metrics used to evaluate the performance of such electro-optic modulators from a device approach, in the context of a communications system. The metrics that are commonly used are listed below, where comparisons are drawn between the MZM and the RRM configurations, with a focus on the devices commonly fabricated on silicon platforms [62].

1. **Insertion loss:** The sources of loss in a modulator device are related to both the fundamental electro-optic component (p-n junction) and the structure that houses it (MZI or RR). The former can introduce losses due to the optical mode interacting with the rough sidewalls of the waveguide, as well as due to absorption caused by the interaction with free carriers in the doped silicon regions and any metal parts that are used for the electrode components. In terms of the intensity modulator topology, a MZM generally introduces higher loss compared to a RRM, because it includes long waveguides to form the MZI arms, as well as the splitter and coupler components.

2. **Modulation depth:** The modulation depth is defined as the ratio of optical output power levels corresponding to the ON and OFF states of the modulator. This is first dependent on the phase modulation efficiency of the electrorefractive component (phase shifter), which expresses the net phase shift induced for a given value of applied voltage, per phase shifter length. It should be noted that the

$\Delta\phi(V)$ function is not linear as the rate of phase change is reduced as the reverse bias voltage increases. Further than that, the modulation depth is determined by the amount of intensity variation induced by a certain phase shift. This is dependent on different parameters for the MZM and RRM devices. Regarding the MZM, longer MZI arms in principle lead to higher modulation depth, while in the case of RRMs, critical coupling is generally desirable to achieve the lowest possible intensity level for the OFF state. Finally, it should be noted that the achievable extinction ratio (ratio between the ON and OFF state power levels) also depends on the electrical properties of the electronics that comprise a fully packaged modulator, while it also differs significantly at higher modulation frequencies, due to bandwidth limitations. These parameters are described in more detail in the following paragraphs.

3. **Bandwidth:** The bandwidth of the modulator measures its ability to support a wide range of modulation frequencies. This is firstly related to the equivalent circuit of the fundamental phase shifting element which exhibits some RC time constant as a result of the capacitance components it includes. Secondly, it depends on the electrical properties of the electrodes used to apply voltage to the modulator. In the case of MZMs, the metallic contacts that span the full length of its arms constitute a set of Radio Frequency (RF) transmission lines whose design affects the datarates they can support. Regarding the MZMs, shorter devices usually show larger bandwidth. In the case of RRMs, no such travelling-wave electrodes are used and the electrical part of the device is treated as a lumped element. However, as the structure is a resonator, its photon cavity lifetime can be detrimental to the operating speed of the modulator when high-Q-factor rings are used.

4. **Wavelength selectivity:** If the modulator transmission exhibits variation with respect to wavelength, the operation of the device requires either the optical source to emit at a specific wavelength or an appropriate tuning mechanism for the modulator to adapt to the arbitrary input wavelength. The RRM always shows selectivity with respect to wavelength, as indicated by the plot in Fig. 2.13. However, a balanced MZM, which consists of arms of the same length, can exhibit nearly uniform transmission across the C-band.

5. **Chirp:** The chirp parameter expresses the variations in the output wavelength of the modulator, as a result of the phase changes that accompany the transitions between the different intensity levels. The disadvantage of producing chirped signals is revealed in long-haul transmission scenarios, where the chromatic dispersion of the optical fibre can significantly distort the signal. However, chirp is not always considered in the modulator design, as the development of silicon photonic modulators is usually aimed at short-reach interconnect applications. Signals produced by RRMs can exhibit chirp due to the phase response of the device [60]. However,

in the case of MZMs, driving both arms by a differential pair of electrical signals (push-pull configuration) can practically eliminate the chirp effect.

6. **Temperature sensitivity:** The design of modulators for the Silicon-on-Insulator (SOI) platform needs to take into account the large thermo-optic coefficient of silicon (1.8×10^4 K^{-1}). RRMs are particularly sensitive to temperature changes and an external active tuning mechanism is required to ensure stable operation. MZMs, on the other hand, are not particularly affected by temperature variations as the refractive index changes occur on both arms, thus eliminating the net effect on the output transmission.

7. **Footprint:** For silicon chips to accommodate photonic circuits of large complexity, the area occupied by the modulator device needs to be as small as possible. In this respect, the RRMs show an advantage as their diameter, which defines their largest dimension, can be as small as tens of microns. In the case of MZMs, the largest dimension is their arm length which usually spans hundreds of micrometers, or even reaches the millimeter scale.

8. **Power consumption:** Another important parameter is the power that is consumed by operating the modulator and it is often measured in units of energy consumed per bit of data. The electrical components that accompany a MZM are treated as a distributed circuit, where the travelling wave electrodes that drive the modulator are often terminated with a resistance (typically 50 Ω) to suppress any reflections. In this type of system, the drive voltage, the characteristic impedance and the bit rate ultimately determine the power consumption. In the case of a RRM, the electrical contacts constitute a lumped circuit element, therefore the power consumption is dictated by their capacitance and the drive voltage. Since no termination is used, reflections can be significant in this system and the drive voltage can be larger than the one applied to the ring. Additionally, any active tuning mechanism used to stabilise the RRM operating point also incurs consumption of electrical power, which should be taken into account in the total power consumption calculation. In particular, if the RRM resonance wavelength is shifted away from its optimal position in the λ-axis relative to the optical source wavelength due to some temperature change, an active tuning device (such as a heater) needs to constantly supply power (usually in the form of applied voltage) to maintain the λ-position of the RRM operation point.

It is clear that every silicon modulator contains electrical components in conjunction with the photonic structures that enable modulation. Especially in the case where a commercial transmitter unit is built, the modulator devices require appropriate packaging along with all the necessary electronic control circuits, which may differ from their preliminary versions that are typically used for experimental work in a research environment. This emphasises the importance of co-designing the electronic and photonic

components of an electro-optic modulator. The design steps related to the electronic parts of the modulator become clearer if a MZM with a p-n junction and metallic contacts that span the full length of its arms is considered. The driving signal is affected by the electrical behaviour of the p-n junction used for electro-refraction (equivalent circuit model per unit length), the travelling wave electrodes, as well as the type of packaging with the electrical signal source, which could involve wire bonding or flip-chip bonding. All these factors affect the power and the bandwidth of the electrical signal even at a stage prior to its conversion to the optical domain. Example microscope pictures of two fabricated modulators, in the MZM and the RRM configuration, are illustrated in Fig. 2.16.

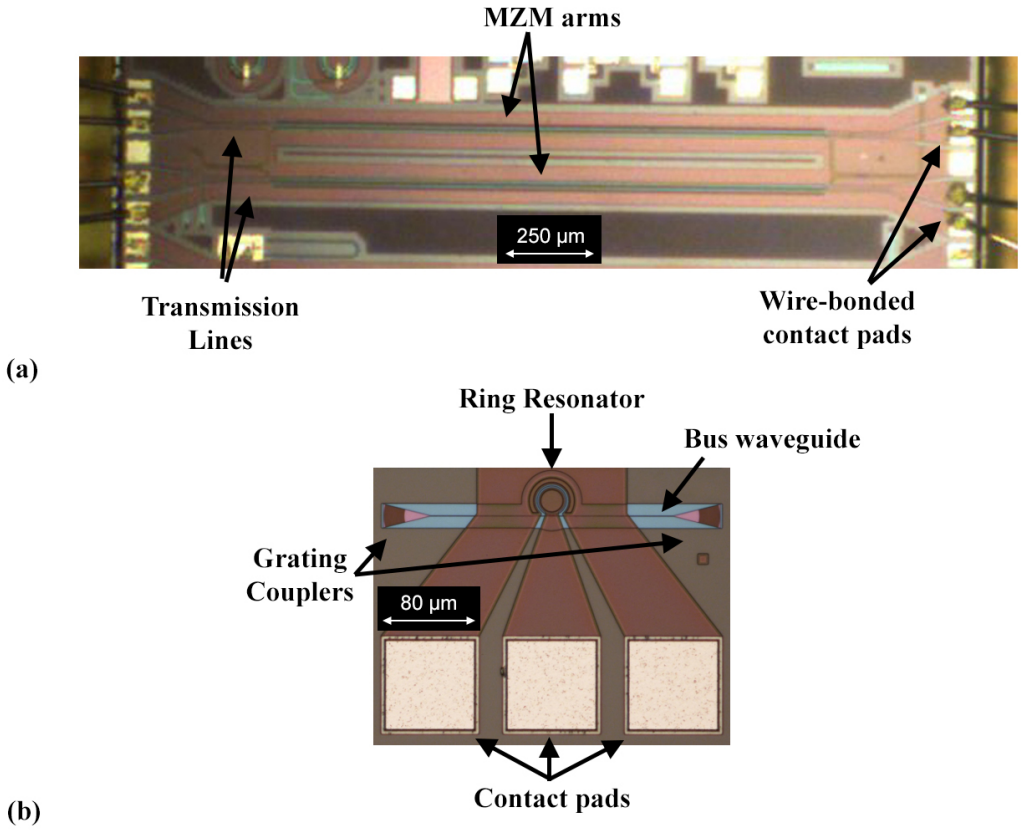

FIGURE 2.16: (a) Top view image of a Mach–Zehnder Modulator after its wire-bonding to a Printed Circuit Board (PCB), (b) Top view image of a Ring Resonator Modulator.

2.2 Optical Communication Systems

This section is dedicated to the Pulse Amplitude Modulation (PAM) and Discrete MultiTone (DMT) formats, as well as the linearity of a modulator and the techniques of its evaluation. The purpose of this section is to familiarise the reader with the relevant terminology, before the report on the experimental work. The section on the modulation formats includes an explanation of some key digital communications theory concepts,

along with a description of the actual implementation of the modulation formats in the author's experiments. It must be noted that basic knowledge about the fundamentals of digital telecommunications is necessary in following the explanations provided below. For more details on such systems, the reader can refer to [63].

2.2.1 Modulation Formats

The purpose of any digital communications system is to reliably transmit a set of binary data through a communication channel. The representation of information in this context is a sequence of bits, whose origin is irrelevant to the analysis of the communications system (output from a computer, an analog-to-digital converter, etc.) [63]. Under this consideration, a digital communications system is described by the block diagram in Fig. 2.17, where the transmitter Tx converts the digital bits to a time-dependent signal relating to some physical property, which is sent to pass through the channel with impulse response $h(t)$ and arrives at the receiver Rx. At the Rx stage, the received signal is converted to a bit stream again. The quality of this transmission is determined by the level of noise added to the signal throughout this process, which is here represented as $n(t)$. In the case of optical communications, the channel consists of the optical fibre and all optical components involved in transferring the electrical signal to the optical carrier in the C- wavelength band, according to the convention that Tx and Rx transmit and receive respectively an electrical signal (represented by changes in voltage). This incorporates the E/O modulators and the O/E photodetectors into the channel block and renders them the bottleneck in bandwidth, as the frequency of the optical carrier in a standard single-mode fibre (SMF) is of the order of hundreds of THz. It is also noted that these channels can be considered linear and time-invariant (LTI) for this analysis. In the following paragraphs, a description of the Tx-Rx pairs for the PAM-4 and DMT formats will be presented with block diagram schematics describing the steps in their software implementation process.

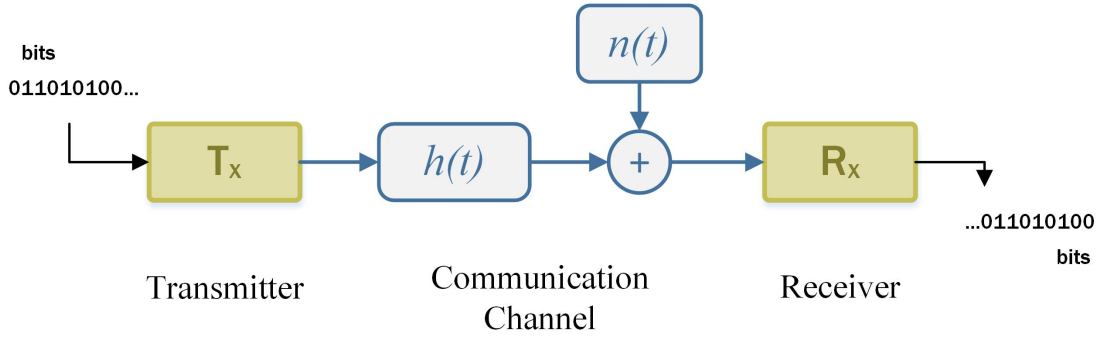

FIGURE 2.17: Block diagram of a digital communications system.

Pulse Amplitude Modulation (PAM) translates the binary data to a signal comprising multiple amplitude levels, or multiple levels of intensity in the case of optical signals.

Thus, if a symbol is defined as the smallest packet of information transmitted with a modulation format, the number of different symbols in a PAM format is the same as the number of levels used. For example, a PAM-4 format employs 4 intensity levels which correspond to 4 different symbols. Depending on the number of levels N_L in use, the number of bits mapped to a symbol is equal to $b = log_2 N_L$. This mapping is shown schematically on an intensity axis in Fig. 2.18.

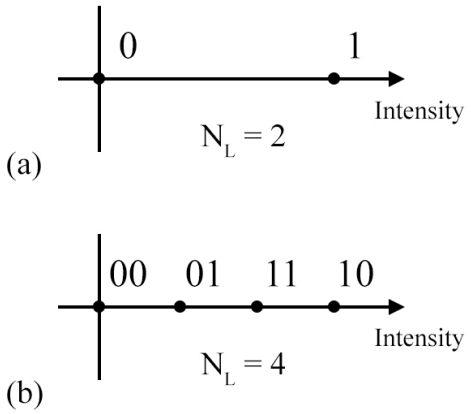

FIGURE 2.18: Constellation diagram for (a) a PAM-2 (or On-Off Keying - OOK) and (b) a PAM-4 modulation format in optical communications.

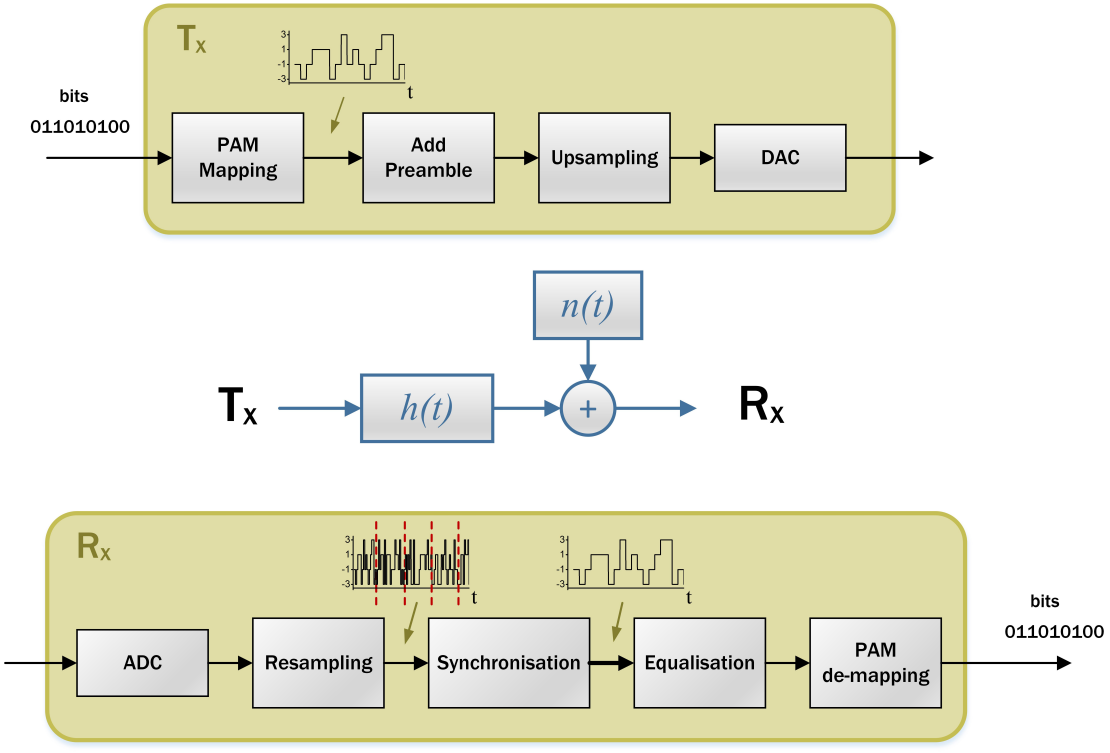

FIGURE 2.19: Block diagram of a PAM-4 system, consisting of the transmitter, the channel and the receiver.

The software implementations of the transmitter and receiver components for a transmission link using the PAM-4 format are represented with the block diagram in Fig.

2.19. The bit stream is usually generated as a Pseudorandom Binary Sequence (PRBS), which serves as one "frame" of data. This frame is first mapped to the PAM-4 symbols in order to create a PAM-4 waveform, to which a preamble is added in order to mark the start of the frame. Since this discrete-time waveform contains one sample per symbol, it is then appropriately upsampled based on the sampling rate of the Digital-to-Analog Converter (DAC) in order to match the desired symbol rate. After being sent to the DAC, the waveform is translated into a voltage signal and exists in the continuous-time domain. This waveform propagates through the channel $h(t)$ to finally be sent to the Analog-to-Digital Converter (ADC) of the receiver. The additive noise $n(t)$ represents all types of distortions that come from either optical components (laser source relative intensity noise, optical amplifier noise) or electrical components (noise from RF amplifiers, modulators, photodetectors, DAC, ADC). After passing through the ADC, the received signal is translated back to a discrete-time waveform and resampled appropriately to match one symbol per sample. At this point, a synchronisation algorithm searches for the preamble part in the waveform to identify the beginning and end of a frame and proceed to demodulate it. Finally, the frame is converted from a set of symbols to a bit stream using the reverse PAM mapping operation. The received bit stream can then be compared to the original transmitted one and a bit error ratio (BER) can be calculated.

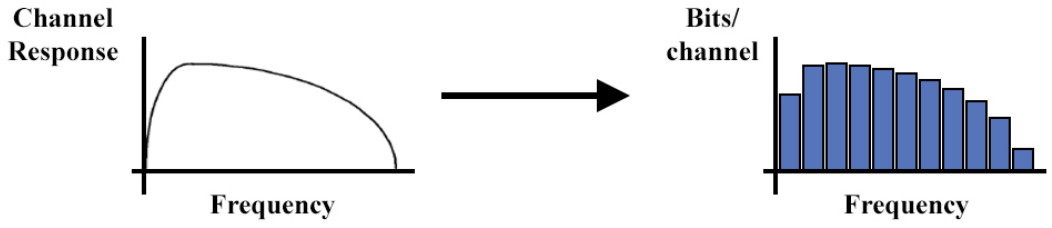

FIGURE 2.20: Data loading in a multicarrier modulation format such as DMT.

The implementation for DMT is more complicated than the one for PAM-4 because the symbols generated are allocated into different RF carrier frequencies instead of being sequentially transmitted in time. This multicarrier modulation is considered to tackle issues with Inter-Symbol Interference (ISI) which appear when conventional data formats are used in channels with a band-limited frequency response [63, 64]. The objective of multicarrier modulation formats is to use the available channel bandwidth as efficiently as possible and the strategy to achieve this is to divide the spectrum in a number of sub-channels, narrow enough for their individual frequency response to be considered flat (Fig. 2.20). Thus, data is parallelised and loaded to a number of subcarriers (usually in the form of QAM-modulated symbols). In the special case of DMT, information about the channel response is provided to the transmitter and this estimate is used to adaptively load the binary data to the sub-carriers so that the ones exhibiting relatively higher (lower) Signal-to-Noise Ratio (SNR) values are occupied by data modulated with

more (less) complex formats. This property makes DMT applicable to slowly time-varying two-way channels, such as telephone lines. This is in contrast to environments such as the one-way channels in broadcast applications where channel estimation is not available and bit loading is implemented in a uniform manner across the channel subcarriers, using the Orthogonal Frequency-Division Multiplexing (OFDM) format. In the case of optical communication channels, bandwidth constraints arise from the presence of electro-optic (E/O) components (modulators, photodetectors) as well as from the effect of power fading due to chromatic dispersion in relatively long-reach fibre links, therefore DMT enables the efficient use of the available bandwidth through its adaptive data loading. Another aspect of the DMT format is that it is designed to produce signals that can be transmitted by an intensity modulator and received through Direct Detection (DD) by a photodiode, without the need for any coherent system in the data recovery.

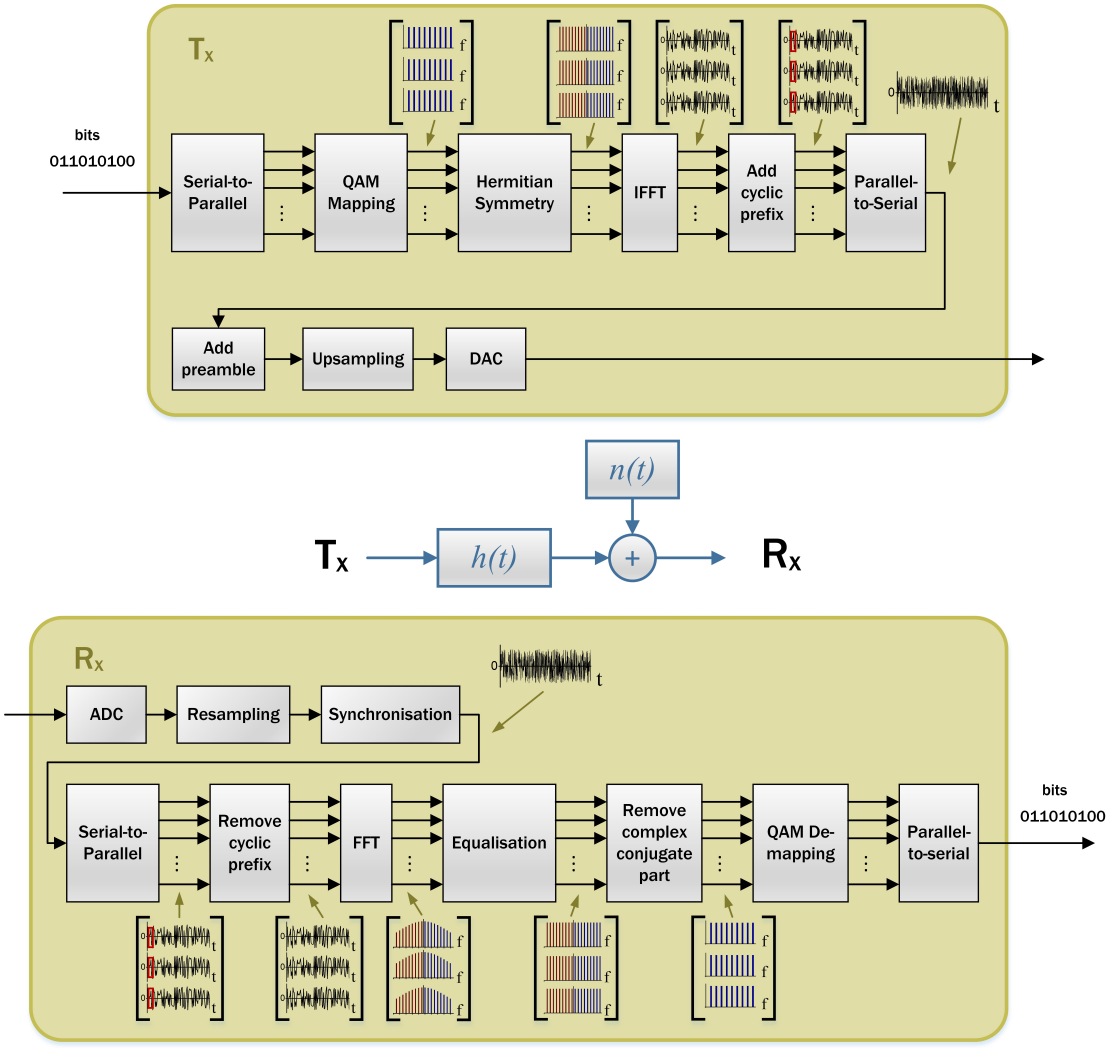

FIGURE 2.21: Block diagram of a DMT system, consisting of the transmitter, the channel and the receiver.

The software implementations of the transmitter and receiver components for a transmission link using the DMT format are represented with the block diagram in Fig. 2.21. Considering that channel estimation has already taken place, a water-filling algorithm is used to decide the order of the QAM modulation format used in each subcarrier based on its SNR value, hence the number of bits b_i per symbol for each of the subcarriers. Details of the water-filling algorithm used in this work can be found in [64], pp. 305-330. If N is the number of bits sent in the first frame of data and N_c is the number of subcarriers used, the binary sequence is sent to a Serial-to-Parallel block to be divided into N_c sets of bits. Each set carries as many bits as the QAM format selected by the water-filling algorithm allows to be transmitted in a single symbol. The bits are mapped to QAM symbols and a matrix of size $N_c \times M$ is created, where $M = \frac{N}{N_c}$. Each row of this matrix represents a signal in the frequency domain, whose time-domain representation is, in principle, complex. In order to render this signal real, another N_c carriers are added as the negative part of the frequency spectrum and the data on them are equal to the complex conjugate of the data in the positive part in order to satisfy the condition of Hermitian symmetry. The row-signals are then Inverse-Fast-Fourier-Transformed (IFFT) to produce a matrix of real-valued time signals. Each row now represents a DMT symbol in the frame. Since the frame has to be sent in a serialised form to the channel, the DMT symbols will have to be positioned in a successive order. Before this happens, a cyclic prefix is added to every signal-packet to provide a guard interval for the mitigation of ISI effects, while an additional preamble is added to mark the start of each DMT symbol. Finally, the last stages are the serialisation of the frame and its approriate up-sampling in order to be transmitted to the channel through the DAC. The same concepts apply for the channel as the ones described previously for the PAM-4 case. The received signal is captured by the ADC, re-sampled and each frame is identified through a synchronisation routine. These operations are applied in reverse at the receiver, i.e. the frame is parallelised, the cyclic prefix from each DMT symbol is removed and a FFT operation transforms the signal back to the frequency domain, in a $N_c \times M$ matrix. At this point, based on the estimate of the channel frequency response, an equalisation algorithm appropriately scales the data on different frequencies of the received signal. The negative part of the spectrum is removed and the QAM symbols on each carrier are mapped back into sets of bits, which are serialised into a single binary sequence.

As was mentioned in the beginning, the DMT format continuously adapts to the transmission channel in order to make efficient use of the available spectrum and maximise the total data rate. This is achieved by incorporating a step of channel estimation at the beginning of the transmission. An estimate of the channel frequency response can be quantified by first allocating uniform data to all the carriers and capturing the received signal, whose SNR profile follows the power fading of the channel, as shown in Fig. 2.22.

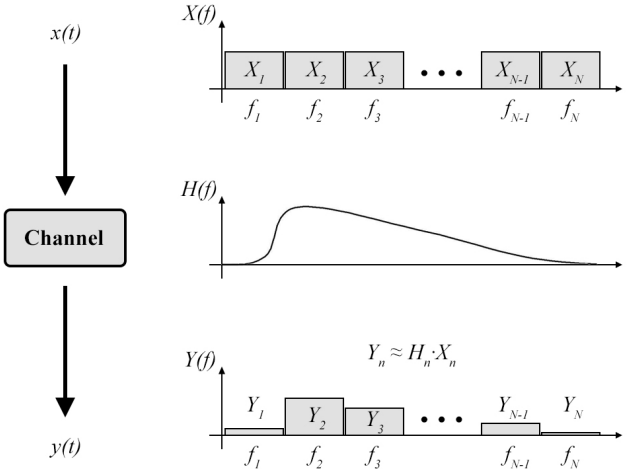

FIGURE 2.22: Channel frequency response estimation by transmitting uniformly allocated bits across all DMT subcarriers.

2.2.2 Analog links – modulator linearity

Although PAM and DMT formats allow for an increase in the capacity compared to conventional On-Off Keying (OOK) systems, they pose a new requirement for the components of a transmission link, which is that of high linearity in the input–output relation. Any optical communication system can be described by the block diagram illustrated in Fig. 2.23 (a). The input RF signal containing the information bits is converted to the optical domain through an E/O modulator, which in turn sends the optical signal to propagate through a length of fibre (system channel) in order to be received and converted back to the electrical domain by an O/E photodetector. Hence, the requirement for high linearity concerns all components of such a system, however, as shown in [65], the most prominent source of nonlinearity in real photonic links is the modulator. If a sinusoidal transmission curve is considered for the modulator, Fig. 2.23 (b) shows how the output optical signal relates to the input electrical signal. If a silicon modulator is expected to transmit data in a PAM or DMT format, a linearity optimisation at the design stage is essential. In the case of PAM-n, loading information on multiple intensity levels on the transmitter side creates the necessity for these levels to remain equidistant on the amplitude axis up to the point of the receiver equipment. DMT, on the other hand, generates an analogue signal with arbitrary intensity transitions in the time domain, thus showing a high Peak to Average Power Ratio (PAPR), which makes it more vulnerable to nonlinear distortions.

The silicon Mach–Zehnder Modulator is intrinsically nonlinear and the two main sources of its nonlinearity are: (1) the sinusoidal form of the interferometer transmission function and (2) the inherent nonlinearity of the carrier depletion mechanism used for electrorefractive modulation [66, 67]. As the block diagram in Fig. 2.24 shows, the $P_{opt}(V)$

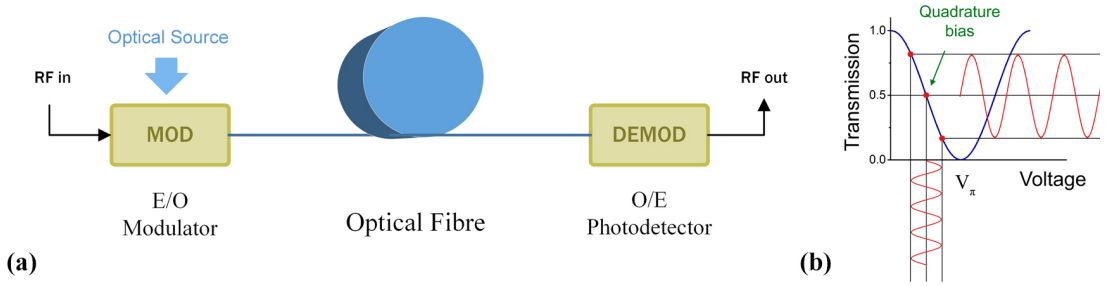

FIGURE 2.23: (a) Schematic of a photonic link, (b) Optical Power vs. Input RF voltage plot for an E/O modulator.

function that describes the E/O conversion is composed of two other functions: one linking the effective refractive index to the applied voltage $n_{eff}(V)$ and one linking the optical output power to the effective refractive index $P_{opt}(n_{eff})$. Therefore, the linearity of the E/O conversion depends on the linearity of both these functions that constitute the composite E/O function.

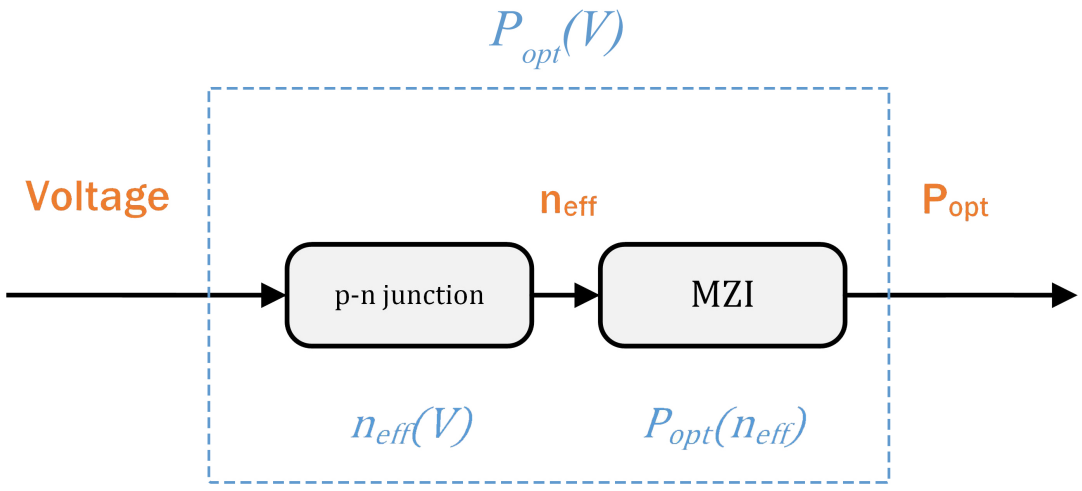

FIGURE 2.24: Block diagram of the E/O conversion stages of a MZM.

The most common technique used to evaluate the nonlinearity of a modulator involves driving it with a signal consisting of frequency tones and examining its spectral output. Before analysing this method, it must be noted that the analytical approach followed below applies to the presence of static weak nonlinearities, for systems with no memory effect or frequency dependence of the output nonlinear distortion components [68]. For these assumptions, the total E/O MZM transfer function $P_{opt}(V)$ is considered in the following mathematical analysis as an input-output function $y(x)$, where the variables y and x are used here to denote the modulator optical output P_{opt} and the electrical signal input V respectively [69]. By expanding the transfer function to a Taylor series around a bias point x_0, we have the following expression:

$$y(x) = \sum_{k=0}^{\infty} \frac{(x - x_0)^k}{k!} (\frac{d^k y}{dx^k})_{x=x_0} = \sum_{k=0}^{\infty} a_k (x - x_0)^k \tag{2.44}$$

where a_k are the expansion coefficients defined as

$$a_k = \frac{1}{k!} (\frac{d^k y}{dx^k})_{x=x_0} \tag{2.45}$$

It is noted that both y and x in these expressions are functions of time denoting the input and output signals of our system, while x_0 expresses the input bias. It is now useful to observe the output $y(t)$ for specific types of driving signals $x(t)$. The usual implementation of this nonlinearity evaluation technique involves driving the modulator with a set of two fundamental frequencies (ω_1, ω_2):

$$x(t) = x_0 + A[cos(\omega_1 t) + cos(\omega_2 t)] \tag{2.46}$$

where A is the arbitrary amplitude of the driving signal. Substituting eq. (2.46) to eq. (2.47) and considering the terms of $y(x)$ only up to the 3rd-order polynomials ($k = 3$), the frequency components produced by the modulator at its output stage are summarised in Table 2.1 [69]:

TABLE 2.1: **Nonlinear distortion components**

Component	**Frequency**	**Amplitude**
DC	0	$a_0 + a_2 A^2$
Fundamental	ω_1, ω_2	$a_1 A + \frac{9}{4} a_3 A^3$
Second-order harmonic (HD2)	$2\omega_1, 2\omega_2$	$\frac{1}{2} a_2 A^2$
Third-order harmonic (HD3)	$3\omega_1, 3\omega_2$	$\frac{1}{4} a_3 A^3$
Second-order intermodulation (IMD2)	$\omega_2 - \omega_1, \omega_1 + \omega_2,$	$a_2 A^2$
Third-order intermodulation (IMD3)	$2\omega_1 - \omega_2, 2\omega_2 - \omega_1, 2\omega_1 + \omega_2, 2\omega_2 + \omega_1$	$\frac{3}{4} a_3 A^3$

It can be observed that apart from the fundamental tones and an additional DC component, new frequencies arise with varying amplitude coefficients. These spurious components can be classified based on the position they occupy on the frequency spectrum (Fig. 2.25). Components at frequencies of integer multiples of ω_1 and ω_2 are called harmonic distortions, while the ones corresponding to sums and differences between the two fundamental frequencies are called intermodulation distortions. By observing their amplitudes, it is clear that the second-order intermodulation distortion (IMD2) is twice as large as the second-order harmonic (HD2) one, while the third-order intermodulation distortion (IMD3) is three times larger than the third-order harmonic (HD3) one. What is also observed is that the IMD3 components are the ones closest to the fundamental tones, making them the hardest to filter out, while the IMD2 components can appear close to the original tones or not, depending on the spacing between the latter. The

significance of this observation for a real application with a signal comprising a continuous spectrum of frequencies is that IMD3 is superimposed on some part of the signal bandwidth even in narrowband systems and therefore becomes the main cause of signal quality deterioration, while IMD2 can mainly affect wideband systems with multi-octave signals (where $\omega_{high} > 2\omega_{low}$).

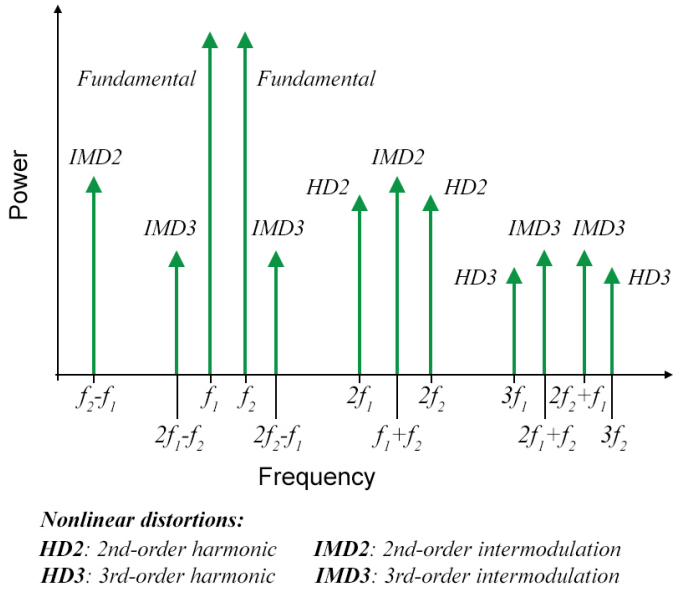

FIGURE 2.25: Output spectrum of nonlinear modulator with a two-tone signal input.

One of the most common parameters that are used as a metric of nonlinearity in a communication link is the Spurious-Free Dynamic Range (SFDR). SFDR expresses the output power dynamic range of the link, for which no intermodulation distortion of a given order is exhibited. However, to accurately interpret this definition, one must take into account the noise floor of the system. Under this consideration, SFDR_n can be defined as the maximum output SNR for which the IMD_n component power is below the noise floor. This is visualised in Fig. 2.26, which shows a plot of the RF output power of the fundamental and IMD_n components with respect to RF input power, in decibel scale. In this plot, the noise power spectral density (PSD) is marked and the SFDR_n is annotated as the difference (when plotted in dB) between the fundamental and IMD_n powers, when the IMD_n is equal to the noise power. Since the slope of the fundamental curve is equal to unity, SFDR can also be defined as the ratio of the input powers for which the two output components are equal to the noise power, as illustrated in Fig. 2.26.

It must be noted that citing a SFDR_n value must also be accompanied with the bandwidth at which the noise measurement was taken, as this affects the value of the noise power. Considering that the slope of the n-th order IMD component curve is n times larger than the slope of the fundamental curve, it can be proven that the relation of the SFDR_n value to the measurement bandwidth B is given by:

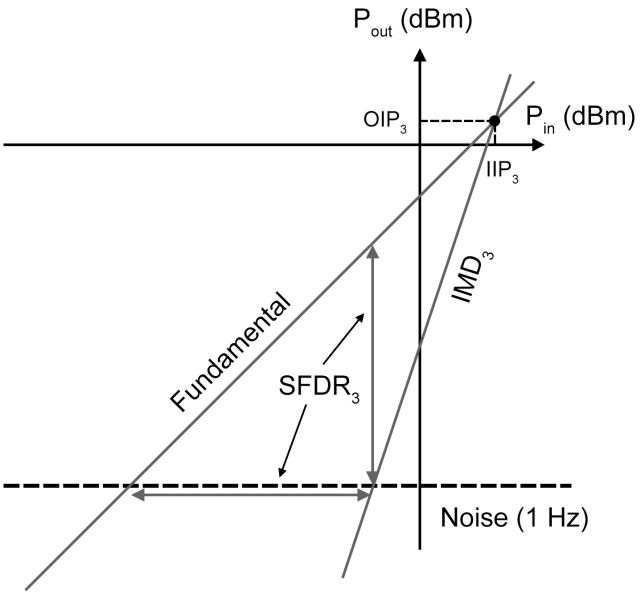

FIGURE 2.26: RF output vs. input power plot for a nonlinear system and $SFDR_3$ definition.

$$SFDR_n(B\ Hz) = SFDR_n(1\ Hz) - \left(\frac{n-1}{n}\right)10log_{10}(B) \tag{2.47}$$

Usually, a 1-Hz measurement bandwidth is considered and $SFDR_n$ is expressed in dB $Hz^{\frac{n-1}{n}}$, based on the scaling factor calculated in eq. (2.47).

Another parameter often cited as a metric of system nonlinearity is the intercept point of the fundamental signal curve and the n-th order IMD curve, considering a linear behaviour for the two curves. The quantities that are often cited to refer to the intercept point are either the n-th order input intercept (IIP_n) or the n-th order output intercept (OIP_n) which represent the corresponding input and output power values respectively and are illustrated in Fig. 2.26 for the 3rd-order IMD component.

Chapter 3

Grating Couplers for Systems involving Higher-Order Modes

Space Division Multiplexing (SDM) has attracted a lot of interest in research over the recent years, as a means of augmenting the available optical data transport network capacity, considering that existing techniques are proving insufficient to accommodate the rapidly increasing generated traffic [11, 12]. The implementations of SDM that have recently seen significant progress in the research community involve the use of either multi-core [70] or multi-mode fibres [71] which increase the available fibre capacity by allocating distinct data streams into different cores or modes, respectively. Considering the latter case, the development of systems based on Few-Mode Fibres (FMFs) also raises challenges in processing the multiplexed data, meaning that components able to realise inter-modal functionalities are required for the system design.

At the same time, the components present in modern communication data centres are making extensive use of the silicon photonic technology. In this context, merging the integrated component systems with the FMF-based networks appears to be an essential task that can be reduced to the design of two basic building blocks: an efficient interface between the FMF and the silicon photonic circuit and an integrated mode multiplexer. Interfacing the Silicon-on-Insulator (SOI) platform with a FMF can be achieved by means of grating couplers designed to be sufficiently large to accommodate the FMF spot size [72, 73]. As regards mode multiplexing, integrated components that implement this functionality entirely on the SOI chip have already been reported [74–76]. Another reported technique involves the chip-to-fibre interface to perform the mode conversion operation. On-chip waveguides with electro-optic phase shifters have been used to feed an array of small-scale gratings which are appropriately positioned in order to illuminate the comparatively larger FMF facet and thus excite higher-order Linearly Polarised (LP) modes [77–80].

Such mode multiplexers rely on the fundamental operation of mode order conversion. This chapter focuses on the design, simulation and characterisation of a fabricated grating coupler that is capable of converting the TE_0 mode of the waveguide to the LP_{11} mode of a two-mode fibre, with no requirement for additional integrated components. Because the conversion mechanism is related to the pattern design of the grating, the operation occurs entirely at the FMF-to-SOI interface. As a result, the design targets set for this work focused on maximising both the coupling efficiency and the conversion efficiency of the device. The first section describes the design strategy related to apodised grating couplers for high coupling efficiency, along with simulation results. The second section describes how the mode conversion operation is incorporated into the pattern and presents the simulation results of the corresponding 3D grating structure. The third section presents and discusses the experimental results of the device characterisation. The contribution of this work to the scientific community was the demonstration of the first fabricated mode-converting grating coupler [22], as the only previous report of the concept in literature presented simulation results, without any experimental verification [81].

3.1 Design & Simulation

Out-of-plane grating couplers (GCs) are a common type of interface between silicon chips and fibre systems which utilises the diffraction of light by an etched groove pattern to change the direction of a waveguide mode and send it towards a vertically positioned fibre (Fig. 3.1 (a)). Since the direction of a wave is expressed by its phase characteristics, the pattern itself is determined by the spatial phase functions of the two modes to be coupled. In particular, if $\phi_{mode,waveguide}(x,z)$ and $\phi_{mode,fibre}(x,z)$ are the phase distributions of the in-plane mode propagating along the grating part of the waveguide and of the fibre mode on the chip plane (the x-z plane in Fig. 3.1) respectively, then the individual scatterers comprising the grating are situated at the points where $\phi_{mode,waveguide}(x,z) = \phi_{mode,fibre}(x,z)$. This phase-matching condition can be used to design grating couplers for any waveguide-fibre mode pair. Hence, to incorporate an additional mode order conversion operation to the coupler, it is sufficient to use the spatial phase function of the desired higher-order mode in the phase-matching equation. Thus, converters to any arbitrary higher-order fibre mode can be designed, as demonstrated previously in [81] and [82].

Regarding the specific case of the TE_0-to-LP_{11} conversion, the solution to the phase-matching equation forms the structure shown in Fig. 3.1 (b). The periodic groove pattern on one side of the grating is offset with respect to the one on the other side by a distance that is equal to half their spatial period. Thus, the optical mode propagating in the waveguide acquires a π phase difference along the x direction as it interacts with the grating and the resulting phase profile of the electric field that is diffracted upwards

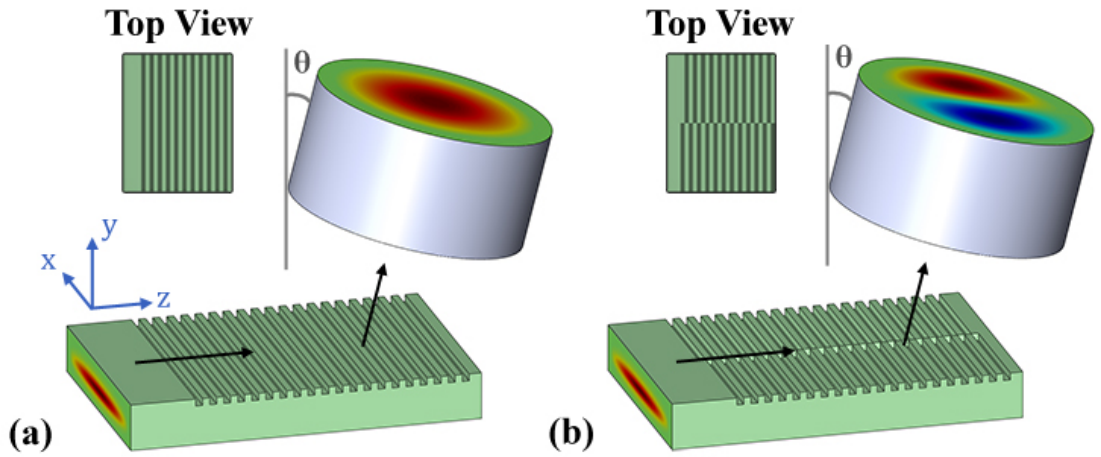

FIGURE 3.1: 3D concept of the grating-fibre interface for (a) a regular grating pattern, (b) a mode-converting grating pattern (dimensions not to scale). Insets: Top view of the gratings.

matches the profile of a LP_{11} fibre mode. This also applies to the reciprocal operation of a fibre mode being launched to the grating in order to be coupled to a waveguide mode.

The phase-matching condition that was described in the previous paragraphs helped in conceptualising the structure of a TE_0-to-LP_{11} GC and acknowledging the key element of the half-period offset. In practise, to further optimise the design of the device in terms of coupling efficiency, the diffracted light must also match the Gaussian intensity profile of the fibre mode. Therefore, a pattern with variable periodicity was used and the design strategy involved simulation work. The full design methodology is presented next in two parts: the first part describes the apodisation method used to achieve the highest possible coupling efficiency for a regular SOI grating, measured through simulations, and the second part reports the implementation of the offset to a 3D-simulated apodised GC and presents results for the mode conversion operation, in the form of diffracted field profile patterns.

3.1.1 Apodisation technique

The first design step was the maximisation of the waveguide-to-fibre coupling efficiency for a regular grating ($TE_0 \leftrightarrow LP_{01}$) through apodisation of the groove pattern. As seen in the structures illustrated in Fig. 3.2, the trench length was set to vary, in order to manipulate the strength of diffraction across the length of the grating. This apodisation method is a common technique used to improve the coupling efficiency between a waveguide and a fibre. Its effect is more intuitively understood when the interaction of an input waveguide mode with the grating is considered. The first grooves with which the optical mode interacts only allow a small portion of the optical power to be radiated upwards, while the next ones are designed to gradually increase the diffracted power along the grating length. This is shown in both structures of Fig.

3.2 by the gradual increase in the arrow lengths which represent the magnitude of the diffracted light. This enables shaping of the intensity profile along the z-direction, so that the diffracted light can match the Gaussian-shaped intensity profile of a fibre mode and the coupling efficiency can be improved.

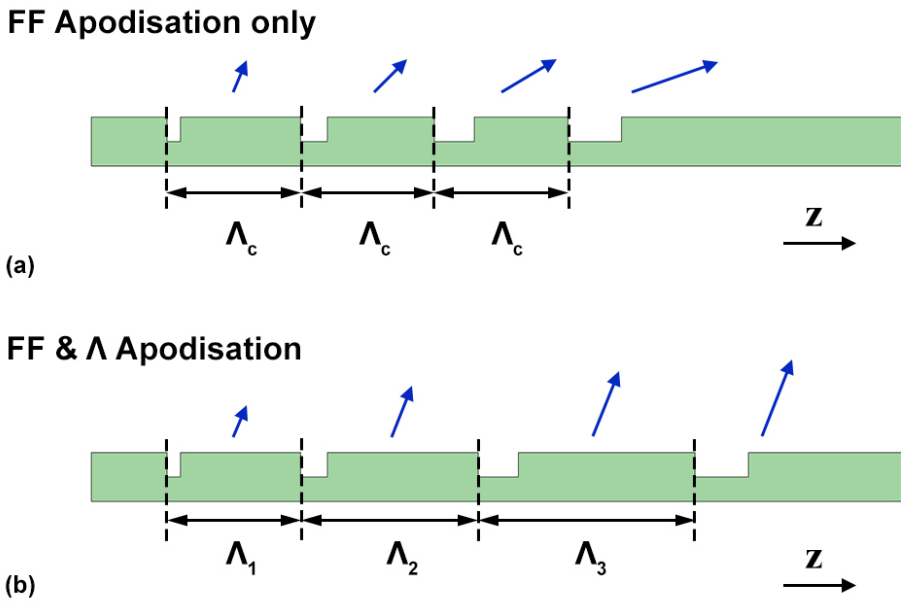

FIGURE 3.2: (a) Grating with apodised filling factor and constant period, (b) Grating with apodisation on both the filling factor and period. The arrows signify the direction of the diffracted light, whose magnitude is represented by the arrow length.

However, considering that each trench-tooth pair of period Λ is an individual scatterer, modifying the trench size while retaining the same periodicity does not guarantee a uniform direction of propagation for the diffracted wave along the structure (see Fig. 3.2 (a)). This is clearer if we consider that the effective refractive index for each scatterer is equal to:

$$n_{eff} = F \cdot n_{eff,u} + (1 - F) \cdot n_{eff,e} \tag{3.1}$$

where F represents the filling factor of the scatterer, given by the ratio of the unetched length L_u over the scatterer period Λ and $n_{eff,u}$ and $n_{eff,e}$ are the effective refractive indices of the unetched and etched part of the silicon slab respectively. Then, n_{eff} extracted from eq. (3.1) can be substituted in the diffraction equation for the first-order Bragg condition:

$$\Lambda = \frac{\lambda_c}{n_{eff} - sin\theta_{air}} \tag{3.2}$$

where λ_c represents the coupling wavelength of the diffracted light and θ_{air} expresses the angle of diffraction. It is clear from this equation that the period Λ of each scatterer

is dependent on its filling factor F through the n_{eff} term if the angle of diffraction θ_{air} is to be kept constant along the structure. In the specific case of a linearly apodised GC, the filling factor at an arbitrary position z along the grating can be expressed by the equation:

$$F = F_0 - R \cdot z \tag{3.3}$$

where F_0 represents the filling factor of the first scatterer and R is the linear apodisation factor, representing the filling factor change per unit length (measured in μm^{-1}). Equations (3.2) and (3.3) show that for linearly apodised scatterers with identical Λ, such as the structure shown in Fig. 3.2 (a), light of a specific wavelength is diffracted towards different angles θ_{air} across the length of the GC, because of the gradual change in n_{eff}. In order to maintain the directionality, Λ has to be modified in the z-direction according to eq. (3.2) so that the Bragg condition is satisfied for the full length span of the GC. Such a structure is illustrated in Fig. 3.2 (b) and it is the one that was considered in the design stage of this work. This technique is described and discussed in more detail in [50].

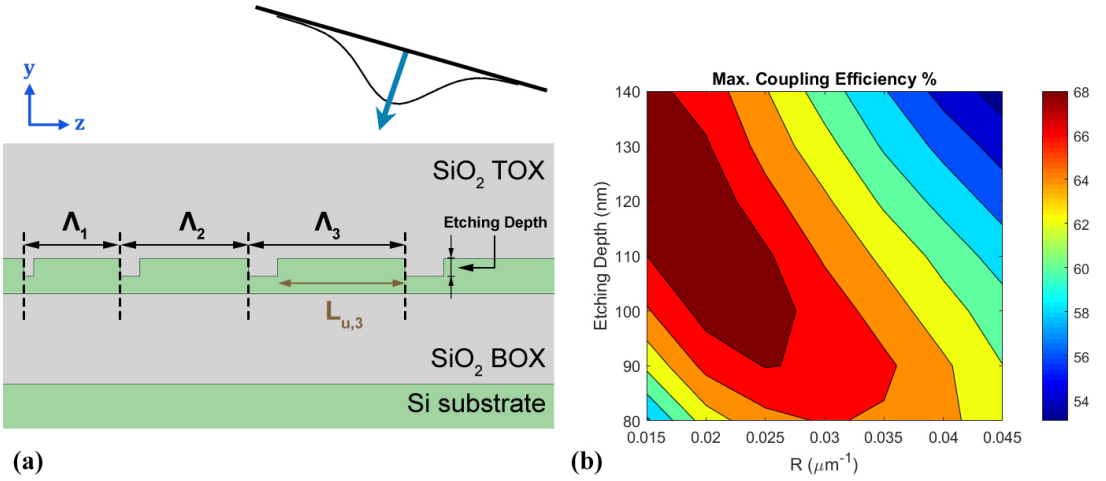

FIGURE 3.3: (a) Side view of an apodised grating, as simulated in FDTD Solutions (TOX: Top Oxide Layer, BOX: Bottom Oxide Layer), (b) Contour plot of the maximum coupling efficiency with respect to the etching depth and the linear apodisation factor R.

To quantify the coupling efficiency of this type of GC, the 2-D structure shown in Fig. 3.3 (a) was simulated with the Finite Difference Time Domain (FDTD) method using the software FDTD Solutions provided by Lumerical^{TM}. This represents the cross-section of the grating in the y-z plane, which is enough to simulate the diffraction effect without loss of generality, as the pattern is assumed to be homogeneous along the x-direction at this stage. The parameters of the structure were based on the specifications of the available SOI wafers and fabrication processes. Therefore, the silicon thickness of the structure was selected to be 220 nm, which corresponds to waveguides supporting Transverse

Electric (TE) modes at $\lambda = 1550$ nm. The silicon device is surrounded by silica (SiO_2), in the form of a top cladding layer of 720-nm thickness and a bottom 2-μm-thick layer. The etching depth, periodicity and length of the trenches were left as free parameters to optimise based on the implemented apodisation technique. Regarding the method employed to evaluate the coupling efficiency, the optical input was set to originate from an out-of-plane fibre to be launched towards the grating and then propagate in-plane along the waveguide, where the coupled optical power can be monitored. For this, an optical source with a Gaussian-shaped intensity profile was selected in order to resemble the fundamental mode of a commercial two-mode fibre, while the beam waist was set to 10 μm based on the reported mode field diameter (MFD) of 20 μm. This beam was incident on the grating at an angle of 14.5° relative to the chip surface normal so as to ensure unidirectional propagation in the waveguide. It is also noted that the optical source was set so that it takes into account the evolution of the beam waist originating from a fibre positioned above the chip and impinging on the top oxide layer (TOX) (Fig. 3.3 (a)). The distance of the fibre core facet from the grating pattern was calculated to be ~16 μm, based on the feasible physical positioning of the full fibre structure, which includes the 125-μm-diameter cladding, at the 14.5° angle. The mode was allowed to propagate over a distance of 10 μm along the waveguide inside the simulation space.

Based on these specifications, a campaign of 2D-FDTD simulations was run on the y-z plane to sweep the etching depth and the apodisation factor of the GC. The results of the sweep are summarised in the contour plot of Fig. 3.3 (b). The plot suggests that the maximum achievable coupling efficiency for this SOI configuration is 68%, while it also reveals the robustness of this design, as the coupling efficiency value changes only by 2% for an etching depth variation of ±10 nm. Therefore, the optimum parameter pair was selected for this work which indicated an etching depth of 110 nm and an apodisation factor value $R = 0.020\ \mu m^{-1}$.

3.1.2 Groove positioning for mode order conversion

The next step of the design aimed to add the mode conversion capability to the device. For this reason, the optimum apodised grating coupler was constructed in FDTD Solutions as a 3D structure. First, the width of the grating was set to 20 μm in accordance with the spot size specifications of a commercial two-mode fibre. Next, the appropriate z-offset was introduced to one side of the GC. In particular, a set of 22 apodised scatterers corresponding to the optimum design mentioned in the previous section was set to comprise the Right Hand Side (RHS) of the GC, as illustrated in Fig. 3.4 (a), while the scatterers on the Left Hand Side (LHS) needed to exhibit a half-period ($\Lambda_{R,i}/2$) offset relative to the RHS to introduce the π phase shift. Since the RHS had a variable $\Lambda_{R,i}$, the offset used was also variable, different for each individual scatterer. The LHS trench positions are indicated with the blue points in Fig. 3.4 (a) at the centre points of each

RHS scatterer and thus they defined the variable period $\Lambda_{L,i}$ of the 22 LHS scatterers. Then, the filling factor values for the LHS part $\{F_{L,i}\}$ were calculated using the Bragg condition equation (3.2) so that the directionality of the GC is maintained. The final groove pattern for the two sides of the GC is given in Table 3.1.

TABLE 3.1: **Trench positions and sizes**

	Right		Left	
No.	Pos. (nm)	Size (nm)	Pos. (nm)	Size (nm)
1	0	61	305	65
2	610	69	916	72
3	1222	76	1528	80
4	1835	84	2143	88
5	2450	92	2759	96
6	3067	100	3377	104
7	3686	108	3996	112
8	4306	116	4617	120
9	4929	124	5241	128
10	5553	132	5865	136
11	6178	140	6492	144
12	6806	149	7121	153
13	7436	157	7751	161
14	8067	165	8384	170
15	8700	174	9018	178
16	9335	183	9654	187
17	9972	191	10292	196
18	10611	200	10932	205
19	11252	209	11574	213
20	11895	218	12218	222
21	12540	227	12864	232
22	13187	236	13512	241

To evaluate the coupling efficiency of this mode converting grating, 3D-FDTD simulations were performed, in which a LP_{01} beam was launched to the grating and the power coupled to the waveguide was monitored. This type of calculation was conducted for apodised designs of both a regular GC and a mode converting GC and the resulting coupling efficiency curves are plotted with respect to wavelength λ in Fig. 3.4 (b). The peak efficiency values observed for the two types are 68.4% (-1.7 dB) and 55.6% (-2.6 dB) respectively, which are slightly higher than the numbers previously reported in literature [81], namely 60.4% (-2.2 dB) and 51.5% (-2.9 dB). Another conclusion drawn from these plots is the presence of a 0.9-dB conversion penalty that is present as additional loss in the mode converter design. Careful study of the simulated electric field propagation revealed that the additional loss arises from a portion of optical power that is incident on the discontinuity in the centre of the grating pattern (between the LHS and RHS parts), which appears to experience refraction towards the substrate without coupling into the waveguide.

The reverse operation was also simulated, where a TE_0 waveguide mode was sent to the grating and out-scattered to a TE_1-shaped mode which can subsequently be coupled

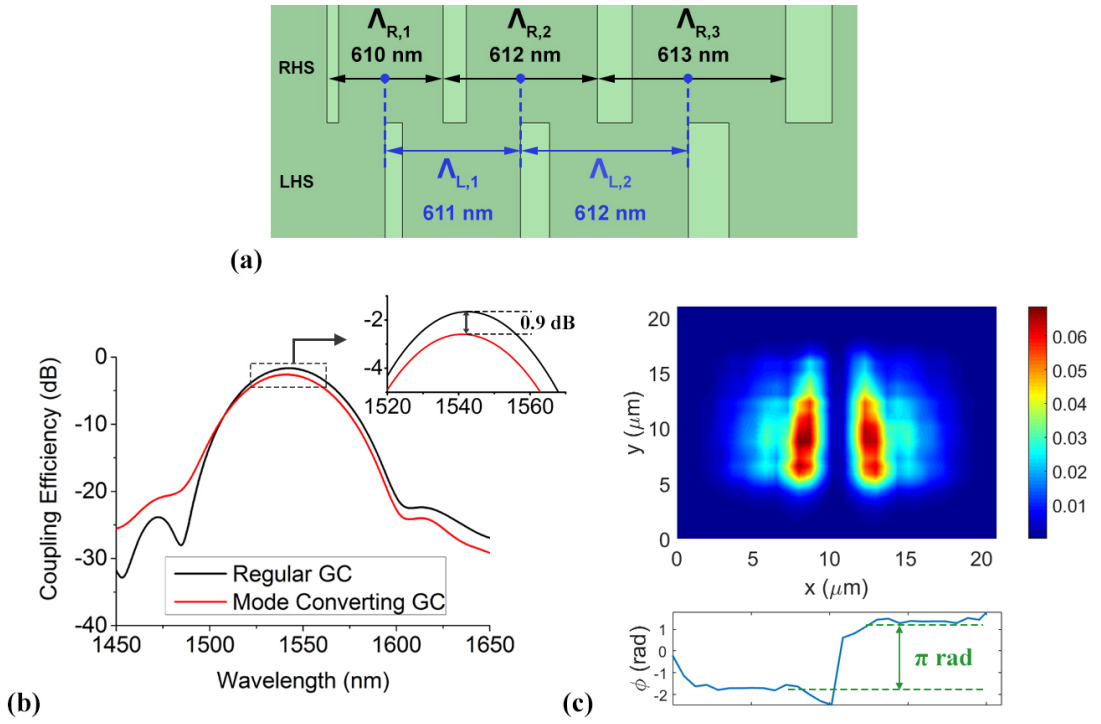

FIGURE 3.4: (a) Top view of the middle area of the mode-converting grating, where the right-hand side and left-hand side patterns meet, (b) Simulated coupling efficiency for a regular and a mode-converting grating coupler, (c) Intensity profile at the output plane above the grating and phase profile at y = 10 μm after conversion of TE_0 to out-of-plane TE_1 (compatible with LP_{11}).

to a LP_{11} fibre mode. The power diffracted upwards at a 14.5° angle relative to the normal was monitored and the resulting intensity profile is shown in Fig. 3.4 (c). It is clear that two intensity lobes are created as a result of the phase shifting between the two parts of the grating, creating an intensity null in the middle. The phase profile of the x-component of the electric field $\mathbf{E_x}$ is also plotted on the bottom, confirming the induced π phase difference.

3.2 Device Fabrication and Characterisation Experiment

The grating coupler design was then fabricated on a SOI wafer and characterised in order to experimentally verify its functionality. The device fabrication was conducted in the facilities of the Optoelectronics Research Centre (ORC) by Dr. David J. Thomson, Dr. Abdul Shakoor and Dr. Ali Z. Khokhar for the Silicon Photonics for Future Systems (SPFS) project. The characterisation experiments were performed by the author with the help of Dr. Cosimo Lacava and the useful guidance of Dr. Yongmin Jung.

The specifications of the SOI wafer included a 220-nm-thick silicon layer on top of a bottom oxide layer (BOX) of a 2-μm thickness, made of SiO_2. The structures were drawn on a resist film using electron beam lithography and the photonic circuit was

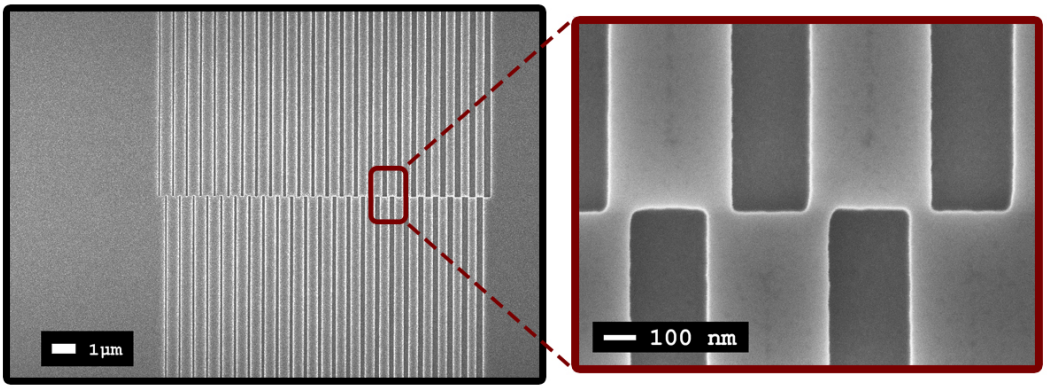

FIGURE 3.5: Scanning Electron Microscope (SEM) image of the mode-converting grating (top view).

then formed on the silicon layer of the wafer by means of inductively coupled plasma (ICP) etching. As a final stage, a layer of SiO_2 was deposited on top of the etched elements, which had a thickness of 730 nm. A top view of the resulting structure is depicted in Fig. 3.5, as captured by a Scanning Electron Microscope (SEM).

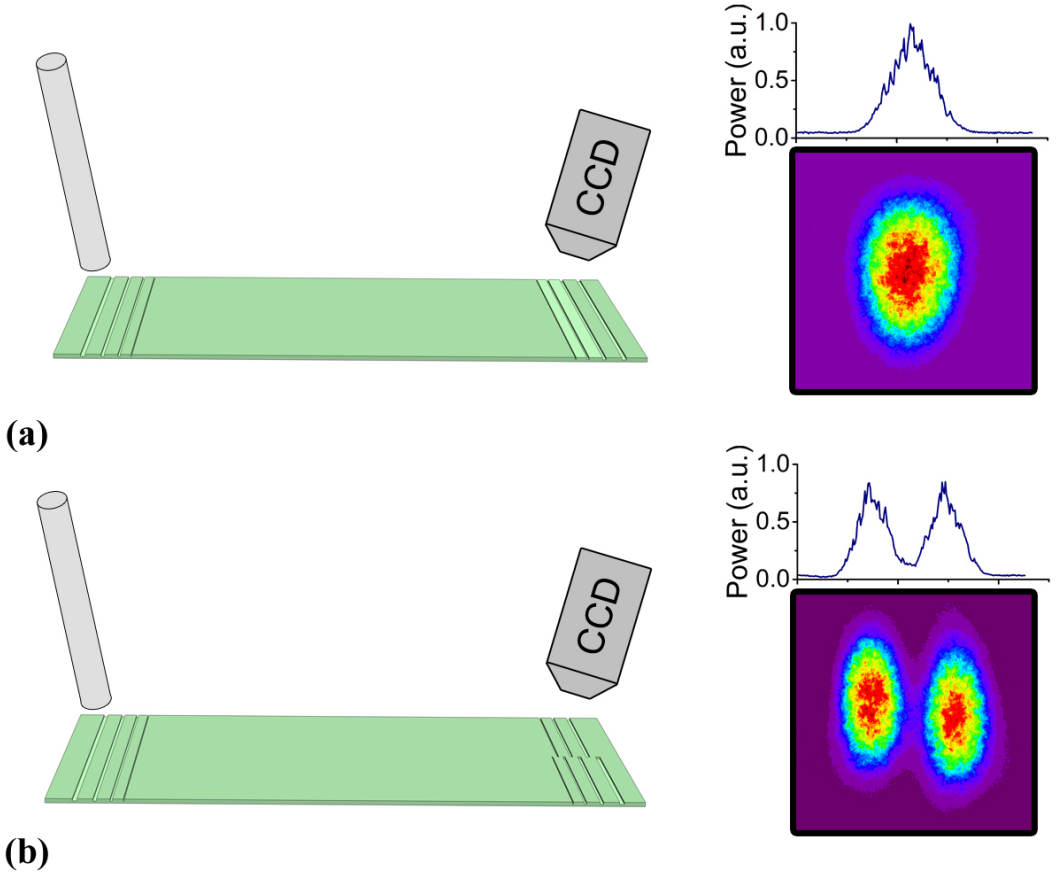

FIGURE 3.6: Characterization setup and recorded output far-field patterns for waveguides interfaced with (a) a pair of regular gratings and (b) a regular and a mode-converting grating.

Two types of devices were drawn on the layout of the silicon chip in order to perform characterisation measurements. Each of them consisted of a waveguide connected to two GCs that served as the input and output (I/O) interface with the external fibre system. The first device type, drawn schematically in Fig. 3.6 (a), contained two regular apodised grating couplers, whereas the second type, drawn in Fig. 3.6 (b), included the mode converting grating at its output coupler. The first characterisation experiment aimed to record the far-field patterns at the output of the designed GCs and the system that was set up for this measurement is shown in Fig. 3.6 (a), (b). The optical input to the waveguides was provided by a wavelength-tunable external cavity laser with a fixed-polarisation output. This was sent to a single-mode polarisation-maintaining (PM) fibre that was appropriately set up to launch TE-polarised light (comprising only the $\mathbf{E_x}$ component) to the input GC and therefore excite the TE_0 mode of the waveguide. At the output side, an objective lens was placed at an angle above the grating pattern so that the far-field pattern of the diffracted light can be imaged through an infrared (IR) camera.

The far-field patterns recorded for the two types of devices are plotted in Fig. 3.6 (a), (b). The device comprising regular I/O grating couplers did not cause any alteration to the mode order, which is evident by the single-lobed intensity profile recorded at its output. In the second device, the TE_0 mode that propagated through the waveguide was converted at the output grating stage, hence the diffracted TE_1-shaped profile exhibits two intensity lobes as a result of the phase change causing the cancellation of the electric field present in the middle. In this form, it can be coupled to the LP_{11} mode of a fibre. In order to also quantify the modal purity of the converted output, the power profile along the horizontal line that bisects the mode is plotted in Fig. 3.6 (b) above the far-field pattern. The intensity in the region between the two lobes would ideally be zero for a pure TE_1 diffracted profile, therefore the maximum-to-minimum intensity ratio was the evaluated metric to characterise its purity and it was measured to be 8.6 dB.

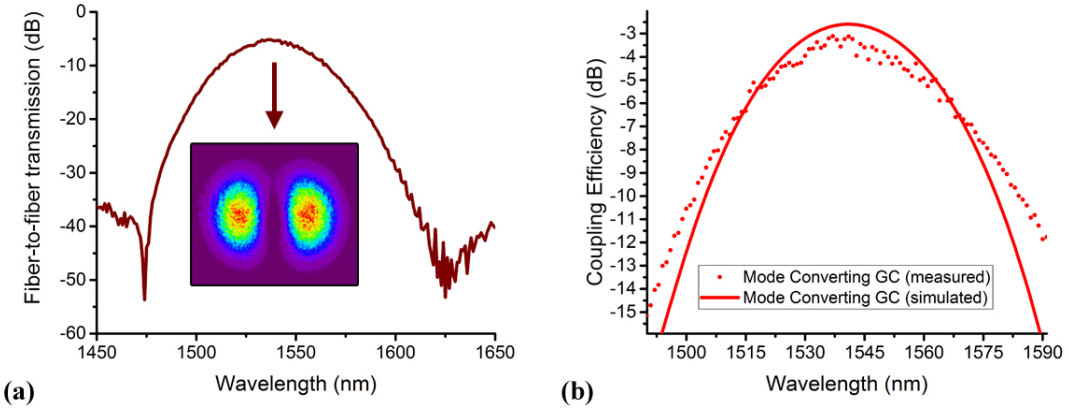

FIGURE 3.7: (a) Fibre-to-fibre transmission for the mode-converting device (inset: far-field pattern at the output of the two-mode fibre), (b) Extracted (and simulated) coupling efficiency for the mode-converting grating coupler.

Finally, the waveguide-to-fibre coupling efficiency as well as the power penalty of the mode conversion operation were evaluated by coupling the silicon devices to 1 metre of a commercial graded-index two-mode fibre. For each of the devices in Fig. 3.6 (a), (b), the fibre-to-fibre transmission was measured by sweeping the input wavelength and the result corresponded to the insertion loss of a pair of gratings. This transmission is plotted in Fig. 3.7 (a) for wavelengths spanning the whole C-band and showed a 3-dB bandwidth of 42 nm. The peak value of -5.2 dB at 1537 nm observed in this plot therefore corresponded to the total insertion loss for the pair of gratings shown in Fig. 3.6 (b). In order to verify the excitation of the LP_{11} mode in the fibre, the far-field pattern at the output of the fibre was also recorded and is depicted in the inset of Fig. 3.7 (a). This measurement also enabled to quantify the purity of the excited mode, which was evaluated by the same method mentioned in the previous paragraph. The peak-to-trough intensity ratio was measured to be 13.8 dB for this pattern, indicating a higher modal purity compared to the results of the previous experiment. This difference can be attributed to the slightly different setup constructed to capture the far-field pattern in the two cases, as the capturing system used for the GC output consisted of a more complicated array of lenses to image the resulting pattern to the IR camera.

Next, the transmission measurements for the two device types were used in conjunction to extract the coupling efficiency of a single grating. In particular, a transmission measurement for the regular GC pair was divided by 2 (in dB scale) given that the two GCs are identical in order to extract the efficiency for a single regular GC. Using this measurement as reference (peak value -1.8 dB, not plotted here) along with the transmission curve in Fig. 3.7 (a), the coupling efficiency of the mode converting GC was extracted and is plotted with respect to wavelength in Fig. 3.7 (b). The simulation prediction is also presented in the same plot for comparison. The two plots both exhibit peak values at a central wavelength of 1540 nm which correspond to -3.1 dB and -2.6 dB of coupling efficiency for the fabricated and the simulated GCs respectively. The slight mismatch in these peak values is attributed to unaccounted losses associated with the fibre facets in the experimental system used for the measurement. Finally, using again the extracted efficiency for the regular GC as a reference measurement, the power penalty of the conversion operation was calculated as equal to 1.3 dB which is close to the 0.9 dB prediction at the simulation stage.

3.3 Conclusion

This chapter reported the design and characterisation of a fabricated silicon grating coupler that operates as a mode order converter with the specific demonstration of the TE_0 to LP_{11} conversion. The concept was based on applications combining multimode fibre networks with integrated silicon components and the design targets were the optimisation of the coupling efficiency and the conversion efficiency.

The first section described the design strategy and presented simulation results. It was divided into two parts: the apodisation technique used to improve the coupling efficiency and the implementation of the mode conversion functionality. The second section provided information about the fabrication procedure and reported the experimental results for the characterisation of the silicon devices. The main results included a -3.1 dB coupling efficiency for a single mode converting grating coupler, with a conversion penalty of 1.3 dB. Far-field patterns of the converted modes were also presented corresponding to both the output of the grating structure and after propagation in 1 metre of a commercial two-mode fibre.

This work demonstrated the implementation of a TE_0 to LP_{11} conversion entirely at the coupling stage between a SOI chip and a two-mode fibre using an appropriately tailored grating pattern and it was the first result involving a fabricated mode conversion device with a single grating reported in the literature.

Chapter 4

Frequency Comb Generation based on a Ring Resonator Modulator

Over the last decades, the efforts to increase the capacity of optical communication links have very often involved the implementation of Wavelength Division Multiplexing (WDM) [83, 84], where the use of multiple carriers can compensate for the hardware-related limitations in bandwidth, mainly present in the E/O conversion stage. Especially in the field of silicon photonic transceiver design, a significant number of commercial solutions have adopted the use of multiple carrier wavelengths to achieve the >100 Gb/s capacity per transceiver-unit goal [19–21, 85]. Although this is often achieved with arrays of Distributed Feedback (DFB) lasers which operate separately from one another, the concept of using a single laser input fed to an optical frequency comb generator has also attracted significant interest in research [86, 87].

Frequency combs at optical wavelengths have received increased attention in recent years as a disruptive technology in spectroscopy and metrology applications, owing to the rapid advancement offered by the development of nonlinear microresonator devices [88]. At first glance, the adoption of such technology in the telecommunications sector appears to be a difficult feat due to the strict requirements in robustness and reliability set by the community regarding potential commercial comb devices. However, recent steps that the research community has taken into investigating comb generation are rapidly bringing the technology to a very mature stage, with implementations in WDM transceiver environments already being reported in the literature [89–91].

Most reports in the literature have utilised the Kerr nonlinearity of materials such as Silicon Nitride (Si_3N_4) [92–94], Silica (SiO_2) [95, 96], Diamond [97], Gallium Phosphide (GaP) [98, 99], Aluminium Nitride (AlN) [100, 101] and more recently Lithium Niobate ($LiNbO_3$) [91], all based on integrated platforms. Some of these material platforms

involve sophisticated fabrication processes, while others are better candidates for mass production of low-cost components. Silica- and silicon nitride-based solutions, which are compatible with the SOI platform, take advantage of the optical power enhancement present in resonator structures at specific wavelengths in order to generate multiple comb lines through parametric frequency conversion. These Kerr combs have exhibited spans as large as an octave, while their line spacing is fixed at a value equal to the Free Spectral Range (FSR) of the resonator involved. The commonly reported values for the line spacings in these types of combs are in the range of hundreds of GHz, although devices involving very large ring resonators have even shown values below 100 GHz [89]. However, the main limitation of the Kerr comb generation technique is the requirement for a high optical pump power to trigger the nonlinear effect (in the order of Watts or hundreds of milliWatts), with no means of control over its distribution to the comb lines.

A different technique to generate a comb from a single-wavelength input is the use of E/O modulation by a Radio Frequency (RF) driving signal. In this case, the line spacing is solely determined by the modulating frequency of the RF signal, while the comb span is dependent on the achievable modulation depth that dictates the number of generated harmonics. The phase modulators that have previously been used to produce these higher-order tones that comprise the comb spectrum were based on integrated InP [102, 103] or $LiNbO_3$ [104–107]. As the main advantage of this technique is its flexibility in terms of the generated spectral shape, a number of efforts have also been directed towards producing flat combs, mainly by appropriately tailoring the electrical input [105, 106, 108–111]. The most important result of recent years on silicon E/O combs has been the use of a silicon-organic-hybrid (SOH) Mach–Zehnder Modulator (MZM) to generate the WDM carriers of a Tbit/s data transmitter [112], while other works (including the one reported in this chapter) [24, 113–116] have investigated the potential of conventional silicon RRMs for comb generation.

In this chapter, a comb generation technique based on the use of E/O ring modulators is investigated, while experimental results for the implementation on a fabricated silicon device are reported. The first section presents an analytical model describing intensity and phase modulation in ring resonator structures that contain an electrorefractive component, along with a calculation of the spectral components of the modulated output. The following section reports the experimental generation of a flat comb in the C-band, using a fabricated silicon RRM driven by two sinusoidal RF signals. This result provided the first investigation of frequency comb generation with a conventional silicon RRM in the literature [24].

4.1 Modelling Tone Modulation in Ring Resonators

To acquire a thorough understanding of the effects of RF tone modulation on the optical output spectrum of an E/O ring resonator structure, a theoretical approach was attempted as a first step. This section reports the development of an analytical model that describes electro-optical modulation in a ring resonator whose circumference comprises an electrorefractive element. The mathematical formulation for this model is based on the expressions for guided propagation modes and on control theory models, represented by block diagrams. It is noted that this model assumes a linear system for the ring resonator component, and only addresses its steady state behaviour. This means that optical nonlinearities as well as the dynamic behaviour of the ring are not considered in the approach described in this section. This does not diminish the value of the drawn conclusions in terms of applicability in real systems, as the operation of a RRM at low optical power and in the presence of relatively low-frequency RF driving signals is compatible with the presented theoretical treatment. In particular, a real RRM can be described by the model as long as the optical power is sufficiently low so that no nonlinear effects are triggered in the ring circumference where light experiences enhancement at resonance wavelengths. As for the RF input, this model is accurate for driving signals exhibiting transition periods larger than the photon cavity lifetime, which is dependent on the ring quality factor. Finally, it should be noted that the development of this model as an original idea of the author occurred in parallel with the work published in [117], which is the only report in the literature of a frequency-domain approach to the problem.

4.1.1 Block diagram representation of a Ring Resonator

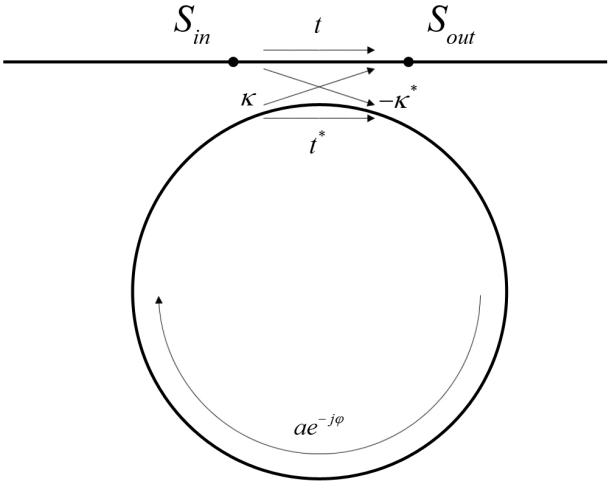

FIGURE 4.1: Schematic of a ring resonator structure with annotations of the input and output mode field variables as well as the mode propagation direction.

As described in Chapter 2, the structure of a ring resonator consists of a bus waveguide and a ring cavity, as illustrated in Fig. 4.1. The analytical expression describing its input-output field relation is repeated here for consistency:

$$S_{out} = \frac{t - \alpha e^{-j\phi}}{1 - \alpha t^* e^{-j\phi}} S_{in} \tag{4.1}$$

where $\phi = k_0 n_{eff} L$ is the phase accumulated during one round-trip propagation of the mode along the ring circumference. The variables k_0, n_{eff} and L here represent the free-space wavenumber, the effective refractive index of the mode and the ring circumference respectively. The design parameters t and α represent the through-transmission coefficient and the round-trip loss respectively. Since S_{out} and S_{in} are electric field variables, t and α also relate to the mode electric field rather than the mode intensity.

Since the function of the cavity structure can essentially be viewed as a feedback mechanism, it is useful to express the above equation using control theory nomenclature, representing the ring resonator system with a block diagram. This diagram is depicted in Fig. 4.2, where all the aforementioned variables are present and κ is the cross-coupling coefficient, directly linked to t through the relation $\kappa^2 + t^2 = 1$. The presence of the feedback loop in the ring resonator system is obvious in this representation and it is trivial to prove that the diagram mathematically corresponds to eq. (4.1).

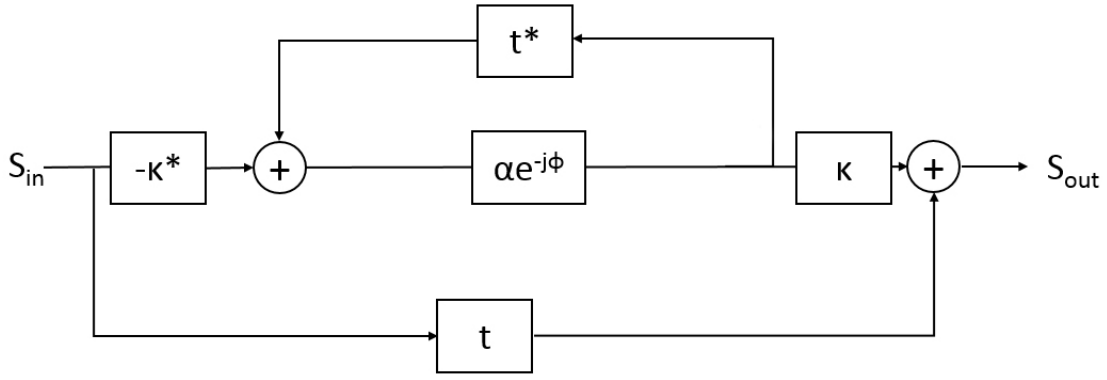

FIGURE 4.2: Block diagram representing a ring resonator system with the mode field as variable.

Eq. (4.1) evaluates the system output S_{out} for a given input S_{in} at a specific wavelength. Although it can describe the steady-state response of the system for any given wavelength, it only applies to systems where S_{in} and S_{out} are variables of electric field of the same wavelength. Therefore, it cannot model the functionality of a modulator, which produces new spectral components at the output, through the use of active elements. In the specific case of a silicon RRM whose circumference is carrier-doped in order to modify the effective refractive index through a voltage input, the electrorefractive element would be ideally represented by a phase modulator. In the presence of a given RF

electrical input, the phase modulator generates spectral sidebands at the output stage which, in principle, cannot be described by the scalar variable S_{out}. In the special case of sinusoidal modulation, the sidebands only consist of discrete frequency tones, at a spacing equal to the modulating frequency Ω_{RF}.

To address the need to handle multiple wavelengths simultaneously, the representation used in Fig. 4.2 was modified. In the new approach, instead of scalar variables, S_{in} and S_{out} are considered to be vectors, whose elements correspond to discrete positions in the frequency axis. Thus, this new system can treat input and output electric fields as they are distributed across a discrete spectrum. Since the model is developed to describe tone modulation and the output spectrum can only exhibit a discrete, comb-like form, the discretisation of the spectrum can be conveniently defined so that the spacing between adjacent frequency points is equal to the modulating frequency Ω_{RF}. The input and output vector variables are now written in the form:

$$\mathbf{S}_{in} = \begin{bmatrix} S_{-N,in} \\ \dots \\ S_{-1,in} \\ S_{0,in} \\ S_{1,in} \\ \dots \\ S_{N,in} \end{bmatrix}, \mathbf{S}_{out} = \begin{bmatrix} S_{-N,out} \\ \dots \\ S_{-1,out} \\ S_{0,out} \\ S_{1,out} \\ \dots \\ S_{N,out} \end{bmatrix} \tag{4.2}$$

where S_0 denotes the complex field amplitude at the centre frequency and $S_i, i \neq 0$ represent the amplitudes spanning the rest of the discrete spectrum. It is noted that the span of the spectrum, i.e. the vector size $(2N+1)$ can be arbitrarily selected and is limited by the used hardware in computational solving.

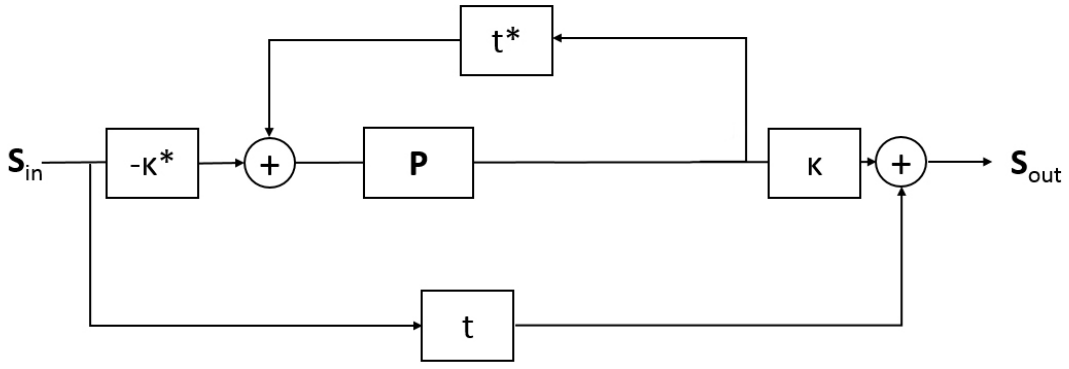

FIGURE 4.3: Block diagram representing a ring resonator system - Matrix approach.

Based on this modification, the new block diagram is mathematically described by matrix operations. Illustrated in Fig. 4.3, the blocks comprising the system can now represent

either scalar coefficients or $(2N+1) \times (2N+1)$ matrices. In particular, the blocks including κ and t retain their scalar form, whereas in order to account for the dispersion in the ring, the round-trip propagation block $\mathbf{P}$ is a matrix defined as:

$$\mathbf{P} = \alpha \begin{bmatrix} e^{-j\phi_{-N}} & ... & 0 & 0 & 0 & ... & 0 \\ ... & ... & ... & ... & ... & ... & ... \\ 0 & ... & e^{-j\phi_{-1}} & 0 & 0 & ... & 0 \\ 0 & ... & 0 & e^{-j\phi_0} & 0 & ... & 0 \\ 0 & ... & 0 & 0 & e^{-j\phi_1} & ... & 0 \\ ... & ... & ... & ... & ... & ... & ... \\ 0 & ... & 0 & 0 & 0 & ... & e^{-j\phi_N} \end{bmatrix} \tag{4.3}$$

which expresses the round-trip propagation in the ring for different wavelengths. The accumulated phase ϕ_i is different for each travelling wave of different wavelength and this is expressed by the different values in each element of the main diagonal. This representation still describes a ring resonator with no electrorefractive element. This is why the only matrices it contains are diagonal.

4.1.1.1 Ring Resonator Modulator Model – Single-tone Drive

Regarding the case of a RRM modulating a single-wavelength optical input, the corresponding block diagram is shown in Fig. 4.4, where S_{in} and S_{out} take the form:

$$\mathbf{S}_{in} = \begin{bmatrix} 0 \\ ... \\ 0 \\ S_{0,in} \\ 0 \\ ... \\ 0 \end{bmatrix}, \mathbf{S}_{out} = \begin{bmatrix} S_{-N,out} \\ ... \\ S_{-1,out} \\ S_{0,out} \\ S_{1,out} \\ ... \\ S_{N,out} \end{bmatrix} \tag{4.4}$$

The use of the matrix approach becomes clear in the RRM model, where the phase modulator component is represented by matrix $\mathbf{A}$. To construct this matrix, the formula for phase modulation by a sinusoidal signal was used, according to the Jacobi-Anger identity:

$$e^{j\omega_c t} e^{j\left(\Delta\phi_A sin\Omega_{RF} t\right)} = e^{j\omega_c t} \sum_{n=-\infty}^{\infty} J_n(\Delta\phi_A) e^{jn\Omega_{RF} t} \tag{4.5}$$

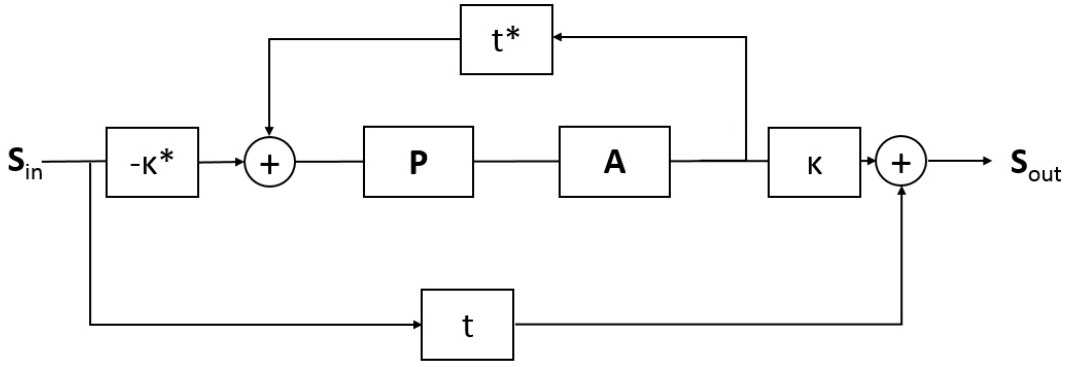

FIGURE 4.4: Block diagram representing a ring resonator system - Matrix approach.

where ω_c is the carrier frequency, $\Delta\phi_A$ is the phase amplitude of the modulating signal and Ω_{RF} the modulating frequency. Based on this expansion to the harmonics of the carrier frequency, the phase modulation matrix $\mathbf{A}$ is written as:

$$\mathbf{A} = \begin{bmatrix} J_0(\Delta\phi_{A,N}) & ... & J_{-N+1}(\Delta\phi_{A,1}) & J_{-N}(\Delta\phi_{A,0}) & J_{-N-1}(\Delta\phi_{A,-1}) & ... & J_{-2N}(\Delta\phi_{A,-N}) \\ ... & ... & ... & ... & ... & ... & ... \\ J_{N-1}(\Delta\phi_{A,N}) & ... & J_0(\Delta\phi_{A,1}) & J_{-1}(\Delta\phi_{A,0}) & J_{-2}(\Delta\phi_{A,-1}) & ... & J_{-1-N}(\Delta\phi_{A,-N}) \\ J_N(\Delta\phi_{A,N}) & ... & J_1(\Delta\phi_{A,1}) & J_0(\Delta\phi_{A,0}) & J_{-1}(\Delta\phi_{A,-1}) & ... & J_{-N}(\Delta\phi_{A,-N}) \\ J_{N+1}(\Delta\phi_{A,N}) & ... & J_2(\Delta\phi_{A,1}) & J_1(\Delta\phi_{A,0}) & J_0(\Delta\phi_{A,-1}) & ... & J_{1-N}(\Delta\phi_{A,-N}) \\ ... & ... & ... & ... & ... & ... & ... \\ J_{2N}(\Delta\phi_{A,N}) & ... & J_{N+1}(\Delta\phi_{A,1}) & J_N(\Delta\phi_{A,0)} & J_{N-1}(\Delta\phi_{A,-1}) & ... & J_0(\Delta\phi_{A,-N}) \end{bmatrix} \tag{4.6}$$

where $J_n(\Delta\phi_A)$ is the n-th Bessel function of the first kind and $\Delta\phi_A$ is given by the equation:

$$\Delta\phi_A = \frac{2\pi}{\lambda}\Delta n_{eff,A} L \tag{4.7}$$

and expresses the phase modulation amplitude, considered to have the same value for all wavelengths, because the change is negligible for a small number of closely spaced frequency taps around the centre frequency. As can be observed, the difference of the phase modulator block (matrix $\mathbf{A}$) from the propagation block (matrix $\mathbf{P}$) in their mathematical formulation is that matrix $\mathbf{A}$ is non-diagonal. This approach enables the emulation of an active element which produces new frequencies in the output spectrum, through matrix multiplication.

Another interpretation of this formulation comes from the identity:

$$\mathbf{A}\cdot\mathbf{V}=\begin{bmatrix}\mathbf{A}_1 & \mathbf{A}_2 & \dots & \mathbf{A}_{2N+1}\end{bmatrix}\cdot\begin{bmatrix}v_1\\ v_2\\ \dots\\ v_{2N+1}\end{bmatrix}=v_1\mathbf{A}_1+v_2\mathbf{A}_2+\dots+v_{2N+1}\mathbf{A}_{2N+1} \quad (4.8)$$

which equates the matrix multiplication of an input vector $\mathbf{V}$ by the matrix $\mathbf{A}$ with a linear combination of the column vectors $\mathbf{A}_i$ (see (4.6)) with the elements v_i as coefficients. Each term $v_i\mathbf{A}_i$ in the right-hand side of eq. (4.8) expresses the phase modulation of each input frequency component v_i, as per eq. (4.5).

A mathematical expression can now be derived for the block diagram of Fig. 4.4, based on control theory:

$$\mathbf{S}_{out}=\left(|t|^2-1\right)\mathbf{AP}\left[\mathbf{I}-t^*\mathbf{AP}\right]^{-1}\mathbf{S}_{in}+t\mathbf{S}_{in} \quad (4.9)$$

where $\mathbf{I}$ represents the $(2N+1)\times(2N+1)$ unit matrix. The similarity of this matrix expression to the expression in eq. (4.1) is clear if the numerator and the denominator of the fraction in the latter are multiplied by t and written in the form:

$$\begin{aligned}S_{out}&=\frac{t-\alpha e^{-j\phi}}{1-\alpha t^* e^{-j\phi}}S_{in}\\ &=\frac{t-\alpha e^{-j\phi}}{t-\alpha|t|^2e^{-j\phi}}tS_{in}=\frac{t-\alpha e^{-j\phi}-\alpha|t|^2e^{-j\phi}+\alpha|t|^2e^{-j\phi}}{t-\alpha|t|^2e^{-j\phi}}tS_{in}\\ &=(1+\frac{(|t|^2-1)\alpha e^{-j\phi}}{t-\alpha|t|^2e^{-j\phi}})tS_{in}=\frac{(|t|^2-1)\alpha e^{-j\phi}}{1-\alpha t^*e^{-j\phi}}S_{in}+tS_{in}\end{aligned} \quad (4.10)$$

In order to demonstrate the functionality of this model in emulating the output spectrum of a RRM, a MATLAB routine was written to simulate it through the use of matrix variables. A set of parameters were fed to the routine, relating to the ring resonator structure and the driving signals, which are listed in Table 4.1. The parameter values were selected to resemble the fabricated RRM devices that were available in the laboratory. The transfer function of the overcoupled ring resonator is shown in Fig. 4.5 (a) and the output spectrum after modulation is shown in Fig. 4.5 (b).

For the considered overcoupled ring resonator, the driving signal amplitude corresponds to the maximum available n_{eff} change that the RF signals can produce in the laboratory. It is clear that the modulation depth is large enough to suppress the carrier to a power level lower than the first harmonics. However, it is not strong enough to increase the power of the second harmonics to a level that allows them to form part of the comb.

TABLE 4.1: **MATLAB Model Parameters**

Property	**Value**
Optical Input Power	1 a.u.
Optical Input Wavelength	1547.858 nm (Resonance Wavelength)
Ring round-trip loss α	0.9828
Field through-transmission coefficient t	0.9548
Ring diameter L	24 μm
Effective group index	3.88
Modulating frequency Ω_{RF}	10 GHz
Effective refractive index change Δn_{eff}	2.15×10^{-4}
A Matrix size $M \times M$	121×121

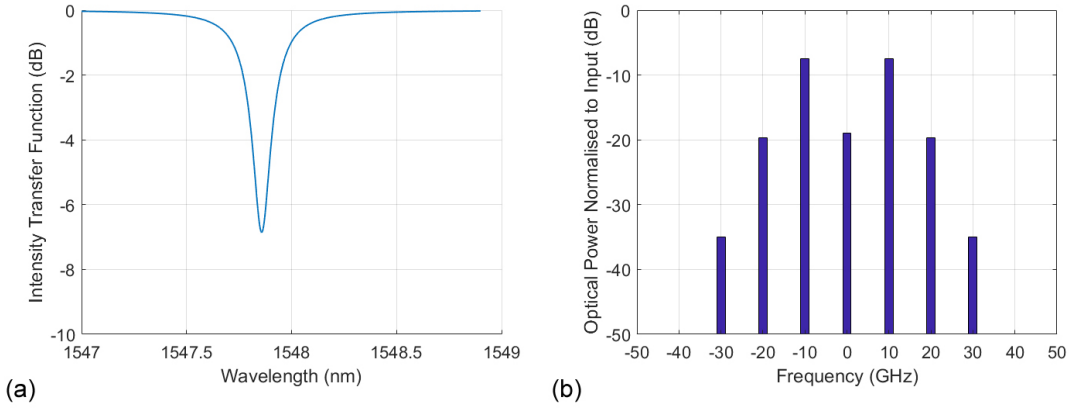

FIGURE 4.5: (a) Modelled ring resonator intensity transfer function, (b) Calculated output spectrum under 10-GHz tone modulation.

Enhancing the power of the second harmonics would result in two prominent tones on each side of the optical carrier, forming a comb shape with five lines.

4.1.1.2 Ring Resonator Modulator Model – Dual-tone Drive

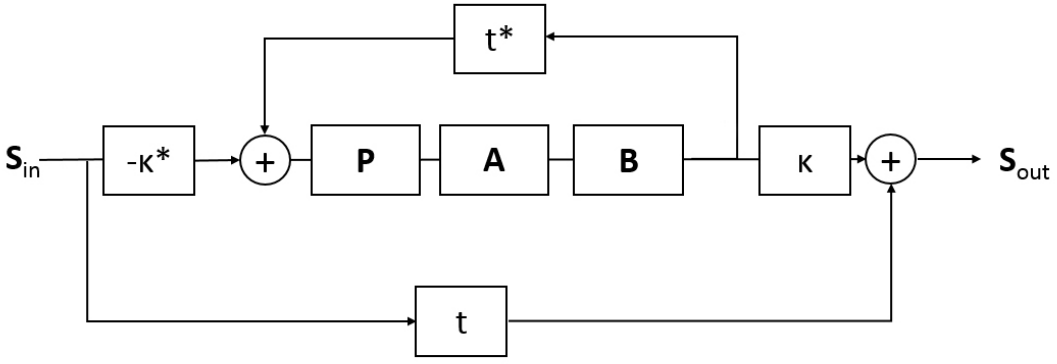

FIGURE 4.6: Block diagram representing a ring resonator modulator system electrically driven using the dual sine wave technique.

Since this model was developed to investigate the potential of a RRM for frequency comb generation, configurations with appropriately tailored driving signals were considered in order to expand the comb span. A well-known technique in the literature is the operation under a multiple-tone electrical input. In the specific case of a dual sine wave input to the RRM at frequencies of Ω_{RF} and $2\Omega_{RF}$, the optical wave is described by the expression $e^{j\omega_c t} e^{j\left(\Delta\phi_A sin(\Omega_{RF} t + \Delta\theta)\right)} e^{j\left(\Delta\phi_B sin(2\Omega_{RF} t)\right)}$, where $\Delta\theta$ is used here to denote the phase difference between the two sine waves. The phase amplitudes of the two modulating tones are represented in this expression by $\Delta\phi_A$ and $\Delta\phi_B$. The model used to describe this configuration is illustrated in Fig. 4.6.

In this model, the matrices **A** and **B** are given by the expressions:

$$
\mathrm{A} = \begin{bmatrix}
J_0(\Delta\phi_{A,N}) & \cdots & e^{j(-N+1)\Delta\theta} J_{-N+1}(\Delta\phi_{A,1}) & e^{-jN\Delta\theta} J_{-N}(\Delta\phi_{A,0}) & e^{j(-N-1)\Delta\theta} J_{-N-1}(\Delta\phi_{A,-1}) & \cdots & e^{j(-2N)\Delta\theta} J_{-2N}(\Delta\phi_{A,-N}) \\
\cdots & \cdots & \cdots & \cdots & \cdots & \cdots & \cdots \\
e^{j(N-1)\Delta\theta} J_{N-1}(\Delta\phi_{A,N}) & \cdots & J_0(\Delta\phi_{A,1}) & e^{-j\Delta\theta} J_{-1}(\Delta\phi_{A,0}) & e^{-2j\Delta\theta} J_{-2}(\Delta\phi_{A,-1}) & \cdots & e^{j(-1-N)\Delta\theta} J_{-1-N}(\Delta\phi_{A,-N}) \\
e^{jN\Delta\theta} J_N(\Delta\phi_{A,N}) & \cdots & e^{j\Delta\theta} J_1(\Delta\phi_{A,1}) & J_0(\Delta\phi_{A,0}) & e^{-j\Delta\theta} J_{-1}(\Delta\phi_{A,-1}) & \cdots & e^{-jN\Delta\theta} J_{-N}(\Delta\phi_{A,-N}) \\
e^{j(N+1)\Delta\theta} J_{N+1}(\Delta\phi_{A,N}) & \cdots & e^{j2\Delta\theta} J_2(\Delta\phi_{A,1}) & e^{j\Delta\theta} J_1(\Delta\phi_{A,0}) & J_0(\Delta\phi_{A,-1}) & \cdots & e^{j(1-N)\Delta\theta} J_{1-N}(\Delta\phi_{A,-N}) \\
\cdots & \cdots & \cdots & \cdots & \cdots & \cdots & \cdots \\
e^{j2N\Delta\theta} J_{2N}(\Delta\phi_{A,N}) & \cdots & e^{j(N+1)\Delta\theta} J_{N+1}(\Delta\phi_{A,1}) & e^{jN\Delta\theta} J_N(\Delta\phi_{A,0}) & e^{j(N-1)\Delta\theta} J_{N-1}(\Delta\phi_{A,-1}) & \cdots & J_0(\Delta\phi_{A,-N})
\end{bmatrix} \tag{4.11}
$$

$$\mathrm{B} = \begin{bmatrix} \dots & \dots & \dots & \dots & \dots & \dots & \dots \\ \dots & J_0(\Delta\phi_{B,2}) & 0 & J_{-1}(\Delta\phi_{B,0}) & 0 & J_{-2}(\Delta\phi_{B,-2}) & \dots \\ \dots & 0 & J_0(\Delta\phi_{B,1}) & 0 & J_{-1}(\Delta\phi_{B,-1}) & 0 & \dots \\ \dots & J_1(\Delta\phi_{B,2}) & 0 & J_0(\Delta\phi_{B,0}) & 0 & J_{-1}(\Delta\phi_{B,-2}) & \dots \\ \dots & 0 & J_1(\Delta\phi_{B,1}) & 0 & J_0(\Delta\phi_{B,-1}) & 0 & \dots \\ \dots & J_2(\Delta\phi_{B,2}) & 0 & J_1(\Delta\phi_{B,0}) & 0 & J_0(\Delta\phi_{B,-2}) & \dots \\ \dots & \dots & \dots & \dots & \dots & \dots & \dots \end{bmatrix} \tag{4.12}$$

The expression for matrix **A** is slightly different to incorporate the phase difference $\Delta\theta$, while matrix **B** is similar to **A**, consisting of Bessel function elements, only more sparsely distributed as modulation from a $2\Omega_{RF}$ signal only generates harmonics of order equal to $2n\Omega_{RF}$. The mathematical formulation for the model in Fig. 4.6 is given by the expression:

$$\mathbf{S}_{out} = \Big(|t|^2 - 1\Big)\mathbf{BAP}\Big[\mathbf{I} - t^*\mathbf{BAP}\Big]^{-1}\mathbf{S}_{in} + t\mathbf{S}_{in} \tag{4.13}$$

A MATLAB routine was written to emulate this second model, where the electrical input was now set to a dual sine wave signal, consisting of a 10-GHz and a 20-GHz tone. The Δn_{eff} amplitudes were set to 0.72×10^{-4} and 1.39×10^{-4} respectively, so that they correspond to signals that can be produced in the laboratory. In this case, the output spectrum is also affected by the phase difference $\Delta\theta$ between the two tones, which is already incorporated into the model, therefore this parameter was swept in order to produce the flattest possible comb. The best result (for $\Delta\theta = 0.75$ rad) is shown in Fig. 4.7 (a), while a flatness metric is plotted with respect to the phase difference $\Delta\theta$ between the two tones in Fig. 4.7 (b). Flatness is defined as the power difference between the strongest and the weakest comb line among the five.

It is clear that this comb does not exhibit sufficient flatness, as the maximum power difference among its five lines is equal to 6.38 dB. In order to explore alternative methods of flattening the comb shape, other parameters of the system that can affect the output spectrum were investigated. In particular, the impact of the ring coupling condition was studied by monitoring the generated lines as the through transmission coefficient t was varied. The results shown in Fig. 4.8 (a) present the trend in carrier power as well as the harmonic powers for the overcoupling ($t < \alpha$) and the undercoupling regime ($t > \alpha$). There are two cases where the two power levels are equalised, producing a relatively flat 5-line comb: one appears inside the overcoupling regime and the other inside the undercoupling regime, both of which occur near the critical coupling point.

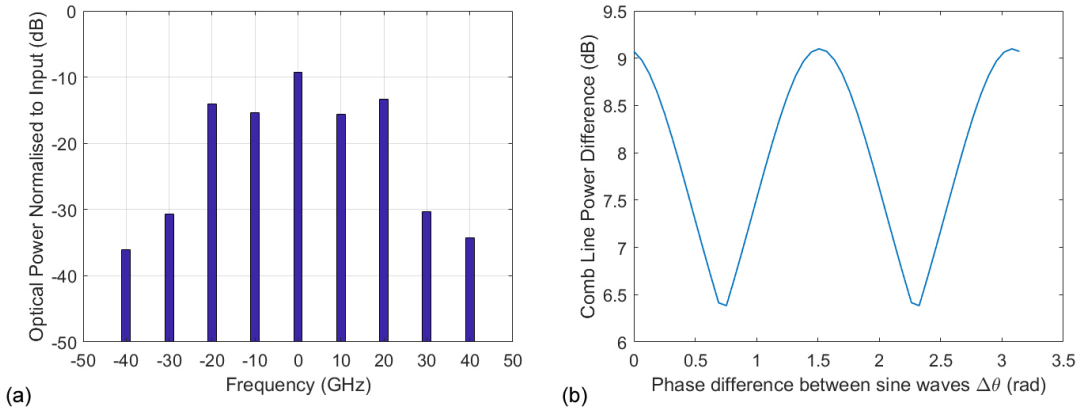

FIGURE 4.7: (a) Calculated output spectrum under 10- and 20-GHz tone modulation, (b) Comb flatness variation with respect to the phase difference $\Delta\theta$ between the two tones.

The flat comb result is a combination of the carrier suppression caused by a strong modulation effect and the level of enhancement that the harmonics experience. Under this consideration, the trend in the power level of the produced harmonic tones is important (Fig. 4.8 (a)), which is dependent on how many round-trips they complete when they enter the ring cavity. Therefore, inside the overcoupling regime, the structure favours the propagation of the generated optical tones inside the cavity and the cascaded phase modulation phenomenon is more prominent, whereas in the undercoupling regime the harmonic power levels drop significantly.

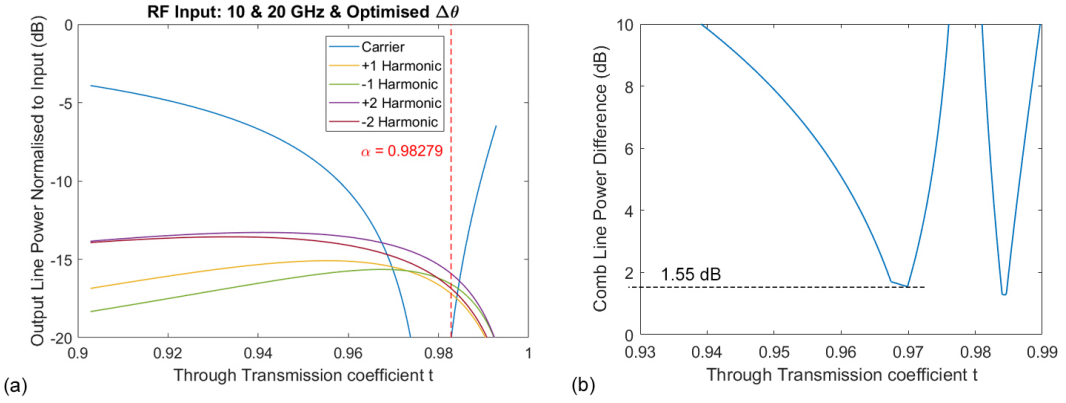

FIGURE 4.8: (a) Calculated power levels for carrier and harmonic tones vs. through transmission coefficient t under 10- and 20-GHz tone modulation with the optimum $\Delta\theta$ value, (b) Comb flatness variation with respect to the through transmission coefficient t.

Figure 4.8 (b) shows the line power difference as it varies with respect to the through transmission coefficient t. The two areas of minimum power difference (increased flatness) can be observed, with the overcoupling regime corresponding to a more robust comb generator system with respect to variations in t. These minima correspond to much lower values than the ones shown in Fig. 4.7 (b), reaching $<$ 2-dB levels.

Therefore, the MATLAB routine was run for the optimised value of 0.9699 for the t parameter (minimum power difference inside the overcoupling regime), which showed a power difference of 1.55 dB among the comb lines. The resulting spectrum is shown in Fig. 4.9 (a), with its dependence on the phase difference $\Delta\theta$ depicted in Fig. 4.9 (b).

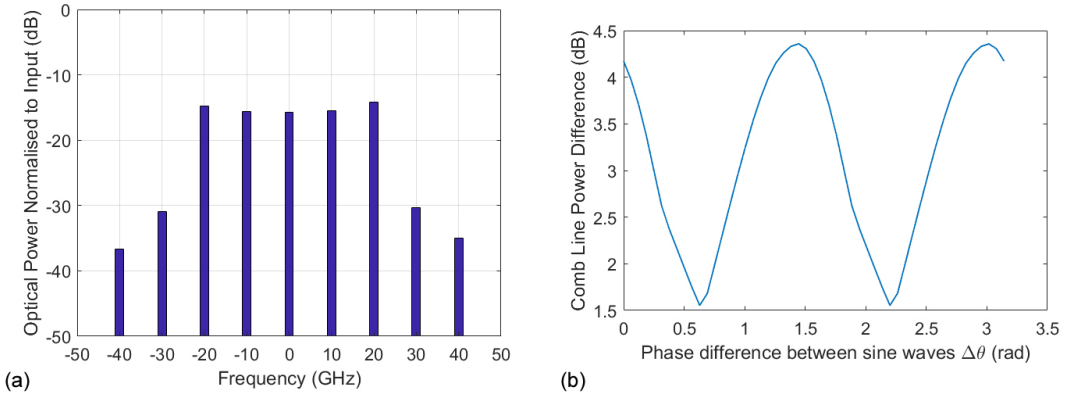

FIGURE 4.9: (a) Calculated output spectrum under 10- and 20-GHz tone modulation for $t = 0.9699$, (b) Comb flatness variation with respect to the phase difference $\Delta\theta$ between the two tones.

The investigation of the model parameters that affect the comb shape were a useful guide in order to implement the comb generation technique with a fabricated device in the laboratory. The tuning methods presented in this section were considered in the experimental procedure described in the following section to optimise the comb shape in terms of flatness. The amplitude and phase of the RF signals could easily be tuned with the available electrical components, while traversing different regimes of the ring coupling condition was achieved by appropriately biasing the p-n junction of the silicon modulator, which triggered different modulation mechanisms and at the same time affected the round-trip loss.

4.2 Frequency comb generation in a Ring Resonator Modulator

This section reports the generation of an optical frequency comb with a highly uniform power distribution along its span, through the use of a micrometer-scale Ring Resonator Modulator (RRM) fabricated on a SOI platform. The device was designed by Dr. D. J. Thomson at the Optoelectronics Research Centre (ORC) and fabricated at the Institute of Microelectronics (IME) in Singapore for the Silicon Photonics for Future Systems (SPFS) project. The characterisation and comb generation experiments were performed by the author, with the help of Dr. C. Lacava and Dr. K. R.H. Bottrill. The specifications of the RRM are first presented, along with the measurements of its complex transfer function. Next, the comb generation experiment is described and the effect of

the coupling condition and modulation regime on the comb shape is discussed. Finally, the optimum operation of the RRM for the generation of a flat comb is reported, with the demonstration of five 10-GHz-spaced lines, whose coherence is verified by an additional time-domain measurement showing transform-limited pulse generation. These results were the first investigation of the capabilities of conventional small-footprint and low-power silicon modulators for comb generation on an integrated platform. The significance of these observations can be appreciated in potential WDM systems requiring low-cost solutions for comb generation, with devices fabricated using CMOS-compatible processes.

4.2.1 Ring Resonator Design

A modulator-based comb is produced by means of electro-optic modulation of a Continuous Wave (CW) source. This is essentially achieved by appropriately shaping the resulting spectrum around the optical carrier. In particular, the comb shape is determined mainly by two factors: the applied electrical signal waveform and the achieved modulation depth. In the specific case of a silicon RRM, the modulation depth is dependent on the coupling condition of the ring and the operating regime of the p-n junction. Since these are directly related to the RRM design, the specifications of the fabricated device are described in the following paragraphs, with an elaborate discussion on the above parameters of this implementation.

The fabricated RRM reported in this chapter had a 24-μm diameter and a bus-ring gap of 240 nm, which was measured to be slightly off the critical coupling point, inside the overcoupling regime (see Section 2.1.5.2), when no bias voltage is applied. The device was fabricated on a SOI wafer, entirely through CMOS-compatible processes. A top view microscope image of the RRM is shown in Fig. 4.10 (a), while the cross-section of its doped waveguide section is portrayed in Fig. 4.10 (b), where the p-n junction can be seen (not visible in the top view image). The silicon layer thickness was 220 nm and the etching depth for the rib waveguide structures was 130 nm. The photonic circuit pattern was written using Deep Ultraviolet (DUV) lithography, while the p- and n-doped sections were realised by boron and phosphorus ion implantation respectively along the ring circumference. Coupling to and from the planar structures on the silicon chip was facilitated by two focused grating couplers, which were designed for Transverse Electric (TE) mode operation in the C-band (electric field parallel to the x-axis in Fig. 4.10). Two Polarisation Maintaining (PM) fibres were positioned at a 11°-angle to the surface normal of the chip to launch and collect light, as shown in Fig. 4.10 (c).

Regarding the electrical input to the RRM, the three metallic pads shown in Fig. 4.10 (a) were written on a layer on top of the photonic structure in a Ground-Signal-Ground (GSG) configuration to provide access to the p- and n-doped sections of the ring circumference through vias. Thus, the RF signal could be applied to the RRM through

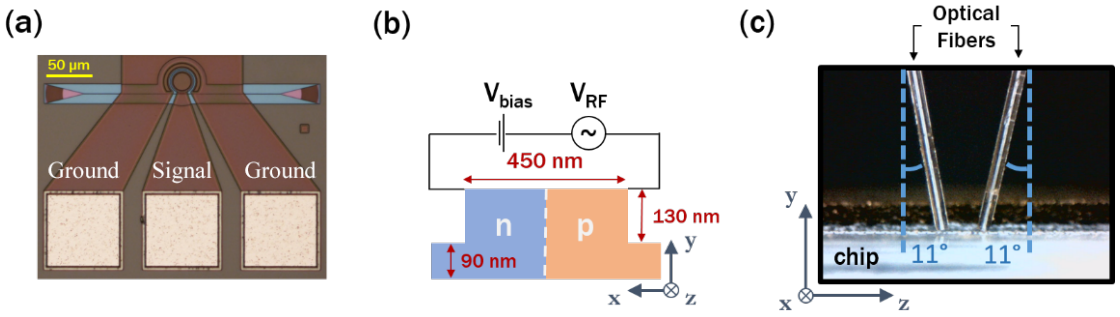

FIGURE 4.10: (a) Ring resonator modulator top view micrograph, (b) waveguide cross section and (c) coupling scheme for the silicon photonic chip.

a high-speed 3-pin GSG probe that made contact with the pads. The changes caused to the propagating optical mode by the voltage applied to the p-n junction can be attributed to both electrorefractive and electroabsorptive effects, as per the relation of carrier density change with respect to refractive index and absorption in silicon, evaluated by Soref and Bennett in [35]. In a doped waveguide, these effects are expressed as a change in its complex effective refractive index $\Delta\tilde{n}_{eff}$, which is defined as:

$$\Delta\tilde{n}_{eff} = \Delta n_{eff} + i\Delta\alpha \tag{4.14}$$

where Δn_{eff} expresses the effective refractive index change of the doped waveguide and $\Delta\alpha$ expresses the absorption change. In the case of the RRM, where the doped section was the ring circumference, the two effects manifested themselves as changes in the transfer function of the RRM: Δn_{eff} was exhibited as a wavelength shift, while $\Delta\alpha$ altered the resonance depth and shape because an increase in the round-trip loss altered the coupling condition. Depending on the polarity of the applied voltage, the physical mechanisms responsible for the change in $\Delta\tilde{n}_{eff}$ were either the change in the depletion area of the junction (in the reverse bias regime) or the injection of free carriers (in the forward bias regime), both present in an area that overlaps with the optical mode. The impact of the junction regime on the RRM transfer function was evaluated by characterisation measurements reported in the following paragraphs.

4.2.2 Device Characterisation

First, the intensity transfer function of the RRM was measured, using a tunable laser source while simultaneously monitoring the output power of the modulator. The transmission spectrum is therefore shown in Fig. 4.11 (a) for different bias voltages, measured by means of a wavelength sweep of a 1-pm step. The effect of the bias regime on the resonance shape and position in the λ-axis is apparent. The deepest resonance trough is observed for a forward bias voltage of 1 V, which suggests that the ring is critically

coupled for this voltage, while lower (including reverse bias) and higher voltages correspond to overcoupled and undercoupled ring states respectively. By evaluating the quality factors (Q-factors) of the ring for each voltage, it is useful to note that they fall in the range of 3,000 to 10,000, corresponding to photon cavity lifetimes smaller than 8 ps. This suggests that there is no significant bandwidth limitation originating from the resonator topology itself for electrical signal frequencies in the order of tens of GHz.

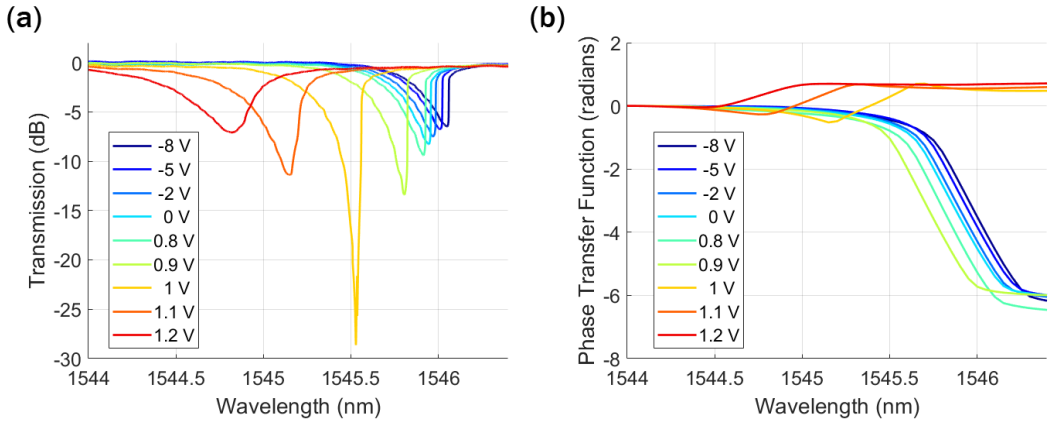

FIGURE 4.11: Measured (a) intensity and (b) phase transfer function (resolution: 50 pm) of the ring resonator modulator and their change vs. applied bias voltage.

Apart from the coupling condition investigation, it can also be seen that forward biasing induces stronger changes to the RRM response, which is due to the different characteristics of the physical mechanisms responsible for modulation in forward and reverse bias. In the reverse bias case, the depletion region of the p-n junction is widened compared to the case of no applied voltage and the induced changes to it do not overlap highly with the optical mode, hence they cause a small but fast effective refractive index change. However, forward biasing involves a narrower depletion region, while for even higher voltages ($> +\ 0.7$ V), a carrier injection effect is triggered. Both of these mechanisms modify the effective refractive index greatly in forward bias, although carrier injection is a slower phenomenon. Therefore, even though the forward bias regime offers stronger interaction with the mode and leads the RRM to critical coupling, operation in the carrier injection regime hinders modulation at frequencies higher than $\sim$1 GHz. These effects of the different bias regimes also became clear by observation of the corresponding generated comb shapes which are discussed in the next section.

The phase transfer function of the RRM was also measured for different DC bias voltages and is plotted in Fig. 4.11 (b). As the phase profile of the RRM could not be directly measured, a purpose-built measurement system was constructed to extract this graph [118]. The technique that was used involved launching two closely spaced coherent spectral tones to the RRM and measuring the acquired phase difference between them after propagation in the device, through heterodyne detection at the output. The analytical description of this measurement method, along with the specifications of the implemented system used in the experiment are reported in [118–120]. The phase profile

plots in Fig. 4.11 (b) verify the change in the ring coupling state for different bias voltages. Based on the information from the graph, operating the RRM near the resonance wavelengths provides the largest phase modulation depth. For the purpose of comb generation, the phase modulation properties of the RRM provide useful insight regarding the capability of carrier suppression, which is key to achieving a flat comb shape. Carrier suppression can happen when the driving signal modifies the phase of the fundamental tone so that it reverses its sign throughout the voltage swing. Therefore, depending on the spectral position of the carrier tone relative to the RRM resonance wavelength, it can experience different levels of power suppression. This offers a degree of freedom in tuning the fundamental tone power level at the output in order to equalise it to the level of its harmonics and produce a flat comb shape.

4.2.3 Experimental results and Discussion

The setup illustrated in Fig. 4.12 was used to implement the frequency comb generation. An external tunable laser source generated the optical carrier that was fed to the RRM, while the electrical driving signal consisted of two RF sinusoidal waveforms. Two RF clocks were used to produce electrical tones at frequencies of 10 and 20 GHz, which were subsequently amplified and combined together to drive the RRM by means of a high-speed probe. A phase shifter was used to tune the phase difference between the two sinusoidal signals, while a bias tee enabled the application of a DC voltage to appropriately bias the p-n junction. The frequencies of 10 and 20 GHz were selected in order to produce five comb lines of a 10-GHz spacing. Higher modulating frequencies were also tested but the produced optical tones did not exhibit sufficient power levels to form a flat comb shape, due to the bandwidth limitations of the RRM.

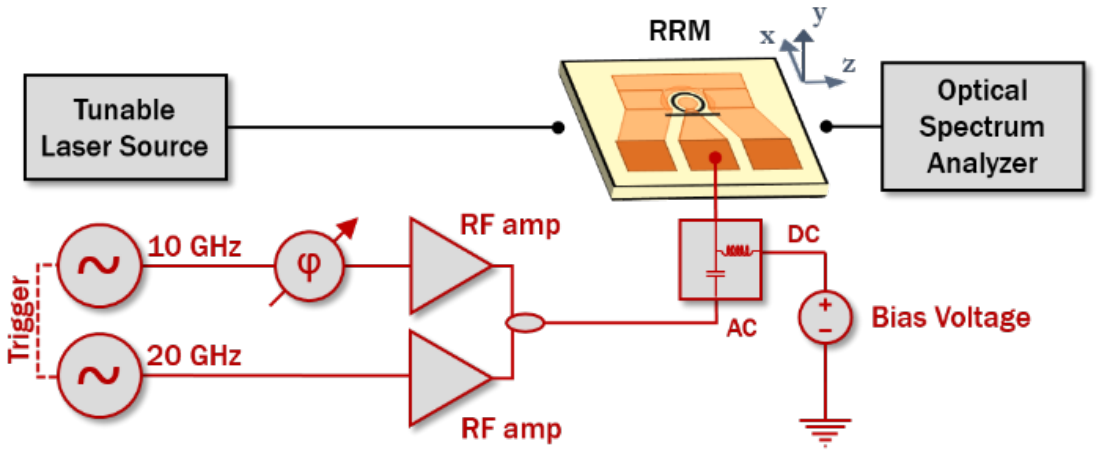

FIGURE 4.12: Experimental setup for the frequency comb generation. Lines in black represent optical connections, while lines in red represent electrical connections.

The implementation of this comb generation system offered sufficient flexibility in optimising the spectral output of the RRM. The system was appropriately tuned with the

aim of producing a comb with a flat shape and a high power level. Based on these considerations, the optical power used at the input was set to 2.3 dBm in order to produce comb lines at a high power level relative to the noise floor. Testing the system with higher intensity levels of the laser source triggered the onset of nonlinear effects in the ring which deteriorated the achievable modulation depth, because of the extra nonlinear effective refractive index change and nonlinear absorption present along the ring circumference. The optimum result was achieved with a 1.5-V_{pp} 10-GHz tone and a 2.9-V_{pp} 20-GHz tone, whose phase difference was equal to π radians, while the bias voltage used was equal to + 0.22 V. It is noted that the amplitudes of the RF tones were limited by the gain of the RF amplifiers used. This configuration generated the frequency comb illustrated in Fig. 4.13 (a), which consists of five 10-GHz-spaced spectral lines with a maximum power difference of 0.7 dB among them. The on-chip insertion loss of the RRM was equal to 5.5 dB.

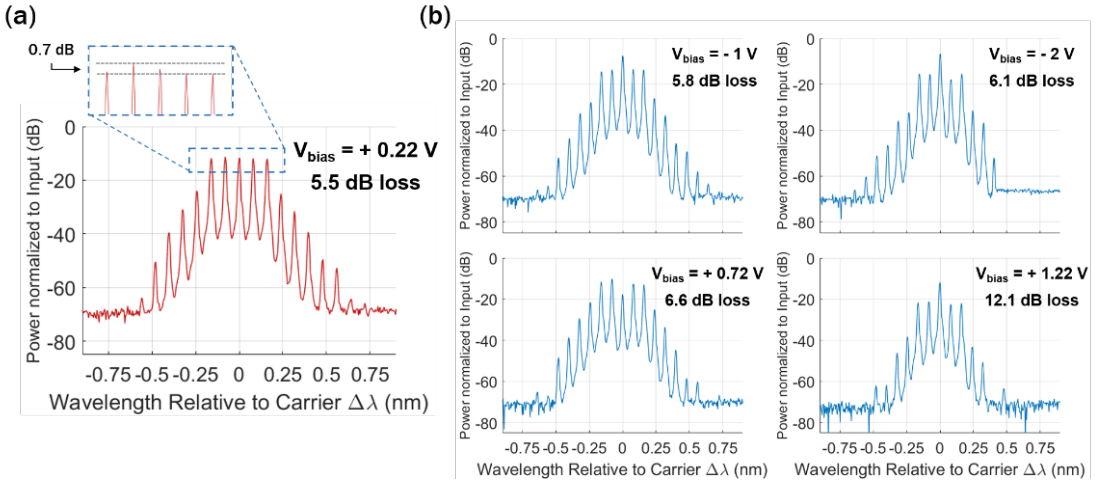

FIGURE 4.13: (a) Generated frequency comb at 10 GHz line spacing for a 0.22 Volt forward bias voltage applied, (b) Generated frequency combs for different bias voltages applied. Top and bottom rows correspond to reverse and forward bias respectively.

According to the discussion in the Device Characterisation section, the shape of the RRM output spectrum is determined by the strength of the combined amplitude and phase modulation effects. The power level of the produced harmonic tones is directly dependent on both of these effects, while the suppression of the carrier tone power is mainly determined by how strongly the light experiences phase modulation. The method used in this experiment to flatten the comb shape involved tuning the bias voltage of the RRM and the wavelength of the Continuous Wave (CW) source. Figure 4.13 (b) portrays the comb spectra corresponding to the different bias voltage regimes, for each of which the source wavelength was optimised for the best possible outcome in terms of comb flatness. In the case of reverse bias, the produced harmonics were not sufficiently strong to form a flat comb shape because the achieved modulation depth was relatively small. This is due to the relatively low resonance depth (see Fig. 4.12 (a)) and the moderate efficiency of the carrier-depletion effect. On the other hand, forward-biasing the RRM

led to higher modulation depths, because the ring was closer to the critical coupling state and the efficiency started to increase. However, higher forward bias voltages also moved the p-n junction towards the carrier injection regime, which hinders the generation of high-frequency harmonics. Hence, for bias voltages higher than ∼0.7 V, the power of the comb lines dropped significantly. Therefore, the optimum trade-off point was achieved for a bias voltage of + 0.22 V, which is illustrated in Fig. 4.13 (a). This observed trend in the evolution of the comb shape with varying bias voltage aligns with the predictions mentioned in the Device Characterisation section.

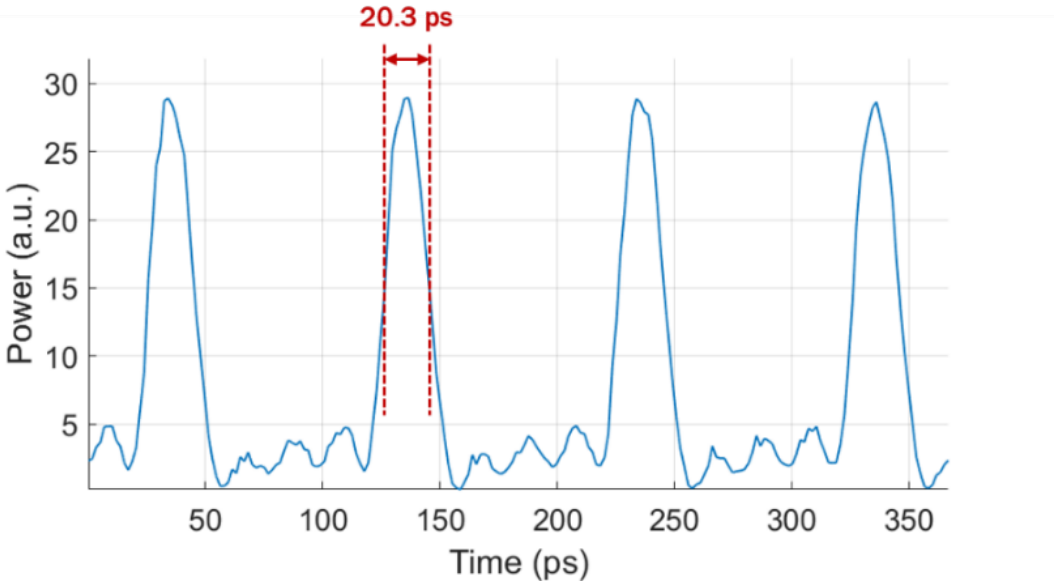

FIGURE 4.14: Measured optical pulses generated at the output of the device, by means of an optical sampling oscilloscope.

The next step was to verify the coherence of the generated comb lines through a time-domain measurement of the output. An optical sampling oscilloscope (EXFO PSO-102) was used to record the generated pulses illustrated in Fig. 4.14, that corresponded to the comb spectrum. The full-width at half-maximum (FWHM) of the pulses was measured to be 20.3 ps, while their repetition rate of 10 GHz matched the comb spacing. According to the analysis described in [106] regarding coherent flat frequency combs with near-ideal rectangular spectra, their corresponding time-domain representation is a sum of sinc-shaped Nyquist pulses. Based on this mathematical description, the theoretical pulse width, measured as the FWHM, is equal to $0.9\frac{1}{N \cdot f_m}$ when the phase is constant across all comb lines or shows a linear dependence on frequency across the comb spectrum [121, 122], where N is the number of the flat comb lines and f_m is the repetition rate. For the generated five-line comb spectrum reported in this chapter (Fig. 4.13 (a)), this corresponds to $0.9\frac{1}{5 \cdot 10\,GHz} = 18$ ps, which is close to the experimentally measured value of 20.3 ps. The small difference of ∼2.3 ps can be attributed to the fact that the generated comb spectrum was not ideally rectangular, since there is a 0.7 dB power margin among the lines. An alternative metric of the pulse width is the duration between the zero-crossing points which is theoretically equal to $\frac{2}{N \cdot f_m} = 40$ ps [106], while the

experimentally measured value was 41 ps, which verified that the generated pulses were transform-limited and the comb was coherent.

The comb generation technique that was implemented in this experiment exhibits a low cost in device footprint and low power consumption. Based on a compact ring resonator structure, the reported device occupies an area of 0.062 mm^2, which is much smaller compared to typical MZM-based devices, such as the mm-sized modulator presented in [112]. The RRM implementation relies on electronic control (two input RF tones) to fine-tune the generated comb shape, with a power consumption in the range of tens of milliWatts. Thus, the added complexity in the RF domain allows for the use of a simple conventional low-cost silicon modulator. The use of the five generated lines as optical carriers in transceiver devices can be compatible with commercial applications as previously reported solutions have commonly used four WDM carriers in their transmitter designs [19, 123, 124]. The limitations present in the reported experiment were related to the RRM E/O bandwidth which did not allow for a comb line spacing higher than 10 GHz and the strength of the external RF signal which restricted the number of generated lines. Regarding these aspects, the required power can be reduced and the comb span broadened for optimised ring designs, where the critical coupling condition is satisfied when the p-n junction is far from the carrier injection regime, as well as through cascaded ring configurations.

4.3 Conclusion

This chapter investigated the use of E/O silicon ring resonator modulators to generate an optical frequency comb. After an introduction to the concept of modulator-based comb generation techniques, the first section presented an analytical model for a tone-driven RRM and results of its MATLAB implementation for a dual-tone input were presented. The system behaviour was studied with respect to parameters such as the ring coupling condition and the phase difference between the two tones, which were tuned in order to optimise the comb shape in terms of flatness.

Based on the guidelines provided by this software model of the RRM, the next section described the experimental implementation of the comb generation technique on a fabricated silicon RRM. Characterisation measurements were reported and the effect of the bias voltage on the output comb shape was discussed. The best result involved the generation of five comb lines at a spacing of 10 GHz with a maximum power difference of 0.7 dB among them. The coherence of the lines was also verified by a time-domain measurement of the output, which revealed the generation of transform-limited 20-ps pulses. This work investigated for the first time the potential of a low-cost conventional micrometer-sized silicon modulator to generate a frequency comb in the C-band, based on an appropriately tailored RF input at low power.

Chapter 5

Mach–Zehnder Modulators for Advanced Modulation Formats

The capacity of an optical link served by a silicon modulator can be increased through the use of advanced modulation formats [125]. Depending on the specific link requirements, an appropriate combination of a modulation format and transceiver components is selected, with the purpose of maximising the available capacity while minimising the cost. In the case of short-to-medium-reach interconnects within data centres, where silicon modulators are used [15, 126, 127], the requirement for low complexity and cost-effectiveness has so far favoured the use of modulation formats compatible with Direct Detection (DD) schemes. For this reason, while modulation schemes such as Phase Shift Keying (PSK), Quadrature Amplitude Modulation (QAM) and Orthogonal Frequency-Division Multiplexing (OFDM) are widely employed in optical telecommunications, the primary focus in the case of silicon photonic transceivers has been on formats such as Pulse Amplitude Modulation (PAM) and the OFDM implementation termed Discrete MultiTone (DMT), that can be directly received by a photodetector, without the need for any coherent system.

PAM formats that use 4 amplitude levels or more can essentially allocate multiple information bits to each transmitted symbol, while techniques such as DMT modulation load the information bits on multiple carrier frequencies which simultaneously modulate the optical carrier. However, these formats have strict requirements in terms of transmission reliability, because their corresponding waveforms exhibit amplitude variations that must be more precisely replicated at the receiver side, compared to a conventional On-Off Keying (OOK) signal ((Fig. 5.1)). This poses some challenges on the modulator design, which has to show highly linear behaviour in order to transfer the signal to the optical domain undistorted.

This chapter reports the implementation of a fabricated and electrically-packaged silicon Mach–Zehnder modulator for the purpose of PAM-4 and DMT data transmission

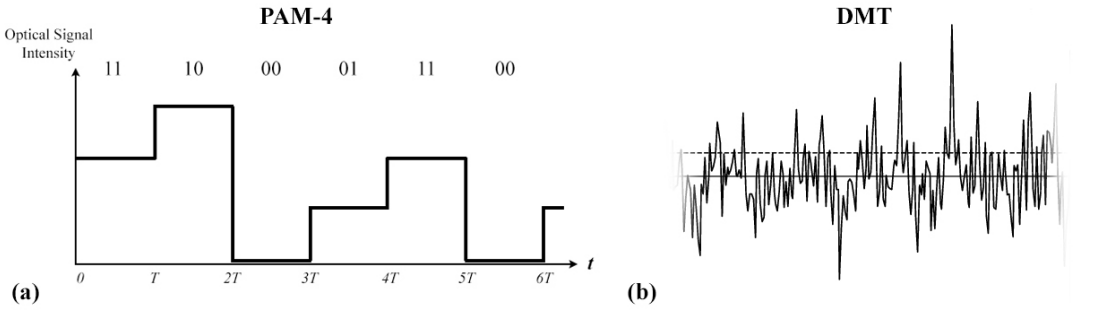

FIGURE 5.1: Time-domain representation of data modulated with (a) the PAM-4 format and (b) the DMT format.

and further considers through modelling several Ring-Assisted MZI modulator design configurations optimised for linearity and modulation depth. The first section presents the characterisation results on the fabricated MZM in terms of its static electrical behaviour, RF frequency response and linearity. The second section describes the experimental setup for the PAM-4 and DMT transmission links and reports the extracted Bit-Error-Ratios (BERs) and spectral efficiency (SE) values for each case. Finally, the third section analyses the design of a number of novel topologies for linear modulators through modelling of their transfer functions.

5.1 Characterisation of the Mach–Zehnder Modulator

The Mach–Zehnder Modulator that was used for the transmission experiments was designed by Dr. D. J. Thomson and fabricated externally by the Institute of Microelectronics (IME) in Singapore for the SPFS project. The packaging of the fabricated optical chip with an electrical Printed Circuit Board (PCB) was implemented by Dr. Li Ke. The characterisation experiments were performed by the author and Dr. C. Lacava, in order to evaluate the compatibility of the device with advanced modulation formats. This section reports on the design strategy, the fabrication parameters and the characterisation measurements.

The modulator was designed as an imbalanced push-pull MZM, with multi mode interference (MMI) couplers of a 50:50 coupling ratio used to split and recombine the two arms and two grating couplers at the input and output of the device to facilitate fibre-to-chip coupling. Two identical 1.8-mm-long phase shifters were embedded in its two arms to induce a refractive index change on application of electrical voltage, based on the plasma dispersion effect. They consisted of silicon waveguide sections that were doped by means of phosphorus and boron ion implantation to create a p-n junction as illustrated in Fig. 5.2. As it is essential for the MZM to support high baudrates for high capacity applications, the p-n junction was designed for operation in the high-bandwidth carrier-depletion regime, which requires the driving voltage applied to reverse bias the

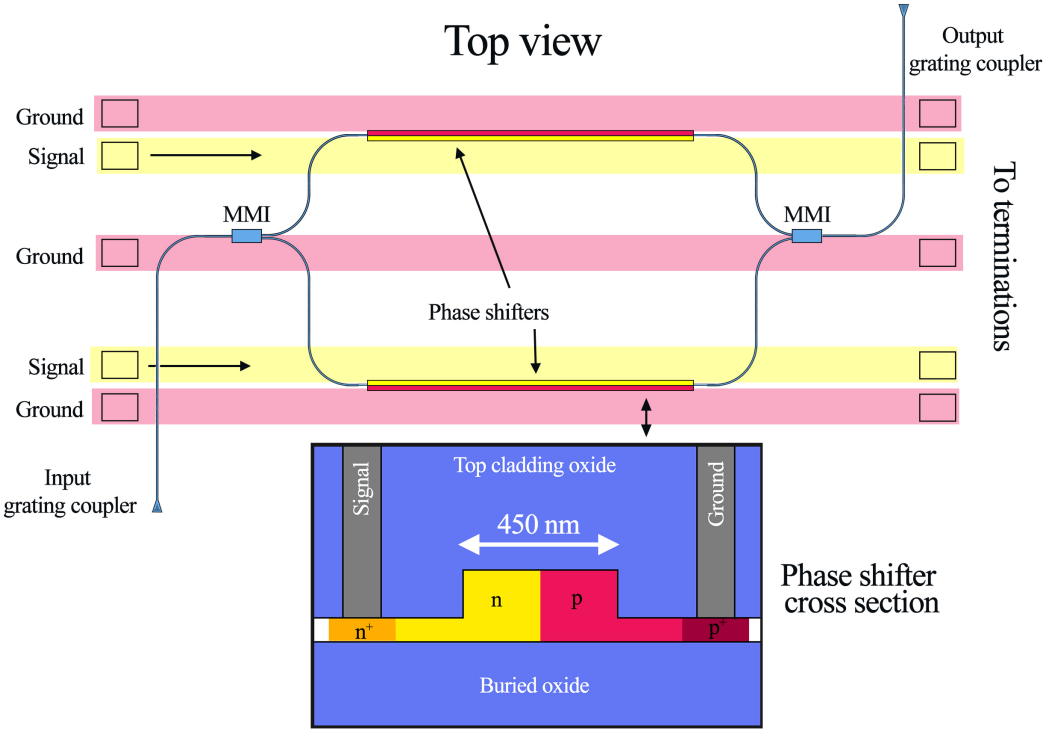

FIGURE 5.2: Top view schematic of the MZM. Inset: Doped waveguide cross-section.

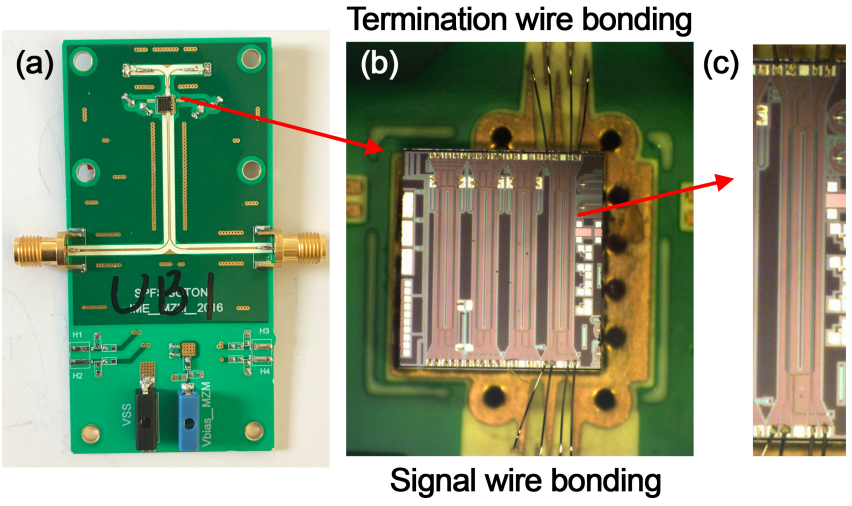

FIGURE 5.3: Top view photograph of the packaged MZM.

junction. For the differential RF signals to bias the doped waveguides, two electrical transmission lines were drawn on an aluminium layer on top of the SiO_2 cladding to form 50 Ω coplanar waveguides traversing the length of the MZM arms. On each side they were equipped with a set of 5 metallic pads in the Ground-Signal-Ground-Signal-Ground (GSGSG) arrangement that provided their interface with the external electrical signal source (pink and yellow pads in Fig. 5.2). The final device was surface mounted to an electrical PCB that comprised two SMK connectors leading to two microstrip lines that were wire bonded to the MZM electrical pads in order to route the differential RF signals to the optical modulator. 50 Ω terminations were also built on the PCB and wire-bonded to the output of the MZM transmission lines. Fig. 5.3 (a) shows a microscope image of the packaged device (photonic chip attached to the PCB) from a top perspective view, while Figs. 5.3 (b) and (c) show magnified photographs of the silicon MZM structure and the bonding wires.

5.1.1 Transfer function and frequency response measurement

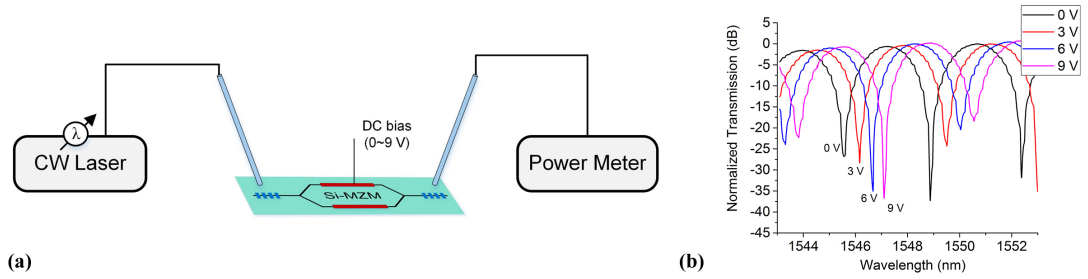

FIGURE 5.4: (a) Experimental setup for the characterisation of the MZM, (b) Normalised MZM optical transmission for different DC voltages applied to a single RF input port.

The optical transfer function of the MZM was first measured by sweeping the input wavelength to the device and measuring the output power at each wavelength sequentially. This measurement was repeated for different bias voltages applied to the modulator, producing a series of plots that describe the static modulation properties of the MZM (with no RF signal applied). The experimental setup used to implement this measurement is illustrated in Fig. 5.4 (a). At each sweep step, an external cavity laser (ECL) provided a single-wavelength optical input to the MZM and the power collected at the device output was measured by a power meter. Coupling to and from the grating interfaces of the MZM was realised through polarisation-maintaining (PM) fibres that were positioned at an angle to the chip surface, while their facets were rotated appropriately so that their primary polarisation axis was aligned to the transverse electric (TE) mode in the silicon waveguides. A bias tee was used to apply DC voltage to one arm of the modulator from an external power supply. The transfer function and its shift in wavelength as a result of the phase shift ($\Delta\phi$) induced by the MZM DC bias are shown in Fig. 5.4 (b). To evaluate the modulation efficiency, the phase change $\Delta\phi$ was quantified as a function of

the applied voltage by measuring the wavelength shift $\Delta\lambda$ of the transmission nulls in Fig. 5.4 (b) for each voltage value and substituting it into the following equation:

$$\Delta\phi = \frac{2\pi \cdot \Delta\lambda}{FSR} \tag{5.1}$$

where FSR is the Free Spectral Range of the MZM. The results are illustrated in Fig. 5.5 (a), while the property extracted from this data to quantify the modulation efficiency of the MZM is the $V_\pi L$. The voltage required to achieve a π phase shift V_π was evaluated for each point individually using a first-order approximation [128–130]:

$$V_\pi L = \frac{\pi V_{bias} L}{\Delta\phi} \tag{5.2}$$

and the modulation efficiency $V_\pi L$ is plotted as a function of V_{bias} in Fig. 5.5 (b).

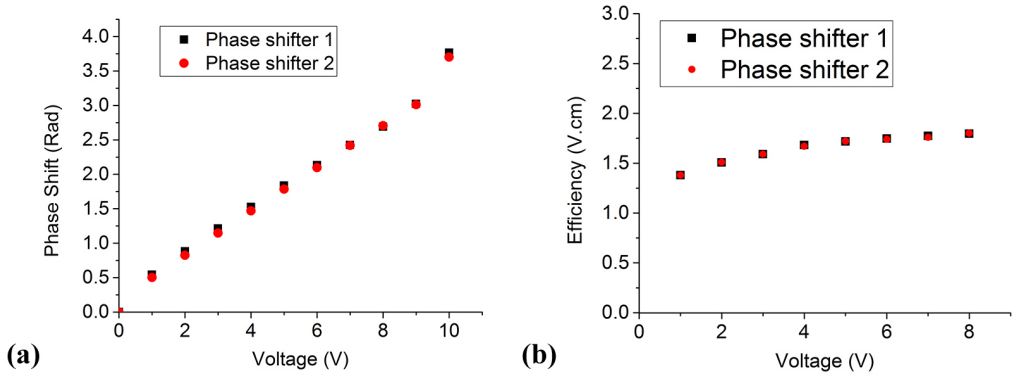

FIGURE 5.5: (a) Measured MZM phase shift for a given applied voltage, (b) Modulation efficiency measured for different bias voltages.

Regarding the E/O properties of the MZM in the presence of RF signals, a series of bandwidth measurements were conducted to evaluate the effect that the electrical packaging had on the frequency response of the final device. First, the electrical S_{21} transmission of the coplanar RF waveguides on the unpackaged optical chip was measured. Coupling to the transmission line was achieved through high-speed electrical RF probes in order to connect it to a 50-GHz Network Analyser and the frequency response is shown in Fig. 5.6. It is noted that the bandwidth evaluation in electrical transmission measurements on Travelling-Wave MZMs uses the -6.4-dB threshold in order to be considered a comparable metric to the E/O 3-dB bandwidth of the MZM, as proven in [131]. As shown in Fig. 5.6 (a), the measured -6.4-dB bandwidth for the unpackaged MZM was 26 GHz at a DC bias voltage of 8 V applied to the phase shifter. Next, the S_{21} parameter was measured for the PCB which comprised a pair of 50-Ω microstrip lines with two SMK connector interfaces and its frequency response revealed a -6.4-dB bandwidth of 10.02 GHz. Finally, the same type of measurement was conducted for the packaged MZM, showing a significant deterioration of the -6.4-dB bandwidth, at a value of 4.45 GHz for a DC bias voltage of 8 V. It is apparent that the microstrip lines on the PCB

along with the wire-bonding to the optical chip resulted in a decrease in the electrical bandwidth available to drive the MZM. The purpose of these measurements was to identify the sources of bandwidth limitation in the packaged device, by isolating the factors associated with purely electrical components from the E/O phase shifter design. Lastly, the final packaged device was also operated under excitation from an optical source in order to evaluate its E/O frequency response. An optical carrier was therefore modulated by a range of RF frequencies and the output was detected by a photodiode with a flat frequency response. The result of this RF frequency sweep method is presented in Fig. 5.6 (b). It is evident that the 3-dB E/O bandwidth of 4.33 GHz is only slightly different from the electrical bandwidth of 4.45 GHz, which suggests that the bottleneck in the device bandwidth appears at the stage of mounting the optical chip to the PCB. To mitigate the detrimental effect of the electrical packaging on the device bandwidth, other techniques such as flip-chip bonding are currently being considered for future implementations.

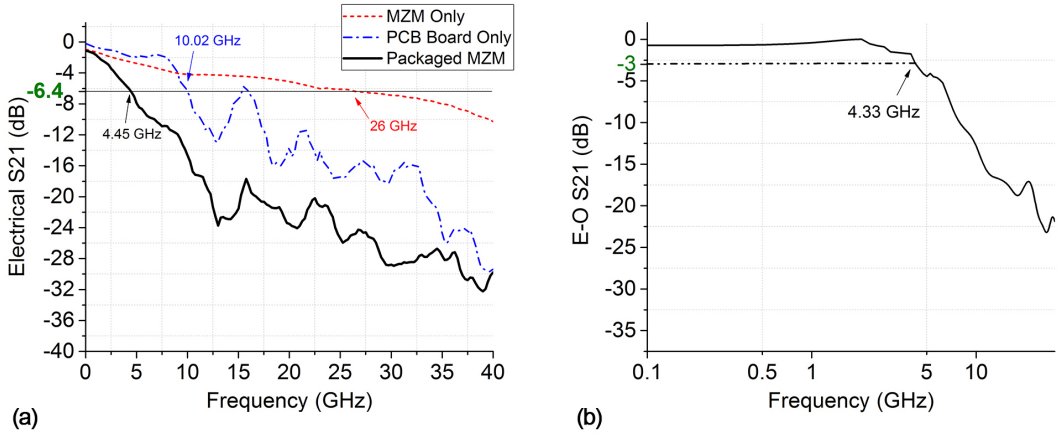

FIGURE 5.6: (a) Electrical S_{21} parameter measured on the MZM device only (red dotted curve), the PCB only (blue dash-dotted line) and the packaged MZM device (black line), (b) E/O S_{21} parameter measured on the packaged device.

5.1.2 Linearity Evaluation

The final step of the characterisation experiments was the evaluation of the modulator linearity. As mentioned in the previous section, this is crucial for transmissions of PAM-4 and DMT data, as these modulation formats are extremely sensitive to nonlinear distortions caused by the link components [132, 133]. The goal of this step was to quantify the spurious-free dynamic range ($SFDR$) of the MZM as a metric of its linearity. To this end, the two-tone test was performed on the packaged modulator, according to the methodology reported in Section 2.2.2. It should be noted that due to the dual-drive push-pull configuration of the packaged MZM, no second-order nonlinear distortions are present in the system [69, 134, 135], therefore the main limitation comes from the third-order distortions. Out of these, the intermodulation distortion components (IMD3) play

the most important role in signal deterioration as they are always situated very close to the fundamental frequencies, whereas part of the harmonic distortion components (HD3) appear at out-of-band frequencies that can be filtered out and are generally weaker in amplitude.

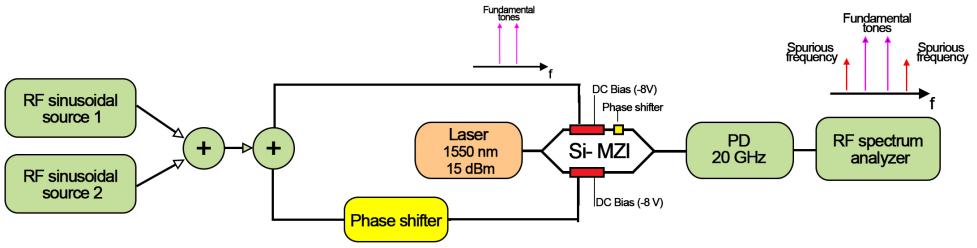

FIGURE 5.7: Experimental setup for the MZM linearity measurement.

Under these considerations, the measurement scheme illustrated in Fig. 5.7 was set up to evaluate the $SFDR_{IMD3}$ of the device. The MZM was set to operate at its quadrature point (output power at -3 dB of its maximum transmission) by tuning its optical input to the appropriate wavelength via an ECL CW source. The optical interface between the chip and the fibre setup was again enabled by the vertical grating couplers and PM fibres that were set up to excite the TE waveguide mode. The optical power launched to the chip was 15 dBm and the received modulated signal was collected by a 20-GHz photodetector and sent to a RF spectrum analyser to monitor the final RF frequency response. The RF input to the MZM consisted of a pair of single-frequency signals that were generated by RF frequency synthesisers and combined together through a 3-dB RF coupler (Wilkinson power divider). This signal was subsequently split into two appropriately phase shifted paths to differentially drive the modulator. In order for the MZM to operate in the carrier-depletion regime of the p-n junction, a DC reverse bias voltage was applied to it and the modulator linearity was investigated for different bias values.

The $SFDR_{IMD3}$ was measured for different modulating centre frequencies, namely 2, 3 and 5 GHz. Around these central values, the two input tones had a spacing of 0.01 GHz and the RF spectrum analyser collected the output with a resolution bandwidth of 100 Hz and a background noise level of -157 dBm. The RF P_{in}-P_{out} plots for the investigated frequencies and bias voltages are shown in Fig. 5.8 (a)-(c), from which the $SFDR_{IMD3}$ and IIP_3 parameters are calculated. As explained in Section 2.2.2, the measured parameters describe the full communication link, which means it reflects the nonlinearity of the full transmission setup. For this reason, a reference measurement on a commercial 40-GHz $LiNbO_3$ modulator was performed and the comparison with the silicon MZM is shown in Fig. 5.8 (d)-(e), where all measurements are normalised to a

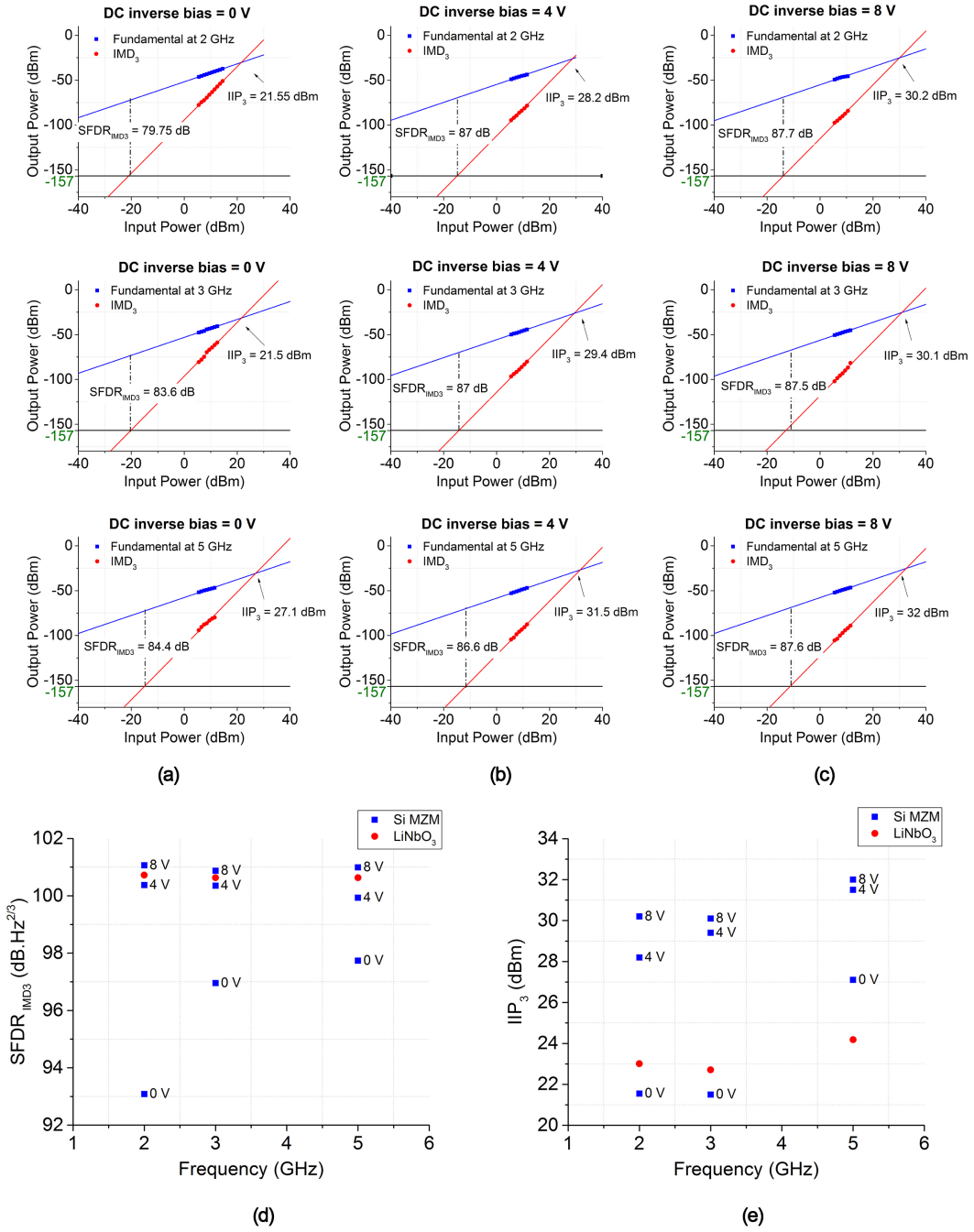

FIGURE 5.8: (a) - (c): RF P_{in}-P_{out} graphs for the fundamental and IMD3 components of the packaged MZM biased at 0, 4 and 8 V and at driving frequencies of 2, 3 and 5 GHz (resolution bandwidth of 100 Hz), (d), (e): Comparison of calculated $SFDR_{IMD3}$ and IIP_3 parameters (resolution bandwidth of 1 Hz) between the silicon MZM and a $LiNbO_3$ operated at its quadrature point (V_{bias} = 2.1 V).

resolution bandwidth of 1 Hz. It is clear from this comparison that the silicon MZM exhibits remarkable linearity properties when biased at 8 V and driven with 5-GHz signals. Its $SFDR_{IMD3}$ value is equal to 101 dB $Hz^{2/3}$ and the $IIP3$ value is larger than 30 dBm, which surpasses the performance of the commercial $LiNbO_3$ modulator. A general comparison to the linearity metrics for Si-based modulators reported in the literature is presented in Table 5.1. The table shows that considering both the $SFDR_{IMD3}$ value and the frequency for which it is achieved, the investigated MZM performs better than other Si MZMs reported in the literature, according to the measurements in the communication link considered in this experiment. It can be seen that the device that shows a higher $SFDR_{IMD3}$ value at a higher frequency [136], as well as a number of devices in this Table that exhibit high linearity [137, 138], take advantage of a different modulator topology, the Ring-Assisted MZI (RAMZI) configuration. The design of such modulators is discussed in the final section of this Chapter.

TABLE 5.1: **Linearity of various Si-based modulators present in the literature**

	$SFDR_{IMD3}$ **[dB** $\mathbf{Hz^{2/3}}$**]**	**Central Frequency [GHz]**
[139] Si ring modulator	84	1
[137] Si ring-assisted MZM	99	10
[140] Si MZM	113.7	2
[138] Si ring-assisted MZM	71.65	1
[136] Si+III-V ring-assisted MZM	117.5	10
[141] Si MZM	95	1
[142] Si MZM	97	1
[26] This work (Si MZM)	101	5

5.2 Mach–Zehnder Modulator in PAM-4 and DMT transmission links

This section reports the transmission experiments performed using the electrically packaged Mach–Zehnder Modulator that was described in the previous section. The following experiments were conducted by the author and Dr. C. Lacava, in a collaboration with the group in the State Key Laboratory of Advanced Optical Communication Systems and Networks of Peking University in Beijing, China. In particular, PAM-4 and DMT data were modulated using the MZM and were launched to various lengths of optical fibre (SMF) to test the transmission reliability in different propagation lengths through Bit-Error-Ratio (BER) measurements. The main results include 40 Gbits/s PAM-4 transmission up to 20 km of SMF and 49.6 Gbits/s DMT transmission up to 40 km of SMF. The latter, which proved to offer the best performance for medium-reach links, showed the highest spectral efficiency of 5 b/s/Hz reported in the literature for an unamplified Direct-Detection link with a silicon photonic modulator.

5.2.1 Data transmission experiment

The experimental scheme used for the data transmission is shown in Fig. 5.9. Blocks in yellow represent the software implementation of the modulation formats, while the rest of the components represent hardware instruments. The equipment consisted of a 32-GS/s DAC (of a 20-GHz bandwidth) that converted the digital signal to an electrical differential output which was amplified to drive the modulator (4 Volts peak-to-peak was applied to each MZM arm). The optical carrier was generated by a tunable CW laser at the wavelength that corresponded to the 3-dB operating point of the modulator. A bias voltage of 8 V was used on the MZM, as it showed the best linearity properties at that value during the characterisation stage. The modulated signal was sent to propagate through spools of SMF of variable length (0 - 50 km) before being collected by the receiver. At the receiver stage, a Variable Optical Attenuator (VOA) along with an EDFA were used as a noise source and the final amplified signal was fed to a 30-GHz photodetector integrated with a transimpedance RF amplifier (TIA). An 80-GS/s ADC (of a 35-GHz bandwidth) converted the signal to a digital form for offline processing.

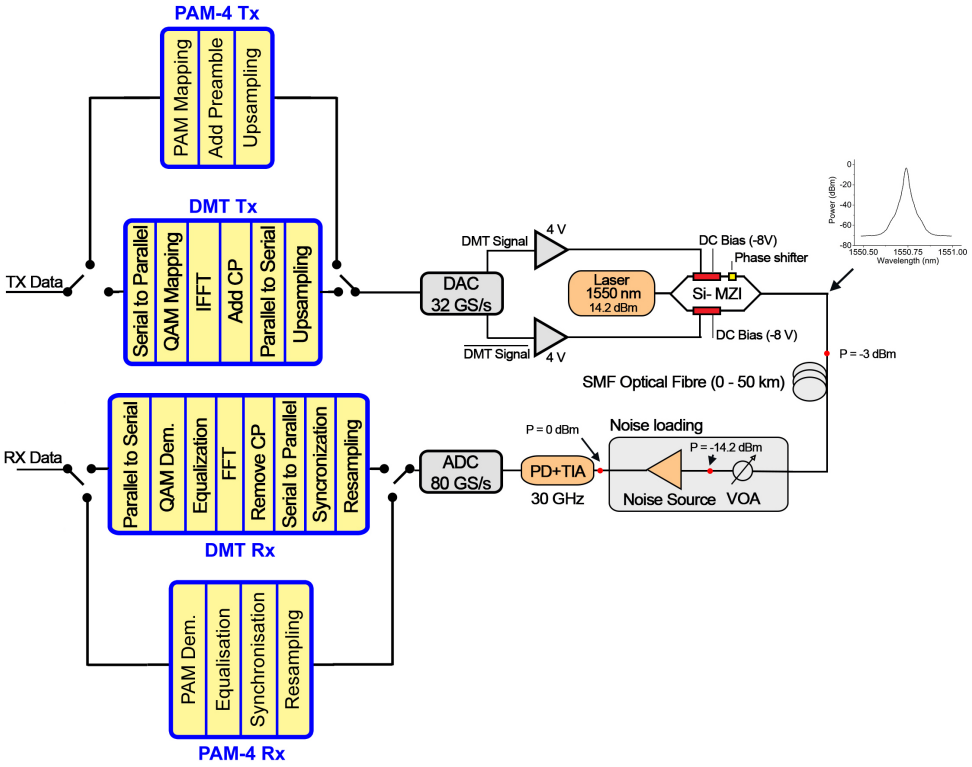

FIGURE 5.9: Experimental Scheme for the PAM-4 and DMT transmission links.

The data were generated using the block diagrams described in the Background section. In the case of PAM-4, Pseudorandom Binary Sequences of length 2^{15}-1 were mapped to the PAM-4 symbols and were upsampled to be sent as an electrical signal from the DAC at a rate of 20 Gbaud. A preamble was also added at the start of each sequence for synchronisation purposes. At the receiver side, the signal captured at a rate of 80 GS/s

was resampled and the start of the sequence was identified by locating the preamble. After equalisation, the PAM-4 symbols were mapped to bits and the received sequence was compared to the original transmitted one. The eye diagrams for the signal after equalisation are shown in Fig. 5.10 for back-to-back as well as after propagation in a 20-km fibre, to provide some visual insight of the quality of the received signal.

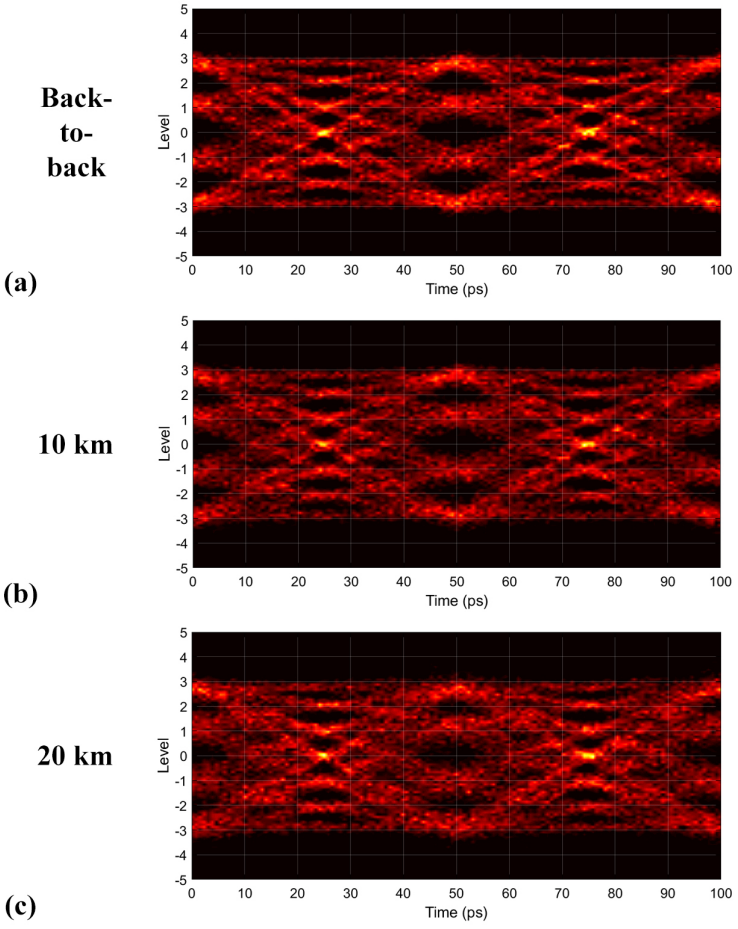

FIGURE 5.10: Eye diagrams for the PAM-4 data after equalisation (a) in a back-to-back system, (b) after propagation in 10 km of SMF and (c) in 20 km of SMF.

In the case of DMT, the software implementation obviously required higher complexity. The PRBS was first parallelised in order to be divided into the different subcarriers of the DMT frame. Then, the distribution of the bits across the available frequencies was selected based on the rate-adaptive water-filling algorithm described in detail in [64]. The role of the algorithm was to decide which QAM format each subcarrier can support, based on the SNR available at that frequency, and map the bits accordingly in order to maximise the total transmission bit rate. The SNR information on the different subcarriers was provided by a channel estimation performed at the start of the experiment and is shown in Fig. 5.11 (a) for the 40-km-long link. This channel estimation was performed by transmitting a QAM-symbol multi-carrier signal with a uniform bit distribution over the RF frequency spectrum and receiving the output signal from the

MZM. The frequency bandwidth used for data allocation was 10 GHz and it was divided into 256 evenly spaced subcarriers, out of which 239 were loaded with bits. Fig. 5.11 (b) shows the bit distribution across the subcarriers. After the binary sequence was mapped to the QAM formats of each subcarrier, a frame of frequency-domain signals was created. For each signal in the frame, the complex conjugate was generated and appended to the original and the total sequence was converted to a real-valued time-domain digital waveform through an IFFT process. A 3.6% cyclic prefix (CP) was added at the start of each waveform and the resulting frame was serialised into one large sequence. A 2% preamble was appended to the sequence for synchronisation purposes and the result was sent to the DAC after appropriate upsampling. A continuous waveform consisting of repetitions of this DMT sequence propagated through the optical channel and was received by the ADC to be converted to a digital signal.

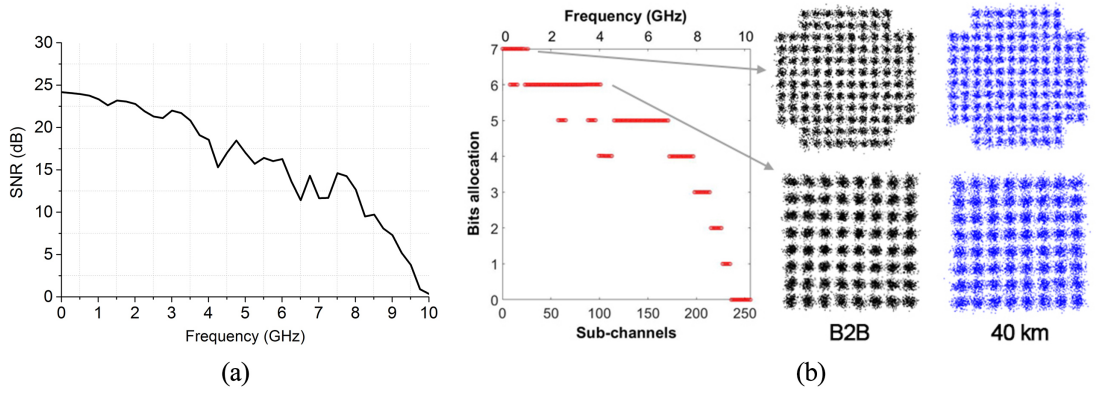

FIGURE 5.11: (a) SNR profile of the link containing 40 km of SMF, (b) Bit loading profile for the 40-km-long transmission link, with constellation diagrams for the 128-QAM and 64-QAM data in the back-to-back and 40-km links.

This signal was then resampled and the DMT sequence was extracted from it by a synchronisation algorithm that identified the preamble position. Next, the sequence was parallelised to form the individual time-domain signals of the DMT frame. After CP removal, the signals were transformed to their frequency-domain counterparts through a FFT process, to be equalised and mapped back to bit sequences. Finally, the bit sequences were all serialised into a single bit stream which was compared to the original transmitted PRBS, so that the transmission bit-error-ratio (BER) could be evaluated.

In total, 1342 symbols were included in one frame spanning the 10-GHz bandwidth, which corresponded to a capacity of 52.42 Gb/s (frame transmission time of 25.6 ns). Since certain samples represent the CP and the preamble and do not carry information, the net transmitted capacity was calculated to be 49.6 Gb/s. A summary of the properties describing the DMT format implemented in this experiment is given in Table 5.2.

TABLE 5.2: **DMT parameters for the 40-km-long link**

Number of channels (allocated)	FFT size	CP	Preamble	Sampling Rate
239	512	3.6%	2%	19 GS/s

As shown in Fig. 5.11 (b), the highest-order QAM format used is 128-QAM and two example constellation diagrams for 128-QAM and 64-QAM are presented for the back-to-back link as well as after propagation in 40 km of SMF. Even though a large number of symbols is used in these formats, it is evident from the received sample distribution that the data is still retrievable, without large signal quality deterioration. This can be attributed to the linearity of the MZM that maintained the amplitude scaling of the QAM symbols.

As mentioned before, the performance of the links was eventually evaluated through BER measurements. The BER values for different lengths of SMF propagation are presented in Fig. 5.12. Because the PAM-4 format was sent at a 20-GBaud rate, the blue curve corresponds to a capacity of 40 Gb/s, while the black curve describing the DMT format corresponds to 49.6 Gb/s. The BER plots indicate that the maximum lengths for which BER values are below the 7% Hard Decision - Forward Error Correction (HD-FEC) Limit ($3.8 \cdot 10^{-3}$) are 20 km for PAM-4 and 40 km for DMT. DMT clearly has an advantage over PAM-4, since it achieves both higher capacity and longer reach in transmission for the same available RF spectrum.

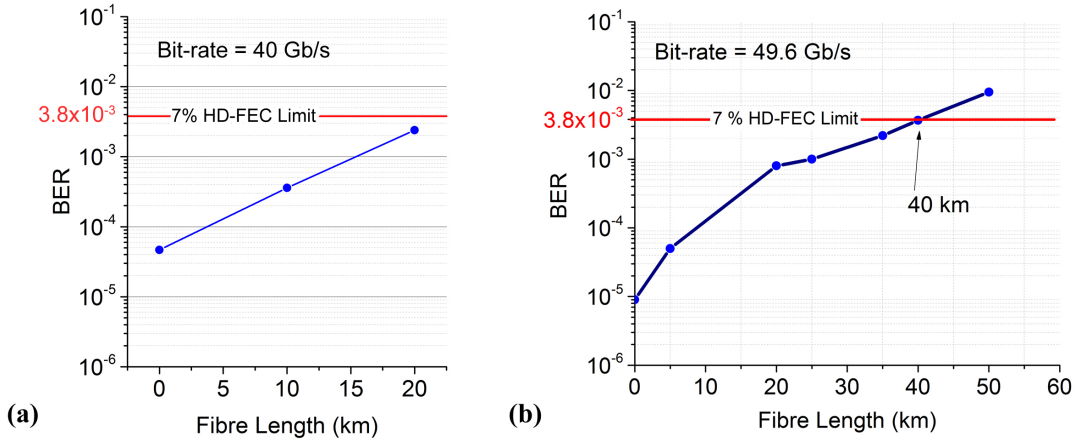

FIGURE 5.12: Bit error ratio (BER) vs. propagation length in SMF for the cases of (a) PAM-4 and (b) DMT modulation formats.

5.2.2 Discussion

In order to gain some meaningful insight on these measurements, an analysis of the causes for signal quality deterioration was performed. Apart from optical loss, the main factor responsible for BER degradation in wideband Intensity Modulated (IM)-DD links spanning long lengths of SMF is chromatic dispersion (CD) [143]. Because

modulation in an IM-DD system generates a double sideband around the optical carrier, the cumulative effect of the dispersion after long-reach propagation induces a relative phase difference between the two sidebands, which significantly distort the received signal. This distortion manifests itself as a decrease in SNR and is most prominent in signals with high-RF-frequency content [144]. In quantitative terms, the SNR penalty introduced by this effect can be modelled by the following equation [143, 145]:

$$SNR_{penalty} = cos^2(\frac{\pi\lambda^2}{c}DLf^2) \tag{5.3}$$

where λ is the optical carrier central wavelength, c is the speed of light, D is the chromatic dispersion coefficient of the fibre, L is the propagation length and f is the baseband frequency modulating the optical carrier. The SNR penalty is plotted as a function of the RF frequency for three different lengths of SMF (10, 40, 50 km) in Fig. 5.13.

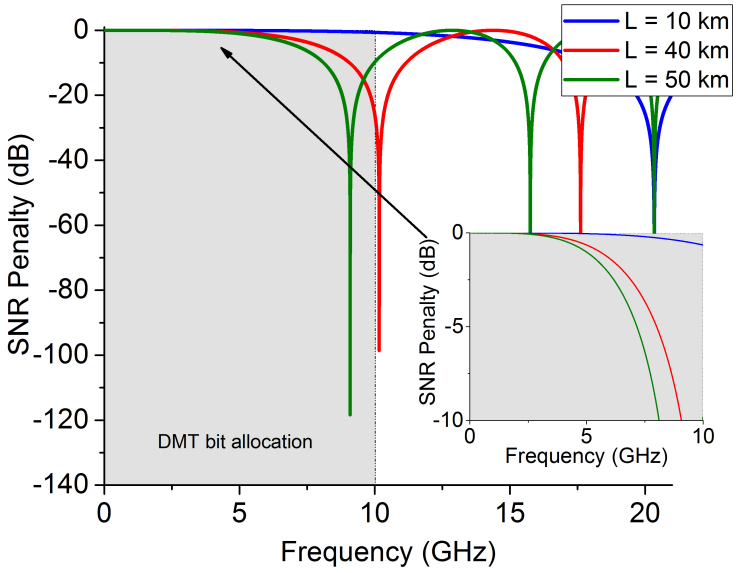

FIGURE 5.13: SNR penalty induced for different propagation lengths of SMF due to chromatic dispersion (central wavelength of 1550 nm).

The blue curve represents the SNR penalty exhibited in a 10-km-long link across a 20-GHz span in the RF spectrum. As is evident, this length does not cause significant deterioration in the 10 GHz band that was used in the modulation schemes present in the MZM experiments (represented by the shaded area in the plot). However, at a length of 40 km, frequencies between 7.5 and 10 GHz show penalties of more than 3 dB (red curve), while in the 50-km case the distortion is even more aggravated. The power fading dips in the graph suggest that for lengths of 40 km or more, the modulator bandwidth stops being the main limiting factor in capacity, as a wider-band signal would still experience deterioration at frequencies higher than 10 GHz because of the fibre dispersion. A method to overcome this type of signal distortion would involve a

DMT format with a complex enough bit allocation algorithm to discretise the available spectrum more finely and efficiently distribute the data to the usable parts, away from the regions where the effect of power fading is prominent [146, 147].

TABLE 5.3: **Baseband SE for various transmission systems reported in the literature**

	Format	**Amplified**	**CD compensation**	**Distance [km]**	**Baseband SE [b/s/Hz]**	**Rate [Gb/s]**
Si-MZM with no electrical packaging [147]	DMT	No	No	10	4.4	107
Si-MZM with no electrical packaging [146]	DMT	No	No	4	3	90
Si-MZM with no electrical packaging [146]	SSB-DMT	No	No	40	2.8	100
Si-ring resonator with no electrical packaging [148]	PAM-4	Yes	No	20	4	40
Directly Modulated Laser (20-GHz E/O bandwidth) [135]	PAM-4	Yes	No	100	4	2 × 56
Directly Modulated Laser (15-GHz E/O bandwidth) [149]	DMT	No	No	80	2	49
Si-photonic Stokes transmitter based on I/Q modulator[150]	16-QAM	Yes	Yes	100	6.4	128
I/Q Modulator with electrical packaging [151]	16-QAM	Yes	No	320	4	50
This work	PAM-4	No	No	20	4	40
This work [26]	DMT	No	No	40	5	49.6

Based on this discussion, a comparison of the modulation formats implemented in this experiment to the relevant literature is presented. A useful metric relating to the capability of utilising the available bandwidth is the baseband spectral efficiency (SE), which is defined as the link capacity over the frequency band (measured in its baseband form) used for data loading. According to this definition, the PAM-4 format has a SE of 4 b/s/Hz, while the DMT format implemented in this experiment showed a SE of 5 b/s/Hz. Apart from the SE differences, the transmission length achieved with DMT (40 km) was also twice as long as the one achieved with PAM-4 (20 km) for BERs below the FEC limit. This shows the advantage of the DMT format in band-limited systems, which stems from introducing more complex T_x-R_x algorithms to make more efficient use of parts of the spectrum with different SNR values. Other implementations reported in the literature are presented in Table 5.3 to provide context to the results of this experiment. The silicon MZMs reported in [146] and [147] exhibit >10 GHz bandwidths but the transmission lengths do not surpass 10 km due to the CD-induced power fading effect. A 40-km transmission is indeed reported in [146] by using a single-sideband (SSB) DMT format, which however adds to the system complexity and renders it less attractive for low-cost applications. Simplicity in the implementation is provided by PAM-4 systems, which makes them very attractive for data-centre IM-DD links as reported in [148] and [135], but the baseband SE associated with this format cannot surpass 4 b/s/Hz as there is no dynamic bit distribution technique to efficiently use the available bandwidth. A SE value of 6.4 b/s/Hz has been reported in [150], demonstrating a 100-km transmission link with a capacity of 120 Gb/s, however the use of an I/Q modulator, a Stokes

receiver and a CD compensation technique significantly increase the complexity of this system. The DMT experiments presented in this chapter [26] demonstrated the use of a highly linear Mach–Zehnder modulator for the transmission of data at 49.6 Gb/s over 40 km of SMF, amounting to a SE of 5 b/s/Hz, which is the highest value reported for a conventional silicon photonic IM-DD system.

5.3 Optimisation of linear performance: RAMZI

From the previous sections, it transpired how PAM-4 and DMT formats pose new challenges for the design of silicon modulators, which have to exhibit very linear behaviour in order to achieve reliable data transmission. For the Mach–Zehnder modulator presented in Section 5.1, the design of the p-n junctions serving as the phase modulators in its two arms allowed for high SFDR values for the system that was built to transmit the data. This approach addressed the problem of the electrical nonlinearity that the reverse-biased p-n junction induces to a silicon modulator [67] and in the case of a MZM, this concerns the $n_{eff}(V)$ function which represents the first block in the diagram of Fig. 2.24.

However, other methods to improve the linearity of a MZM have been proposed in the literature, which aim to linearise the inhererently sinusoidal transmission function $P_{opt}(n_{eff})$ of the Mach–Zehnder Interferometer arrangement (second block in Fig. 2.24) by introducing new photonic circuit topologies [152]. In this case, linearisation occurs as a result of the combination of the transfer functions of multiple components used to form the final modulating device. The combinations that are mostly investigated in the literature include connecting two Mach–Zehnder modulators in series or in parallel [153, 154] or coupling a Mach–Zehnder interferometer to a Ring Resonator modulator, which is also called the Ring-Assisted Mach–Zehnder Interferometer (RAMZI) modulator [155–158]. Implementations of the RAMZI arrangement on silicon platforms have already been demonstrated, both in monolithic structures [137, 138, 159] and after heterogeneous integration with III-V materials [136].

This section reports the design of a number of silicon RAMZI modulator configurations with tunable linearity. In particular, it investigates the linearity dependence on the Ring-to-MZI coupling for the purpose of fabricating a RAMZI modulator with a voltage-controlled linearity. The design process is implemented in a purpose-built MATLAB software code that uses the analytical expressions for the MZI and RRM transfer functions to derive the total device transfer function. It then simulates the two-tone linearity measurement technique. The driving signals of this virtual modulator are modelled as sinusoidal refractive index changes incorporated into the device total transfer function and therefore the SFDR is evaluated. By sweeping a number of design parameters, the changes in the SFDR and therefore the linearity behaviour of the modulator are

analysed. All design parameters are selected to match the capabilities of the available fabrication facilities for devices on the SOI platform.

5.3.1 Design of the RAMZI modulators

The driving signal of a Mach–Zehnder Modulator is experienced as a change in the refractive index Δn_{eff} of one of its arms (or both of its arms). Therefore, the linearity of a MZM is determined by the dependence of the output optical intensity I_{out} on the induced refractive index change Δn_{eff}. For a single-drive MZM that is operated at its quadrature point (intensity 3 dB lower than maximum), this dependence is sinusoidal:

$$I_{out} = \frac{I_{in}}{4}\left[2\alpha^2 + 2\alpha^2 sin\Big(\Delta\phi(\Delta n_{eff})\Big)\right] \tag{5.4}$$

where $\Delta\phi(\Delta n_{eff}) = k_0 \Delta n_{eff} L$ expresses the induced phase difference on one of the MZM arms which unbalances the modulator and changes its output intensity. The parameter α represents the optical loss accumulated after propagation over the length of a MZI arm and I_{in} is the input optical intensity to the MZM. Note that this form for I_{out} is derived from eq. (2.37) when an appropriate $\Delta\phi_{bias}$ has been applied to a balanced modulator to bias it at the quadrature point, where $I_{out}(0) = \frac{I_{max}}{2}$.

The nonlinear components of the sinusoidal function in (5.4) can be determined by expanding it to its polynomials:

$$I_{out}(\Delta\phi) = \frac{I_{in}}{4}\left[2\alpha^2 + 2\alpha^2\Big(\Delta\phi(\Delta n_{eff}) - \frac{1}{6}\Delta\phi^3(\Delta n_{eff}) + \frac{1}{120}\Delta\phi^5(\Delta n_{eff}) + ...\Big)\right] \tag{5.5}$$

where it is evident that $I_{out}(\Delta\phi)$ contains odd-order nonlinear terms, with the most prominent one being the third-order term. In the case of a conventional MZM, $\Delta\phi$ is proportional to Δn_{eff}, therefore $I_{out}(\Delta n_{eff})$ also exhibits third-order nonlinearity.

The nonlinearity inherent in the $I_{out}(\Delta\phi)$ function of a Mach–Zehnder Interferometer topology cannot be eliminated. The concept of linearisation by coupling the MZI to a ring resonator is based on changing the relation between $\Delta\phi$ and Δn_{eff} by introducing a component that exhibits a nonlinear $\Delta\phi(\Delta n_{eff})$ function. Then, the nonlinear terms of $\Delta\phi(\Delta n_{eff})$ can counterbalance the nonlinearity in $I_{out}(\Delta\phi)$ and produce a linear relation for $I_{out}(\Delta n_{eff})$. It can be proven that the phase transfer function of a ring resonator modulator $\phi_{RR}(\Delta n_{eff})$, when operated at its off-resonance point, can eliminate the third-order nonlinear terms of the MZI, for an appropriate MZI-to-RR coupling condition [155]. A schematic of this Ring-Assisted Mach–Zehnder Interferometer (RAMZI) Modulator is given in Fig. 5.14.

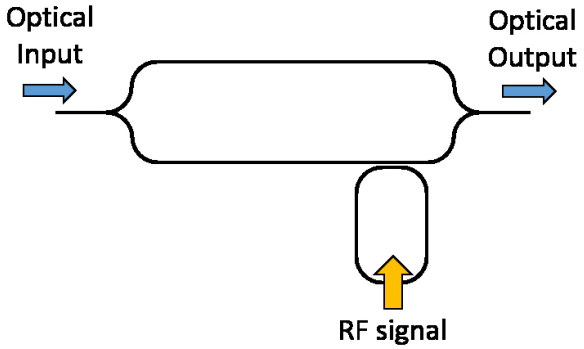

FIGURE 5.14: Schematic of a RAMZI modulator.

To model the RAMZI modulator, a MATLAB code was composed in order to utilise the analytical functions for the electric field transfer functions of the Mach–Zehnder Interferometer (MZI) and the Ring Resonator (RR). These complex transfer functions are repeated here for consistency:

$$T_{MZI} = \frac{1}{2}\left[\alpha_{MZI,1}e^{-jk_0 n_{eff,1}L_1} + \alpha_{MZI,2}e^{-jk_0 n_{eff,2}L_2}\right] \tag{5.6}$$

$$T_{RR} = \frac{t - \alpha_{RR}e^{-jk_0 n_{eff,RR}L_{RR}}}{1 - \alpha_{RR}te^{-jk_0 n_{eff,RR}L_{RR}}} \tag{5.7}$$

where the symbol representations are defined in Table 5.4.

TABLE 5.4: **Symbols used in Equations (5.6) and (5.7)**

Symbol	Physical property
k_0	Free-space angular wavenumber
$\alpha_{MZI,i}$	Loss due to propagation in the i-th MZI arm waveguide
$n_{eff,i}$	Effective refractive index of the i-th MZI arm waveguide
L_i	Length of the i-th MZI arm waveguide
α_{RR}	Loss due to propagation in the RR circumference
$n_{eff,RR}$	Effective refractive index of the RR circumference waveguide
L_{RR}	Length of the RR circumference
t	Through Coupling Coefficient

To construct the transfer function of a RAMZI modulator with one ring coupled to one of the MZI arms, T_{RR} needs to be incorporated into T_{MZI} as shown below:

$$T_{RAMZI} = \frac{1}{2}\left[\alpha_{MZI,1}e^{-jk_0 n_{eff,1}L_1} \cdot T_{RR} + \alpha_{MZI,2}e^{-jk_0 n_{eff,2}L_2}\right] \tag{5.8}$$

The modulating signal of a RAMZI modulator essentially drives the RRM, changing the effective refractive index in the ring circumference. Hence, the RR effective refractive index is written as $n_{eff,RR} = n_{eff,bias} + \Delta n_{eff}$ and T_{RR} is a function of the signal Δn_{eff}. This shows the dependence of the RAMZI optical output to the modulating signal:

$$T_{RAMZI}(\Delta n_{eff}) = \frac{\alpha_{MZI}}{2}\left[e^{-jk_0 n_{eff} L} \cdot T_{RR}(\Delta n_{eff}) + e^{-jk_0 n_{eff} L}\right] \tag{5.9}$$

where the MZI arms were considered to be equal in length.

5.3.2 Simulation of the linearity measurement scheme

The transfer function in eq. (5.9) was written in a MATLAB routine in order to simulate the system described by the block diagram in Fig. 5.15. This virtual communication link represents the two-tone test described in Section 2.2 and was modelled analytically to evaluate the linearity of the modulator for different configurations by quantifying the Spurious-Free Dynamic Range (SFDR) which was calculated by measuring the spectral content of the output.

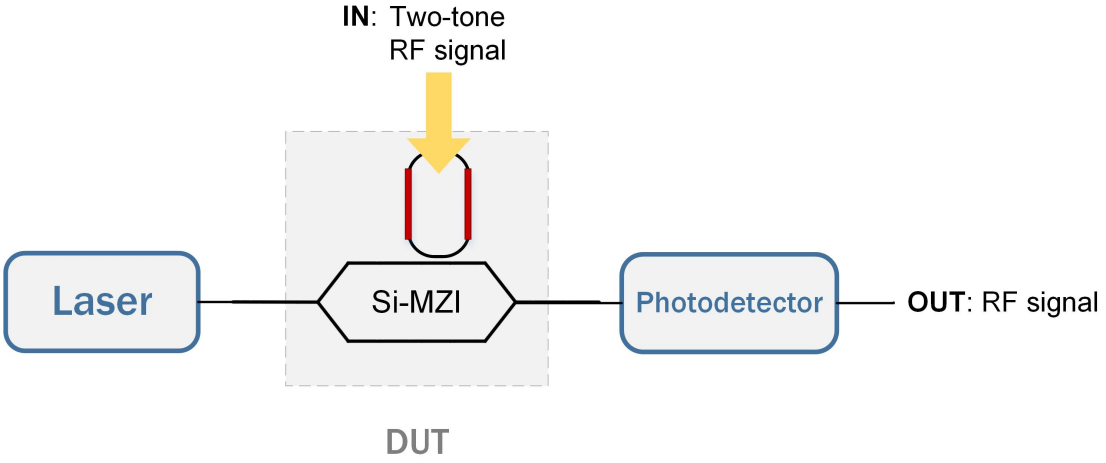

FIGURE 5.15: Block diagram of the simulated SFDR measurement scheme.

TABLE 5.5: **Link Parameters**

Property	Value
Laser Power	15 dBm
I/O Grating Couplers Loss	9 dB
Photodetector Responsivity	0.7 A/W
Modulator and Photodetector Impedance	50 Ω
RAMZI Waveguide loss	0.5 dB/mm
RAMZI Doped Waveguide loss	2 dB/mm
RAMZI MZI arm length	400 μm
RAMZI Ring circumference	286 μm
RAMZI Mode effective refractive index	2.5434

The simulated system used typical specifications for optical components that are commercially available. The parameters of this optical link are stated in Table 5.5. The RF input to the system was a sum of two time-domain sinusoidal signals (f_1 = 10 GHz, f_2 = 10.01 GHz) and its optical output was calculated sequentially for each sampling point in the time domain. It is noted that this sequential analysis assumes every time instance

of the system to be in a steady state, therefore the modulators can be represented with the transfer functions in equations (5.6) and (5.7) at every point in time. It is also noted that the physical mechanisms of electro-refraction (plasma dispersion effect in the p-n junction) were not simulated. Thus, the junction-related bandwidth limitation of the modulator was not considered in this model and a linear relation between input voltage V and n_{eff} was assumed.

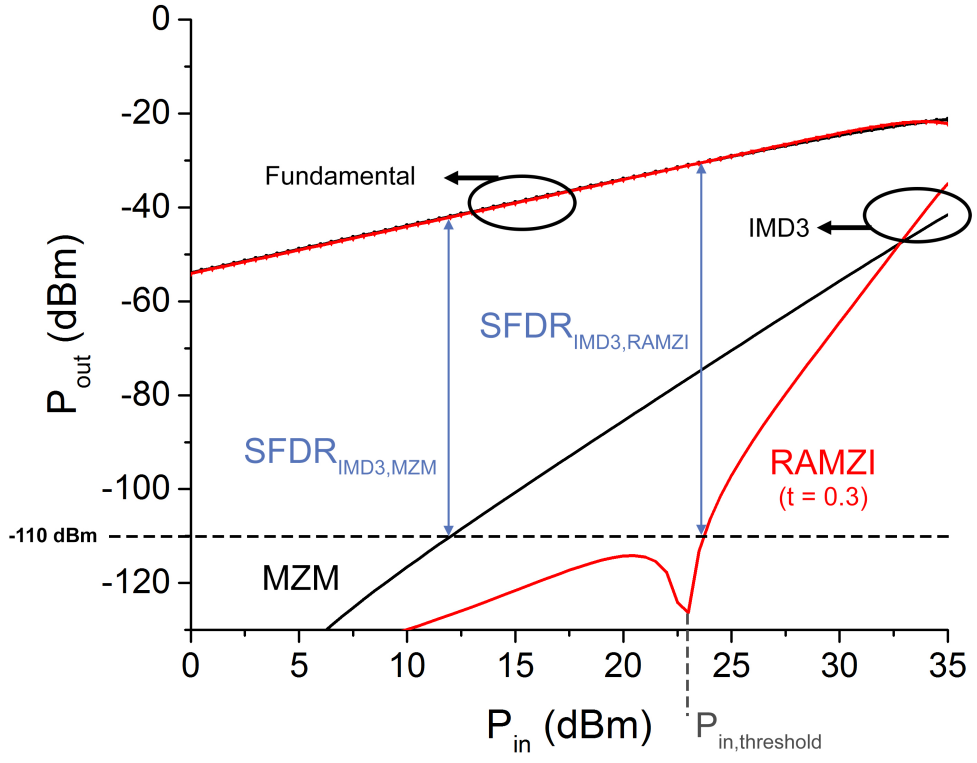

FIGURE 5.16: P_{in}-P_{out} plots for a conventional Mach–Zehnder modulator and a RAMZI modulator.

To calculate the $SFDR_{IMD3}$, the relation of input to output power for the fundamental modulating tones (f_1, f_2) and the 3rd-order intermodulation distortion (IMD3) tones ($2f_1 - f_2$, $2f_2 - f_1$) was investigated. A range of electrical input power values were fed to the system, to form the plot shown in Fig. 5.16. It can be observed that the output power of the fundamental tone shows a linear trend with a slope of 1, while the IMD3 tone shows different slopes in different input power regimes: for lower input power the trend appears linear with a slope value of 2, whereas at higher input power, a slope value of 6 is observed. The transition between the two regimes occurs after a certain P_{in} threshold and manifests itself in the graph as a dip in power. This trend is compared with the one for a conventional MZM topology, where the length of the MZI arms was set so that the power of the generated fundamental tones for the two topologies are equal. The IMD3 power plot in the MZM case follows a linear trend with a slope value of 3, as expected by the strong 3rd-order-term present in the MZI transfer function. The

comparison shows the effect the coupled ring has on the MZI, as when the 3rd-order term is eliminated, other nonlinear terms take prominence in shaping the power variation at the IMD3 frequency, hence the power slope changes from a value of 3 to some higher value. The advantage of using the RAMZI topology is then evident by comparing the SFDRs of the plots for the two configurations (MZM and RAMZI). For a noise level set at -110 dBm (determined by the limitations of the FFT used for the calculation), the $SFDR_{IMD3}$ for the MZM is 68.6 dB, while the $SFDR_{IMD3}$ for the RAMZI modulator is equal to 80.1 dB. A visual representation of the RAMZI linear response compared to the MZM can be seen in Fig. 5.17, where the optical output power P_{out} is plotted with relation to induced refractive index change Δn_{eff}.

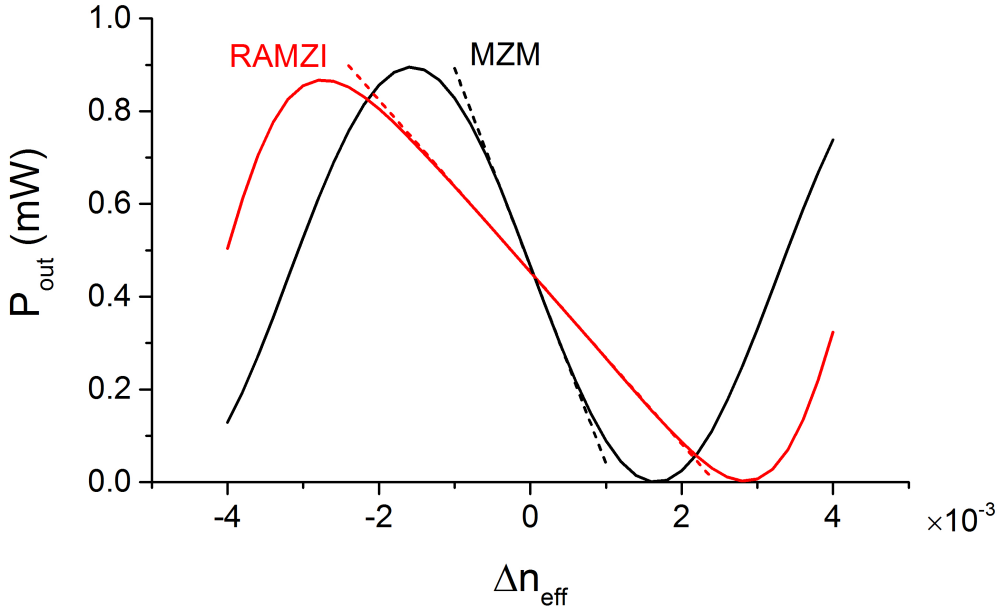

FIGURE 5.17: Optical Output P_{out} vs. effective refractive index change Δn_{eff} plots for a RAMZI modulator and a MZM.

In order to determine the impact of the RR-to-MZI power coupling ratio on the SFDR of the RAMZI modulator, the previous study was repeated for different coupling coefficients t and the SFDR was calculated for each case. Figure 5.18 illustrates the SFDR trend and reveals an optimum t coefficient ($t = 0.3$), for which the SFDR value is at a maximum. For the t values investigated (0.2 to 0.4), a SFDR improvement of up to 11.8 dB is observed for the optimum RAMZI design. To gain some meaningful insight about this variation, Fig. 5.19 depicts how the IMD3 power changes with respect to the input power for the three different cases of $t = 0.2$, 0.3 and 0.4. Modifying the RR-to-MZI coupling value shifts the power dip point along the horizontal axis, thus altering the position of the two slope regimes and the intersection point of the IMD3 plot with the noise level. For t values away from 0.3, the slope takes values which are close to 3 around the noise level, limiting the available SFDR. This shows the significance in providing a degree of freedom for the RR-to-MZI coupling ratio, as the ability to tune the t coefficient allows for fine-tuning of the linearity behaviour of the modulator.

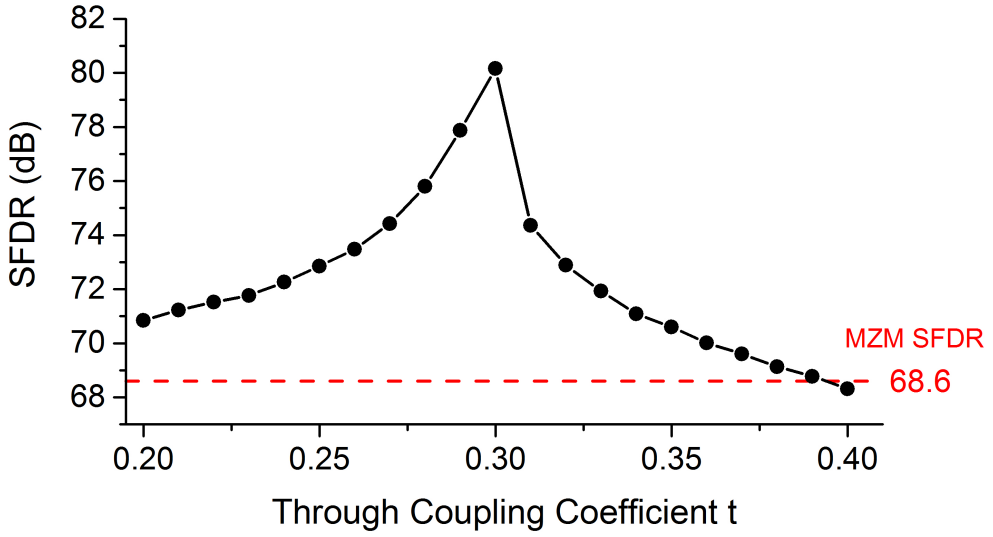

FIGURE 5.18: $SFDR_{IMD3}$ value for RAMZI modulators with different RR-to-MZI coupling coefficients.

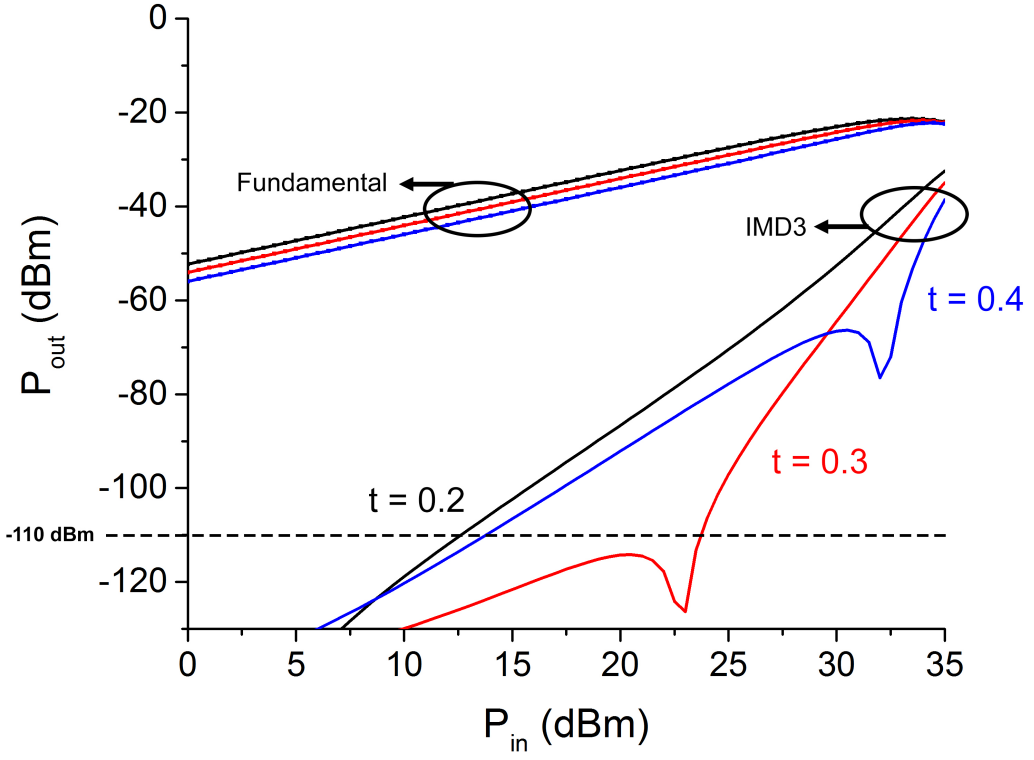

FIGURE 5.19: P_{in}-P_{out} plots for three RAMZI modulator configurations with $t = 0.2$, 0.3, 0.4.

The optimum value for the t coefficient corresponds to a specific value for the coupling gap between the MZI arm and the RR. In particular, the power coupling ratio for the $t = 0.3$ case is equal to $\kappa^2 = 1 - t^2 = 0.91$, which means that strong coupling is required between the two components. Since the smallest achievable gap between two waveguides is often limited by fabrication constraints, additional configurations were studied to provide alternatives for linear modulator design. Further analysis was conducted for the cases of two-ring and three-ring RAMZI topologies, illustrated in Fig. 5.20. In the case of the two-ring structures, two implementations are considered, which analytically yield the same SFDR results: the push-pull configuration (Fig. 5.20 (a)) and the parallel-coupled-ring configuration (Fig. 5.20 (b)). The SFDR trend with relation to t is shown in Fig. 5.21 when two and three rings are used. They show that the position of the maximum SFDR value in the t axis is shifted, with $t = 0.53$ and $t = 0.66$ being the optimum values for the two-ring and three-ring configurations respectively. These results suggest that weaker MZI-to-RR coupling is required for each ring to achieve the same effect ($\kappa^2 = 0.72$ and $\kappa^2 = 0.56$ respectively), thus relaxing the gap fabrication requirements for waveguide-to-waveguide coupling.

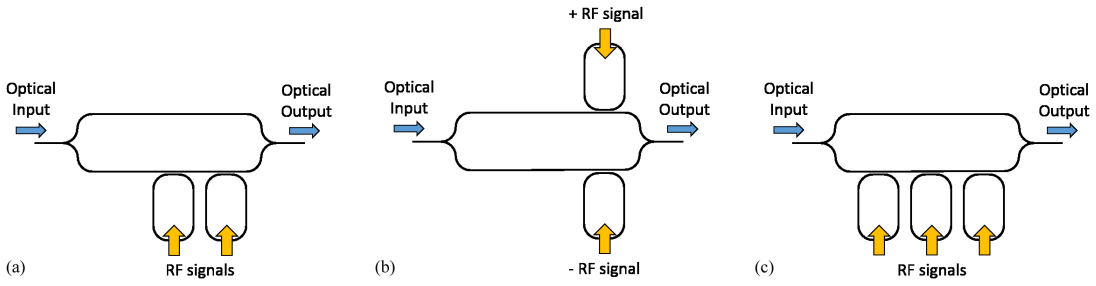

FIGURE 5.20: Schematics of multi-ring RAMZI configurations.

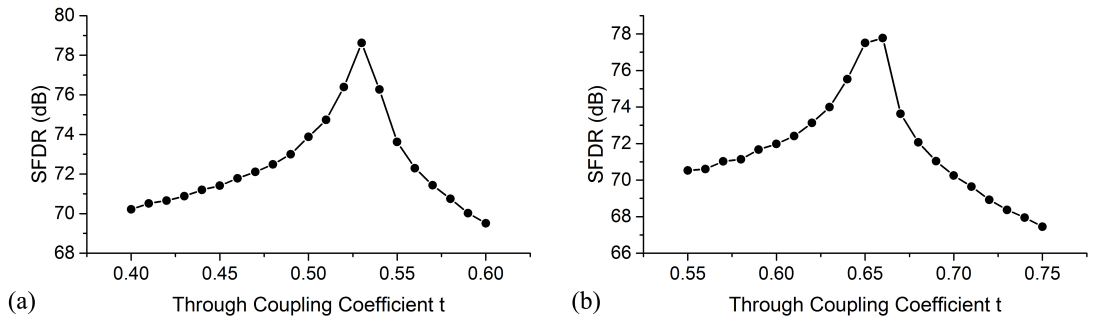

FIGURE 5.21: SFDR with relation to t coupling coefficient for (a) two-ring and (b) three-ring RAMZI configurations.

Finally, the layout design of the aforementioned topologies was drawn by corresponding the power coupling ratios to waveguide gaps. A campaign of FDTD simulations of the structure illustrated in Fig. 5.22 (a) were run to sweep the t parameter and produce the plot in Fig. 5.22 (b), showing the relation of the power coupling ratio κ^2 to the gap size. The waveguide width was set to 450 nm and the coupling length was selected to be 10 μm, so that the gaps corresponding to the desired coupling ratios are feasible

with the available fabrication facilities. With the information from the plot in Fig. 5.22 (b), the selected gaps for the single-ring, the two-ring and the three-ring configurations for the RAMZI modulator were 310, 350, 389 nm respectively. Metallic heaters were additionally designed to be placed on top of the coupling region in order to provide tunability for the coupling ratio and therefore the modulator linearity by means of a variable applied voltage.

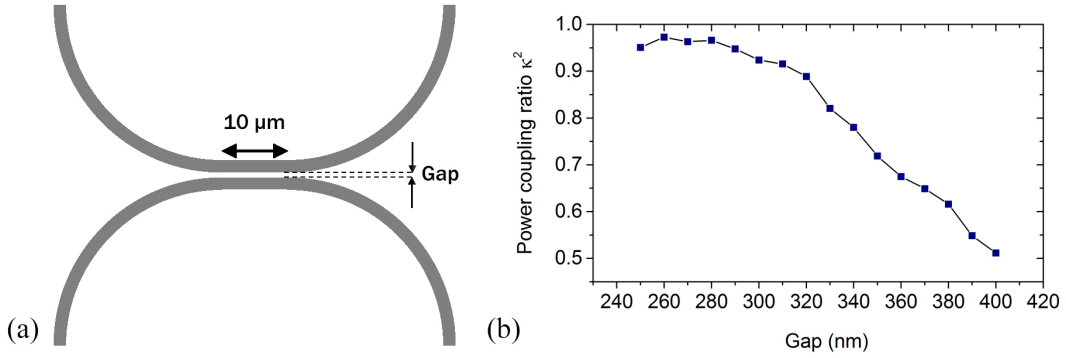

FIGURE 5.22: (a) Top view sketch of the coupling section between two waveguides, (b) Power coupling ratio with relation to coupling gap.

5.3.3 Fabricated RAMZI modulators

A set of tunable RAMZI modulators were fabricated in the facilities of the Optoelectronics Research Centre and the University of Surrey. The device designs that were submitted for fabrication were based on the analysis of the previous section, where the focus was on achieving the optimum coupling ratio and enabling its tunability. As a result, the design layouts consisted of modulators with the optimum RR-to-MZI coupling, along with a number of variations of the RR-to-MZI coupling gap. However, due to complications in the fabrication procedure, not all of the final devices were available for characterisation as some of the interface grating couplers were damaged during the process. The long processes of manufacturing the silicon photonic chips did not allow for a second fabrication round within the duration of this PhD project. Therefore, in this section, selected results are reported for the RAMZI modulator device that demonstrated the highest SFDR value.

The fabricated RAMZI modulator that was tested contained a single ring resonator and is described by the specifications listed in Table 5.6 and a top view microscope image of the SOI device is shown in Fig. 5.23. The setup illustrated in Fig. 5.24 was constructed to characterise the modulator in terms of its linearity. Two frequency-locked RF synthesisers were set to drive the modulator with two frequencies $f_1 = 2$ GHz and $f_2 = 2.01$ GHz. These signals, coupled with a DC bias voltage, were sent to the RAMZI metallic pads through a GSG high-speed probe, while two control voltages were used to tune the RAMZI through two heater structures: one positioned on a layer above the

TABLE 5.6: **Fabricated RAMZI modulator specifications**

Silicon layer thickness	220 nm
Waveguide fabrication procedure	E-beam lithography & Inductively Coupled Plasma etching
Waveguide type	Rib, etching depth 120 nm
Rib waveguide width	450 nm
Doped waveguide p-type carrier concentration (boron ion implantation)	3×10^{17}
Doped waveguide n-type concentration (phosphorus ion implantation)	1.5×10^{18}
MZI arm total length	837 μm
Racetrack Circumference	310 μm
Coupling gap	295 nm
Metallic electrodes material	Stack of Ti/TiN/Al/Ti/TiN

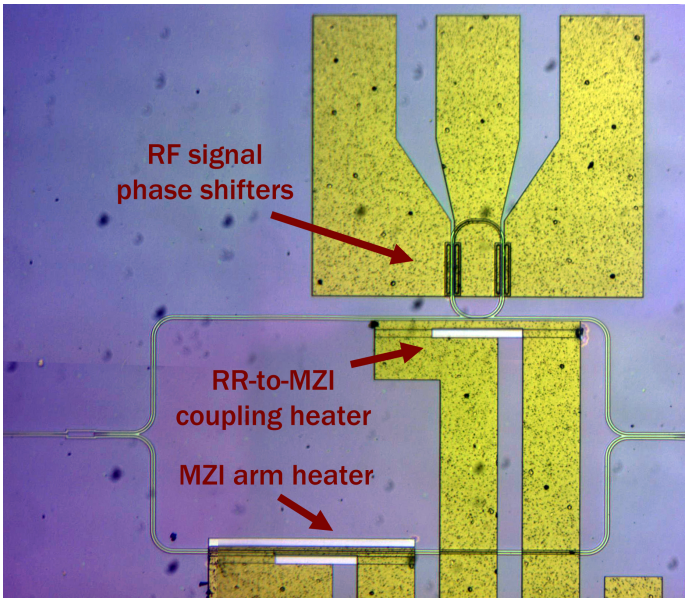

FIGURE 5.23: Top view microscope image of the fabricated RAMZI modulator.

RR-to-MZI coupling area, and one positioned above the uncoupled MZI arm (Fig. 5.23). These two heaters were driven through DC electrical probes and their respective roles in the device operation were to tune the t coupling coefficient and bias the MZI to its quadrature point. The optical carrier was fed to the modulator by a tunable-wavelength laser source, at a power of 14 dBm. The tunability in wavelength enabled the RAMZI to be driven at the off-resonance point of the ring resonator. The total loss of the silicon photonic device (grating couplers + waveguide losses) amounted to 15 dB. The output of the device was sent to a linear photodetector with a responsivity of 0.65 A/W, which was connected to an electrical Spectrum Analyser. Thus, the power of the tones at $2f_1 - f_2$, f_1, f_2, $2f_2 - f_1$ could be monitored and measured. It is also noted that the noise in the implemented link originated primarily by the Relative Intensity Noise (RIN) of the laser source which was equal to -177 dBm at the detection stage.

The SFDR of the modulator was measured for different voltages applied to the coupling

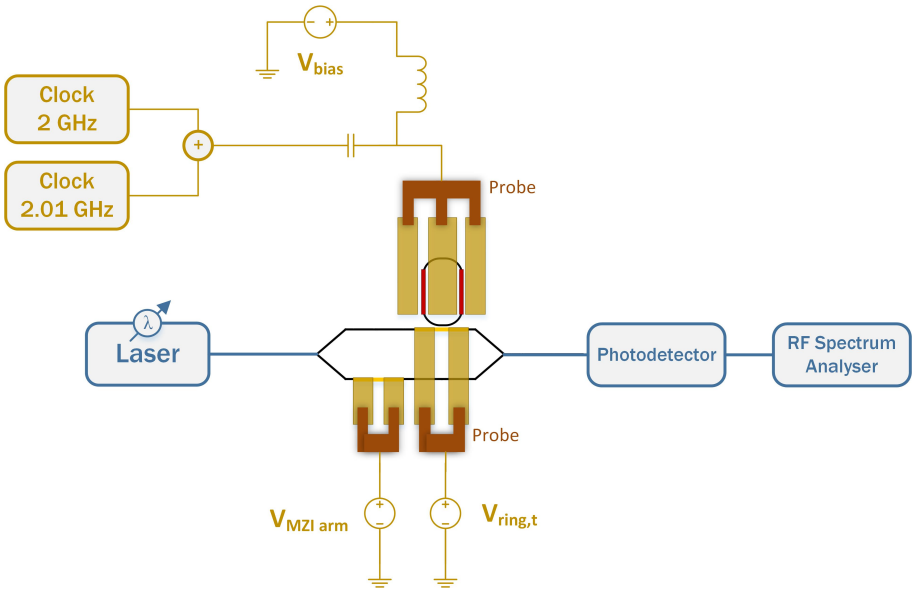

FIGURE 5.24: SFDR measurement setup for the linearity characterisation of the RAMZI modulator.

section heater. In terms of the measurement methodology, it was crucial to ensure that the modulator was operated at both the off-resonance point of the ring and the quadrature (3-dB) point of the MZI. For this reason, the optical wavelength and the MZI arm heater had to also be appropriately tuned for each measurement in the coupling section heater voltage sweep. The results of this measurement are shown in Fig. 5.25. The SFDR values are in the range of 88-89 dB. These values were expected to be higher, considering the linearity measurement results of the silicon MZM in Section 5.1 which was part of a similar link (SFDR ∼101 dBHz$^{2/3}$). However, the RAMZI device that was available for measurement did not correspond to the ideal design, but was instead a sub-optimal variation, with a coupling section that corresponded to a different t parameter than the optimum one. It should also be noted that these SFDR values are slightly higher than the ones calculated through simulations (Fig. 5.18), because the link implementation in the experiment differed from the simulated link in terms of noise power level.

The observed change in linearity was only minor (∼0.7 dB), which was attributed to an insufficient coupling ratio change induced by the heater. The design of the metallic filament used for the heater would need to be improved in order to induce a non-uniform temperature change to the coupling area and cause the refractive indices of the two coupled waveguides to be different from each other.

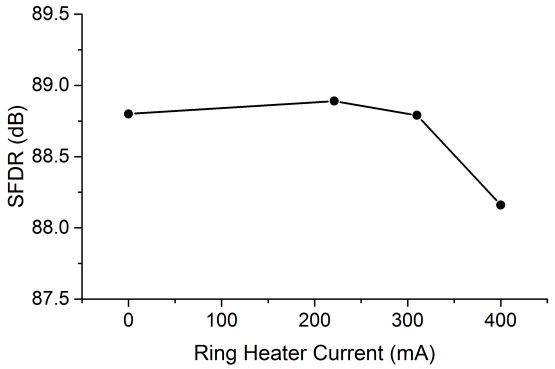

FIGURE 5.25: Fabricated RAMZI SFDR with relation to the current applied to the coupling section heater.

5.4 Conclusion

This chapter focused on the use of MZI-based silicon modulators for the implementation of advanced modulation formats (PAM-4, DMT), with an emphasis on investigating their linearity behaviour. The first two sections reported the characterisation of an electrically packaged Mach–Zehnder Modulator and its implementation on an IM-DD link using PAM-4- and DMT-modulated data. The results showed the reliable transmission (BER below FEC) of PAM-4 data at 40 Gb/s over 20 km of SMF and of DMT data at 49.6 Gb/s over 40 km of SMF, as a result of the highly linear behaviour of the MZM. The DMT transmission showed a spectral efficiency of 5 b/s/Hz, which is the highest value reported for a conventional silicon photonic IM-DD system. The third section focused on methods to improve the linearity of MZI-based modulators while also offering tunability for the linearity behaviour, by investigating the design of a Ring-Assisted Mach-Zehnder Interferometer (RAMZI) configuration. Modelling of the RAMZI modulator showed an increase in its SFDR parameter in excess of 10 dB compared to a conventional MZM of the same modulation depth. Specifications and comments on the design of such RAMZI devices on the SOI platform were reported, while preliminary characterisation results of fabricated devices were presented.

Chapter 6

All-Optical Wavelength Conversion based on Nonlinear Waveguides

Modulation formats that handle complex optical signals such as the variations of Quadrature Amplitude Modulation (QAM) have been under investigation in the research literature on coherent systems over the past years [160]. The adoption of such formats facilitate an increase in the capacity of optical networks and help alleviate a potential "capacity crunch" [83]. Even though the main role of an optical communication system is to transmit these signals in order to transport information, a significant part of the optical networks also includes processing functionalities such as wavelength conversion, which are currently performed in the electrical domain. Silicon photonics can play an increasingly important role in this signal processing sector, enabling the production of all-optical commercial devices, capable of performing a multitude of operations in WDM environments [16, 17, 161, 162].

All-optical processing concerns the techniques implemented in order to manipulate data entirely in the optical domain, rather than transferring it to the electrical domain for processing. The advantages offered by all-optical solutions relate to the ability of handling data at ultra-fast rates (> 500 Gbs^{-1}) [163, 164], which is not possible by the electronic processing alternative. Of course, another important parameter to consider when attempting to compare the two technologies is power consumption and, currently, implementing signal processing through all-optical techniques appears to show a tradeoff between achievable throughput and power consumption [165].

Wavelength conversion is one such optical functionality that enables switching or copying ofa data stream to a different carrier wavelength. The significance of such an operation is clear in the cases of wavelength contention, while switching between wavelengths is also essential when constructing systems that are required to be reconfigurable [166].

Being an all-optical process, wavelength conversion is implemented in optical media by exploiting their nonlinearity. One such application is the use of nonlinear silicon components that utilise the Kerr effect inherent in silicon to trigger Four-Wave Mixing (FWM) and produce new wavelengths. Thus, wavelength conversion of 16- and 64-QAM signals has been previously reported in silicon-based waveguides designed as strip structures [167, 168]. On the other hand, rib-type structures are appealing in applications that require dispersion-tailored devices, with low propagation loss and low polarisation rotation, because this particular geometry exhibits comparatively lower sensitivity to fabrication imperfections [16, 169]. Therefore, to leverage the advantages of this particular geometry, this chapter focuses on investigating rib-type silicon waveguides as building blocks in the design of integrated wavelength converter devices compatible with links that use QAM-modulated data. The first and second sections report the characterisation of a fabricated silicon rib waveguide in terms of its nonlinear properties and the experimental results of a wavelength conversion operation performed on a 16-QAM optical signal. The third section describes the procedure followed to design a fully integrated wavelength converter that suppresses the original signal and the optical pump at the output stage, through the use of appropriately tailored ring filters.

6.1 Waveguide Design and Characterisation

The silicon waveguide that was used in the following experiments was designed and fabricated at the Wuhan National Laboratory for Optoelectronics, in Huazhong University of Science and Technology in China. The characterisation and wavelength conversion experiments were performed at the Optoelectronics Research Centre, in the University of Southampton by the author with the help of Dr. Cosimo Lacava.

The waveguide used as the nonlinear component was drawn on a Silicon-on-Insulator (SOI) wafer with a 220-nm-thick silicon layer. The cross-section of the fabricated structure is illustrated in Fig. 6.1. The layout was written on the silicon layer by means of Deep Ultraviolet (DUV) 248-nm lithography and the selected etching depth for the rib-type structures was 70 nm. The width of the waveguide was 500 nm in order to maintain single-mode operation in the fundamental Transverse Electric (TE) mode and its length was selected to be 4 cm so that the net nonlinear effect across its total length was strong. It is noted that the silicon structures were surrounded by SiO_2, as the bottom consisted of a buried oxide layer, while the top of the layout was covered with a SiO_2 cladding layer. Grating couplers served as the input and output of the waveguide and they were designed to couple TE-polarised light in the C-band. The propagation loss of the waveguide along with the insertion loss of the grating couplers were measured through an effective cutback technique performed on different-length variations of this waveguide that were written on the SOI wafer. The propagation loss was measured to

be $\alpha = 2.5$ dB/cm and the insertion loss corresponding to a pair of grating couplers was 8 dB.

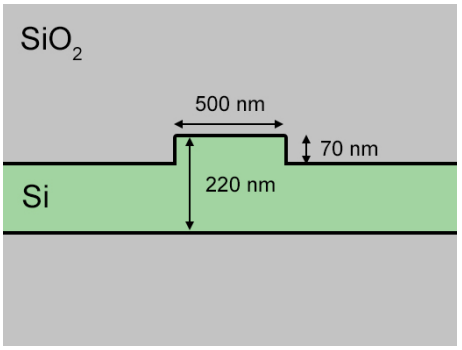

FIGURE 6.1: Cross-section of the Si- rib waveguide used as the nonlinear component.

The characterisation of the nonlinear properties of the waveguide essentially aimed to evaluate the real part of its nonlinear coefficient $Re[\gamma]$ which ultimately determines the strength of the Four-Wave Mixing effect used for the wavelength conversion application. Therefore, the characterisation experiment involved inducing FWM by launching two Continuous Wave (CW) optical beams at closely-spaced wavelengths, namely the pump and the signal beam, to produce light at a third wavelength, called the idler beam, as a result of intermodulation between the two optical inputs. This effect can be described by the following equation [170]

$$\frac{P_i(L)}{P_s(L)} = \left(\eta \cdot P_p(0) \cdot Re[\gamma] \cdot L_{eff}\right)^2 \tag{6.1}$$

which is an approximation of the full mathematical formulation describing Four-Wave Mixing [171], applicable to cases where the two-photon absorption (TPA) effect can be considered negligible and the signal power level is kept significantly lower than the pump power level. In this equation, $\frac{P_i(L)}{P_s(L)}$ represents the power ratio between the signal and idler wavelengths measured at the output of a waveguide of length L, η is a coefficient related to the phase mismatch caused by chromatic dispersion, $P_p(0)$ is the pump power launched at the input of the nonlinear waveguide, $Re[\gamma]$ is the nonlinear coefficient that is dependent on the material and the geometry of a given waveguide, and L_{eff} represents the effective length of the nonlinear waveguide, given by the formula:

$$L_{eff} = \frac{1 - e^{-\alpha L}}{\alpha} \tag{6.2}$$

where L is the length of the waveguide and α is its power loss coefficient.

In order to quantify $Re[\gamma]$, the set-up illustrated in Fig. 6.2 was constructed. Two external cavity lasers (ECLs) were set to provide the CW pump and signal beams at wavelengths of 1557 nm and 1556.6 nm respectively. In order to provide sufficient power

to trigger the nonlinear effect of the waveguide, the pump beam was first amplified by an Erbium-Doped Fibre Amplifier (EDFA). Coupling to the long serpentine waveguide was implemented through optical fibres that were positioned at a 6° angle above the input and output grating couplers, while polarisation controllers placed after the optical sources helped ensure that only TE-polarised light was launched to the chip. The power of the signal beam was kept constant at $P_s = 0.35$ dBm, while the pump power P_p was varied in order to observe the change in the signal-to-idler power ratio $\frac{P_i}{P_s}$ at the output. This ratio, which expresses the conversion efficiency of the FWM effect, was evaluated through spectral measurements at the device output by means of an Optical Spectrum Analyser (OSA).

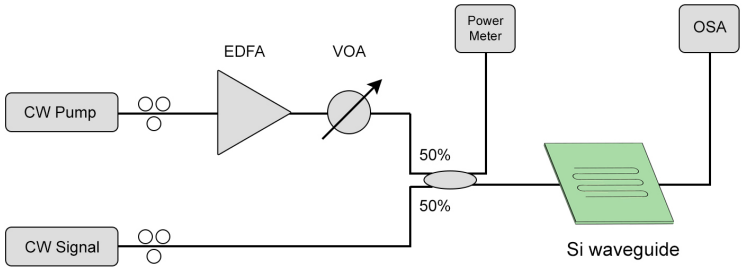

FIGURE 6.2: Experimental setup for the characterisation of the nonlinear waveguide.

The quadratic formula (6.1) was fitted to the measured data in order to evaluate the parameter $Re[\gamma]$. It is noted that for the selected wavelength spacing, η was assumed to be 1 because the effect of dispersion is negligible. The measured conversion efficiency $\frac{P_i}{P_s}$ with respect to input pump power P_p is plotted in Fig. 6.3 along with its fitted model and the extracted value of the nonlinear coefficient was calculated to be $Re[\gamma] = 45 \pm 1$ W^{-1}m^{-1}.

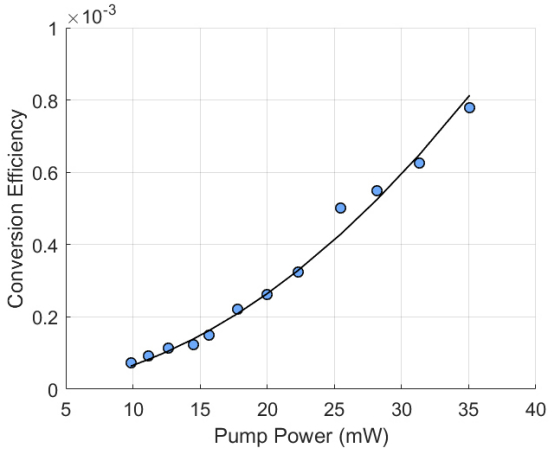

FIGURE 6.3: Fitting of measured data based on equation (6.1).

6.2 FWM-based Wavelength Conversion of 16-QAM signals

The wavelength conversion experiment involved setting up the transmission system shown in Fig. 6.4. In this experiment, the optical carrier was modulated by a 16-QAM signal at a 10-Gbaud rate by means of a Dual-Nested Mach–Zehnder I-Q Modulator. The signal was generated by an Arbitrary Waveform Generator (AWG) which converted a $(2^{15} - 1)$-long pseudorandom binary sequence (PRBS) to a 16-QAM electrical signal fed to the modulator. Both pump and signal beams were amplified by EDFAs in order to achieve a sufficiently high power level on the waveguide, as well as to compensate for the modulator insertion loss. The two optical inputs were coupled to the silicon chip and the converted signal at the idler wavelength was observed at the output on an OSA. The recorded spectrum for the maximum conversion efficiency achieved in this experiment is shown in Fig. 6.5, where an estimated level of 18.5 dBm of pump power was coupled to the waveguide structure (after the input grating coupler) and a conversion efficiency of -16 dB was measured. The selected pump and signal wavelengths were 1557.26 nm and 1555.90 nm respectively, while the idler wavelength was 1558.62 nm. It is noted that no two-photon absorption (TPA) was observed at this level of input power, however the limitation to the pump intensity was set by the damage caused to the input grating coupler at incident powers higher than ∼25 dBm.

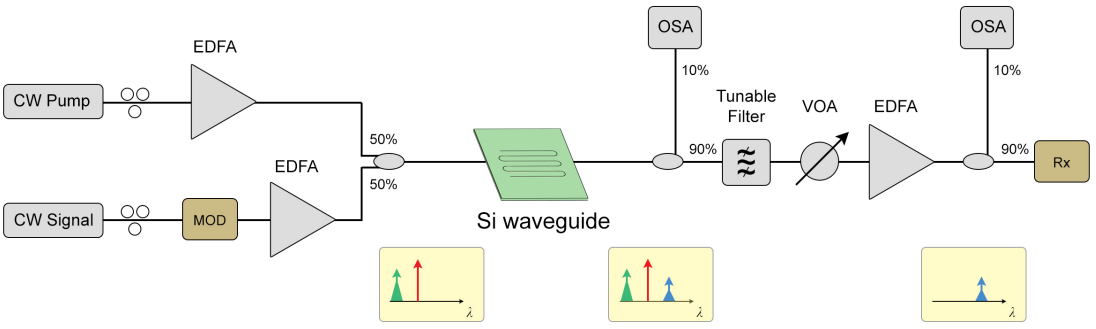

FIGURE 6.4: Optical setup for the wavelength conversion experiment.

To evaluate the Bit Error Ratio (BER) of the converted signal, the idler was first isolated from all other frequencies and then sent to a coherent receiver. Therefore, a tunable optical filter with a 3-dB bandwidth of 50 GHz was used after the chip output and the filtered idler was subsequently amplified to be retrieved by a coherent receiver and an Optical Modulation Analyser (OMA). The OMA consisted of a real-time scope that performed BER calculations on the received 16-QAM data. A Variable Optical Attenuator (VOA) was used to vary the Optical Signal to Noise Ratio (OSNR) of the received signal and record the corresponding changes in BER. The performance of the wavelength converter is presented in Fig. 6.6 through a comparison of the BER vs. OSNR plots for the original (back-to-back) signal and the converted signal. The inset constellation plots

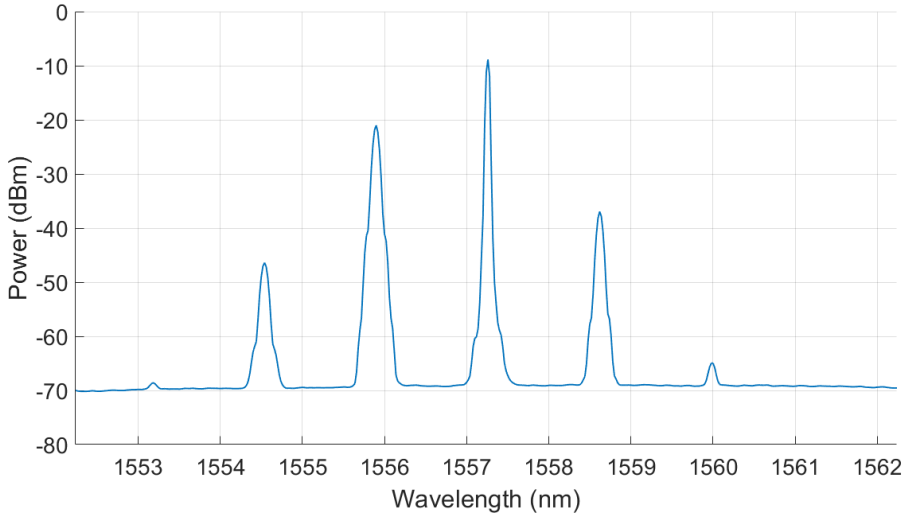

FIGURE 6.5: Spectrum at the Si waveguide output containing the pump, signal and idler, as well as higher-order frequency components generated by Four-Wave Mixing.

portray the quality of the two 16-QAM signals at an OSNR of ∼24 dB, indicating very low degradation for the converted symbols. The curves resulting from a linear fitting of the measured data points suggest that an OSNR penalty of 1.4 dB is incurred during the wavelength conversion process. Given that the back-to-back measurement was conducted with the same Filter-VOA-EDFA arrangement at the receiver side, the only additional source of noise that introduces the OSNR penalty in the wavelength conversion system is the added pump source along with its corresponding EDFA. Therefore, the penalty can be attributed to the amplified spontaneous emission (ASE) of the EDFA used at the input stage of the system.

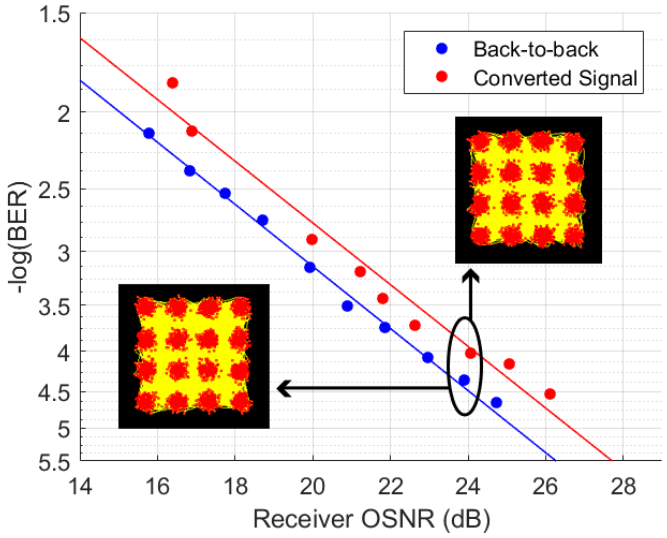

FIGURE 6.6: BER vs. OSNR comparison for the back-to-back and the converted signal.

6.3 Design of an Integrated Silicon Wavelength Converter

As can be seen from Fig. 6.4 and 6.5, the role of the nonlinear waveguide in the FWM-based wavelength conversion operation is the generation of a copy of the signal at the idler wavelength. Any mechanism for removing the original signal and pump beams from the output will have to be added as a bulk component outside the chip (Fig. 6.7 (a)). In the context of a telecommunications system, the design requirements for a wavelength converter usually dictate that the device output contains the optical signal only at the new wavelength. Under this consideration, the design of an integrated device that can perform the conversion operation in the form shown in the schematic in Fig. 6.7 (b) entirely on-chip was investigated.

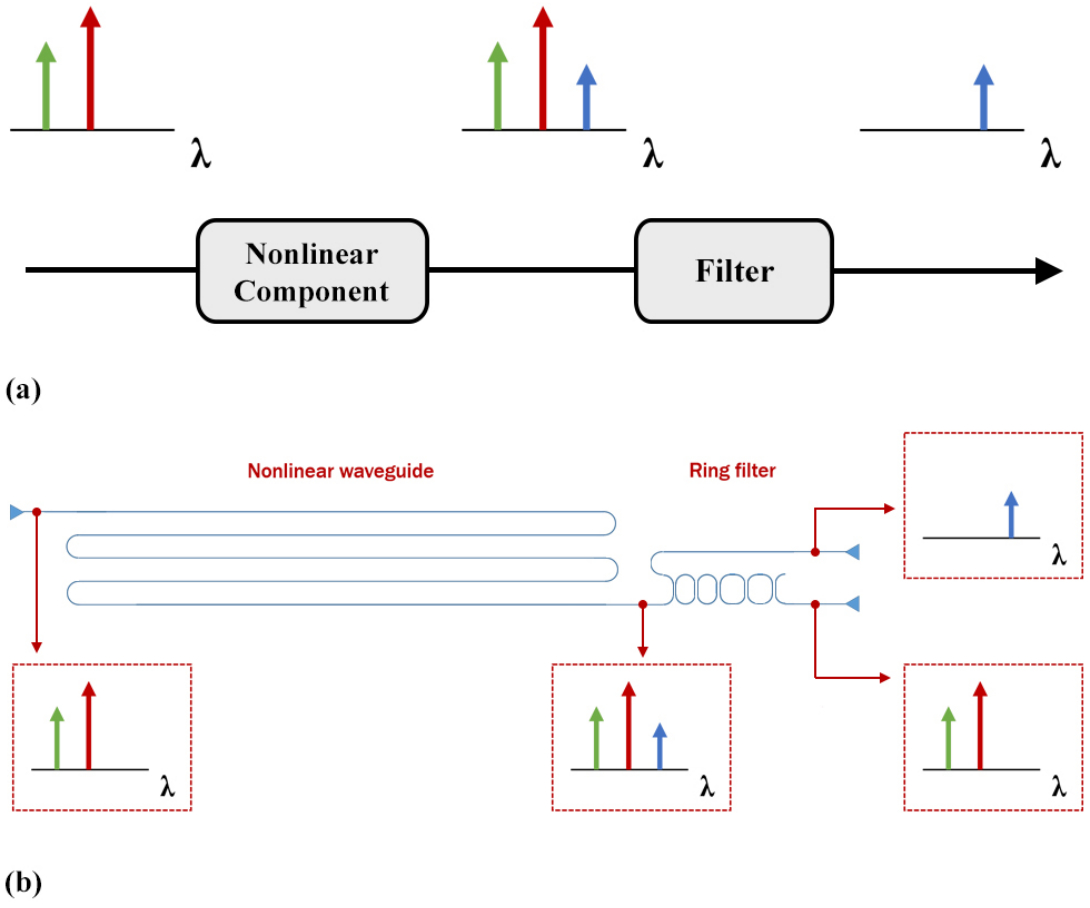

FIGURE 6.7: (a) Block diagram of the integrated wavelength converter and (b) schematic representation of its silicon photonic implementation (ring dimensions not to scale).

The design of this device was based on the concept implemented in Section 6.2, where a bandpass filter was used to selectively allow light to propagate only at the idler wavelength. Therefore, the silicon photonic version of this device involved the design and

cascaded connection of two fundamental building blocks: the nonlinear waveguide and the optical bandpass filter. The requirements for the two components were identified and solutions were proposed by developing a photonic circuit layout for fabrication at the facilities of the Optoelectronics Research Centre (ORC) and the University of Surrey through the CORNERSTONE project [172]. Although the fabrication of the devices was not completed within the time constraints of this doctoral programme, the design procedure and the proposed component specifications are presented in this section.

6.3.1 Nonlinear p-i-n Waveguide for Carrier Extraction

The first component of the integrated wavelength converter shown in Fig. 6.7 (b) is the nonlinear waveguide which is used to generate the idler. The target of the design process for this component is the maximisation of the conversion efficiency. Although the important parameters that determine the conversion efficiency of the FWM phenomenon are present on the right hand side of equation (6.1), increasing the optical power pumped into a silicon waveguide reveals another important factor that limits the FWM process, which is the Two-Photon Absorption (TPA) effect. This is expressed by the imaginary part of the nonlinear coefficient ($Im(\gamma)$). TPA additionally generates free carriers, which in turn causes Free Carrier Dispersion (FCD) and Free Carrier Absorption (FCA). All the absorption effects are detrimental to the FWM process and set an upper threshold to the conversion efficiency.

Based on these considerations, the design of the nonlinear component aimed to maximise the achievable conversion efficiency by mitigating the absorption effects. The technique used for this purpose was the creation of a p-i-n junction in the cross section of the waveguide so that the generated free carriers can be extracted by applying voltage to the junction. This technique has been previously reported in the literature for similar applications [173, 174] as well as for the demonstration of optical gain through Stimulated Raman Scattering in silicon [175, 176].

The silicon photonic chip fabrication processes provided by CORNERSTONE offered the capability of ion implantation to create doped waveguides, therefore the structure shown in Fig. 6.8 was designed. The photonic layout was written for fabrication on a SOI wafer with a 220-nm-thick silicon layer. The designed waveguide was selected to be a rib type to incorporate the doped sections. The etching depth was set to be 120 nm according to the CORNERSTONE project specifications, while the width of the waveguide was set as 500 nm to allow for single-mode operation in the Transverse Electric (TE) mode. The p- and n-doped regions were placed at varying distances across different instances of the device written in the layout, in order to evaluate the optimum spacing configuration experimentally. It is noted that close proximity of the doped section to the optical mode can result in a stronger carrier extraction effect in the presence of high optical power, however it can also introduce losses related to the presence of charge carriers in the p-

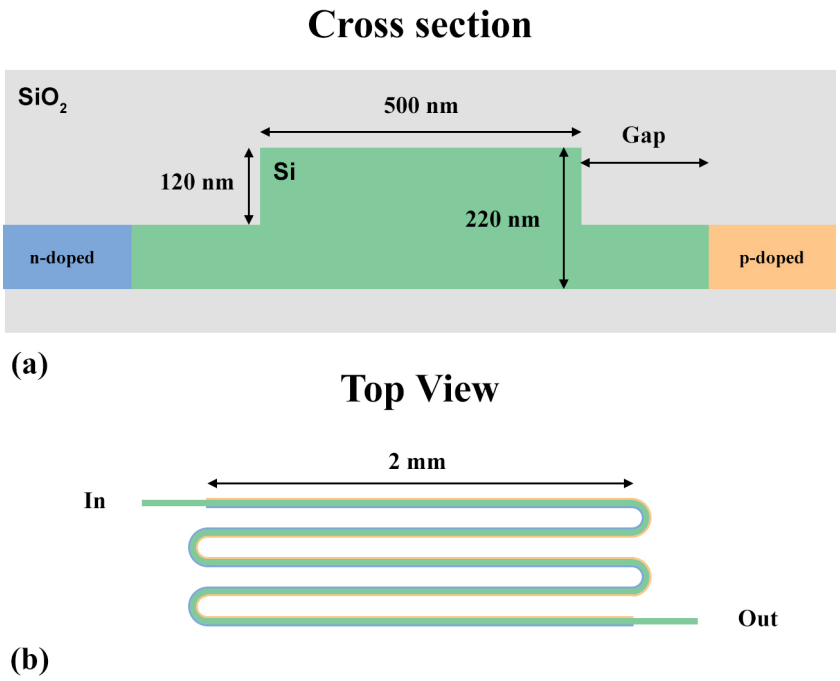

FIGURE 6.8: (a) Cross section of the p-i-n waveguide designed for free carrier extraction, (b) Top view of the full length of the waveguide written in a serpentine shape.

and n-doped areas. The presence of loss reduces the conversion efficiency, as it appears in eq. (6.1) in the form of the L_{eff} parameter, therefore a trade-off between loss and the strength of the carrier extraction mechanism is encountered. The aim of the design was to investigate the combined effects of the gap in Fig. 6.8 (a) and the length L of the waveguide on the conversion efficiency by including a number of device variations in the same layout. The top view of an example device is illustrated in Fig. 6.8 (b), where the length L is approximately 10 mm. The different values for the gap and length parameters that were included in the layout are outlined in Table 6.1.

TABLE 6.1: **Parameter variations for the doped nonlinear waveguide**

Parameter	Values
Gap	200 nm, 400 nm, 800 nm, 1600 nm, 2200 nm
L	10 mm, 18 mm, 34 mm

6.3.2 Ring Resonator Filter

The second component of the integrated wavelength converter is the filter used to isolate the idler. The selected integrated implementation for this filter was a ring resonator structure and the design targets were related to (a) its wavelength tunability, (b) its bandwidth and (c) its Free-Spectral Range (FSR). A ring filter can be tuned in wavelength by means of appropriate heaters, while its bandwidth is dependent on the coupling condition of the ring resonator which can be determined by the geometry of the structure. The challenging requirement for this application was the large FSR that the filter

must exhibit in order for the wavelength converter to be functional across the C-band. It is also noted that a drop filter (bandpass type) was selected as the preferred type, so that the light entering the ring resonator would be the converted signal at the idler wavelength, while the pump and original signal would be out of resonance with the ring cavity. On the contrary, a through filter (bandstop type) would require the idler to be placed at an off-resonance wavelength and therefore pass through the bus waveguide of the structure, while the high-power pump would enter the resonant cavity to be filtered out. However, the presence of the high-power pump inside the ring could significantly detune it due to the nonlinear effects present in it and was therefore not preferred.

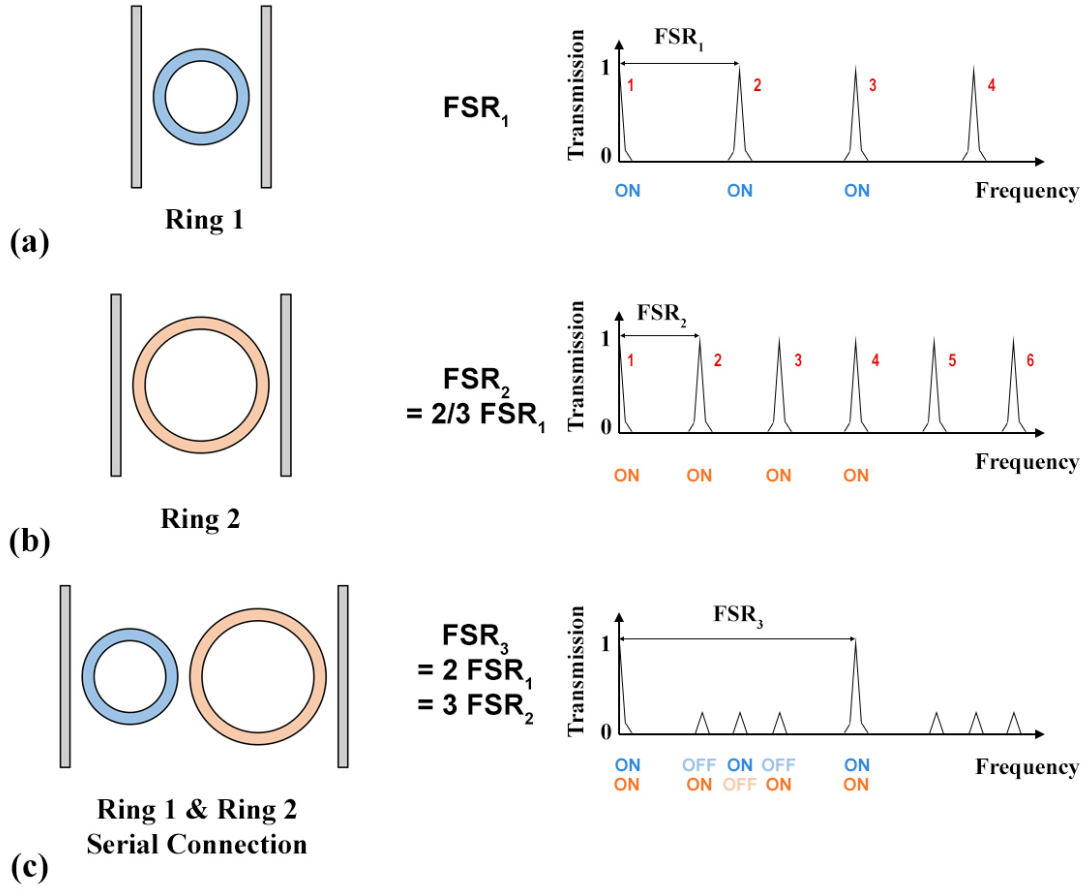

FIGURE 6.9: (a)-(b) Schematic representations and transmission plots of single-ring drop filters and (c) a Vernier filter comprised of two rings with a 2:3 circumference ratio connected in series.

A FSR spanning ∼40 nm cannot be easily achieved by a single ring, as its circumference would have to be smaller than 16 μm and this would introduce significant bend losses. The technique used to expand the FSR in a ring structure is based on the Vernier principle. As shown in Fig. 6.9, the use of two serially connected rings that exhibit a FSR ratio of $\frac{FSR_1}{FSR_2} = \frac{M}{N}$ can effectively result in a structure with FSR equal to $N \cdot FSR_1$ or $M \cdot FSR_2$. This is clearer if the frequency plot in Fig. 6.9 (c) is observed, where the drop port of the two-ring structure can be considered as an AND gate that

exhibits transmission equal to unity only at the wavelengths for which light enters both rings. Therefore, by suppressing certain resonant peaks, a large effective FSR can be achieved with relatively large ring structures whose bend loss values are not prohibitive for fabrication.

Based on the Vernier principle and the restrictions on the bend radius, the three types of ring filters that were designed are shown in Fig. 6.10. The first two types involve rings of circumference L_1 and L_2 equal to 45.416 μm and 60.554 μm respectively, using a 3:4 length ratio to expand the FSR of the total device to ∼40 nm. The second type uses 2 rings of each length in order to improve the suppression of the undesired resonance peaks. However, it is noted that this translates to additional heaters and the requirement for careful tuning of the 4 rings so that they are aligned in the wavelength axis. The third type also uses the 4-ring configuration, where the circumferences are equal to 71.416 μm and 85.700 μm that correspond to a 5:6 length ratio. This configuration provides better tunability to the central wavelength of the filter, as explained in the study of its transfer function in the following paragraph.

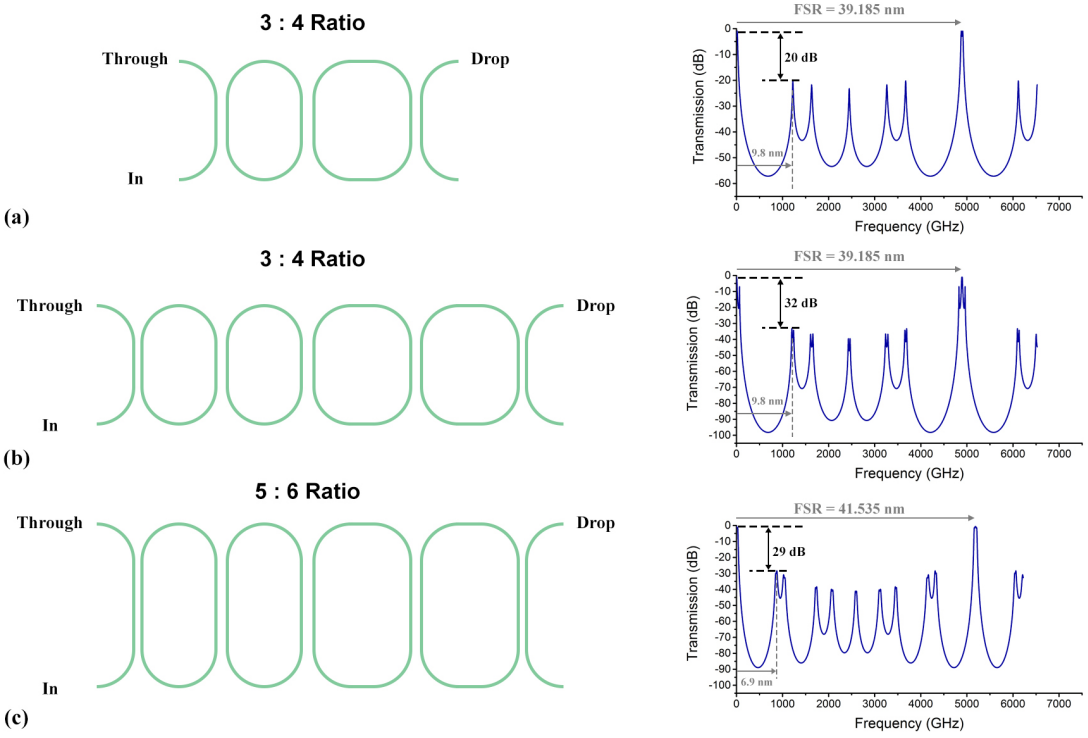

FIGURE 6.10: Schematic representations and transmission plots of (a) a two-ring 3:4-ratio filter, (b) a four-ring 3:4-ratio filter, (c) a four-ring 5:6-ratio filter.

In order to calculate the coupling gaps between the rings, the filters were modelled through a MATLAB routine that used the analysis described in [177]. This model is based on purely analytic formulations of the building blocks comprising such structures: optical couplers and waveguide sections. The transfer functions of the drop filters were therefore evaluated for different values of the coupling gap parameters and an optimum

solution in terms of undesired resonant peak suppression was selected. It is noted that the filters were considered to be symmetrical, meaning that some coupling gaps were assumed to be equal, as shown in Fig. 6.10. The selected optimum values that were used in the design are listed in Table 6.2. The corresponding transfer functions for these configurations are illustrated in Fig. 6.10. The 5 and 9 suppressed resonant peaks are apparent in the 3:4-ratio and 5:6-ratio filters respectively. The improvement in the suppression caused by introducing the additional ring resonators can be quantified by calculating the power ratio between the first and second peaks $R = \frac{P_{firstpeak}}{P_{secondpeak}}$ in the 3:4-ratio plots, where R is equal to 20 dB for the 2-ring filter and 32 dB for the 4-ring filter. The same ratio is 29 dB for the 5:6-ratio 4-ring filter.

TABLE 6.2: **Optimum gap values for the three filter configurations**

Configuration	Gap Values (nm) (left to right)
2-Ring, 3:4 Ratio	250, 444, 250
4-Ring, 3:4 Ratio	250, 387, 250, 387, 250
4-Ring, 5:6 Ratio	275, 450, 450, 450, 275

Another interesting parameter in the Vernier filters is the minimum FSR value $min(FSR)$ of the two rings, as it expresses the wavelength span that must be covered by the tuning heaters in order to enable centring the filter at any wavelength in the 40-nm band. To clarify, shifting both rings in the wavelength axis by a value greater than $min(FSR)$ is a redundant operation, as the same result can be achieved if the two rings are detuned in relation to each other and set so that the first and second suppressed peaks align with each other in wavelength. This way, the transfer function will effectively be offset by $min(FSR)$ by only heating half the rings in the structure by a smaller amount than the one corresponding to $min(FSR)$. This shows the improvement introduced by the 5:6-ratio 4-ring filter, which shows a $min(FSR)$ of 6.9 nm (864 GHz), while the value for the 3:4-ratio ones is 9.8 nm (1223 GHz).

Based on the discussions in the previous paragraphs, wavelength converter devices with variations of the nonlinear waveguide and the filter components were designed on the same layout. Even though measurements on fabricated devices could not be conducted due to the time constraints of this PhD project, a number of considerations regarding future measurements on the first set of devices are outlined below.

One factor that needs to be taken into account during the first characterisation process is the misalignment of the resonance wavelengths among the rings that comprise the Vernier filters. Although the FSR ratios are likely to match the predicted values, the positions of the resonance wavelengths of each ring will be arbitrary and therefore an appropriate initial tuning must be conducted. This can be achieved by tuning each heater individually while measuring the filter transfer function and observing its shape change, in order to match the shapes illustrated on the right half of Fig. 6.10.

Another consideration is the effect of heating on the coupling condition of the rings. The heating filaments are designed to only cover the ring sections that are away from their coupling points, so that they can only detune the transmission in wavelength. However no heat dissipation simulations were conducted and the application of voltage on the heater filaments could potentially alter the refractive index of the waveguides near the coupling points, thus modifying the coupling condition of the rings. This can be investigated through transfer function measurements of heater-equipped standalone ring structures that were drawn on the layout for testing purposes.

Lastly, the use of a high-power pump during the operation of the device might cause a temperature change in the bus waveguide of the filter and therefore affect the coupling condition of the first ring of the structure. A measurement of the power coupling value under different input optical powers can be initially conducted in test coupler structures that are included in the layout.

6.4 Conclusion

This chapter focused on FWM-based wavelength conversion, as an all-optical operation useful for applications involving telecommunication signals. In particular, the implementation of wavelength conversion using nonlinear silicon waveguides was investigated and discussed through experimental measurements and device modelling.

The first section reported the characterisation of a fabricated silicon rib waveguide in terms of nonlinearity, while the second section presented the experimental results of a wavelength conversion system that was built to incorporate the integrated waveguide as the nonlinear component. The main results included the wavelength conversion of a 40-Gbit/s 16-QAM signal with an OSNR penalty of 1.4 dB at a BER = 10^{-5}, indicating that conventional silicon rib waveguide structures can be good candidates in nonlinear processing applications for signals of complex modulation formats, while exhibiting low cost and high yield in their fabrication procedure.

The third section presented a design strategy for the full integration of a wavelength conversion system on a SOI platform, where a nonlinear component is used in conjunction with a filter. The layout drawn for the device fabrication was described, with comments and discussion on the requirements for each block of the system. First, the design of a nonlinear waveguide that incorporated a p-i-n junction for carrier extraction was described, aiming to address the problem of free carrier absorption present in high-power nonlinear applications. Next, several types of Vernier ring filters were proposed and analytically modelled to provide transmission plots and specifications that are useful in the wavelength conversion application. All the layouts were aligned with the design rules set by the CORNERSTONE multi-project-wafer (MPW) programme offered by the Silicon Photonics group at the University of Southampton.

Chapter 7

Conclusions

This project focused on investigating different applications of silicon photonics in a telecommunications system, through the design and characterisation of several key components. The choice of topics and the organisation of the conducted design and experimental work was determined to a great extent by the larger framework of the Silicon Photonics for Future Systems (SPFS) project, which targeted high-capacity transceiver applications. Under this consideration, several experiments were based on already available fabricated devices for such a system, whose design had been initiated at an earlier stage of the SPFS project, while others related to novel functionalities that were developed during this PhD project. It must be noted that the experimental work was coordinated according to the availability of fabricated devices, while some of the proposed designs did not reach the laboratory testing stage due to fabrication lead time restrictions.

In particular, Chapter 3 presented a novel device that targeted an application that relates to the interface of multi-mode fibres with a silicon photonic circuit. Building silicon photonic components for mode conversion functionalities was motivated by the recent research interest in leveraging SDM to increase the capacity of optical communication links. The chapter reported the design of a mode order converter incorporated in a grating coupler through extensive simulation work and experimental measurements. The grating pattern was apodised to improve the coupling efficiency to an optical fibre, while appropriately offsetting one side of the groove set with respect to the other induced the π phase change required to convert the mode order. In particular, a conversion of the TE_0 mode to the LP_{11} mode was demonstrated for the first time in a fabricated silicon device that makes use of this concept, while the characterisation measurements showed a -3.1-dB coupling efficiency to a commercial two-mode fibre and a conversion penalty of 1.3 dB. Far-field profile patterns were also recorded to verify the mode conversion.

Chapters 4 and 5 involved experimental work on fabricated modulator devices to investigate their suitability for comb generation and for data transmission. Chapter 4 focused

on the comb spectra that can be generated by a RRM driven by appropriately tailored electrical signals. A theoretical analysis of the RRM as a frequency comb generator was investigated for the first time in control theory nomenclature, with results on how the ring coupling condition and the phase difference of two input sinusoidal signals affect the comb shape. Next, the experimental implementation of this concept was reported using a fabricated RRM and the generation of five frequency tones at a spacing of 10 GHz with a power margin of 0.7 dB was presented. The behaviour of the RRM as a comb generator was studied and discussed through transfer function measurements and comb spectra measured for different applied bias voltages. The coherence of the comb lines was another parameter that was tested and verified by a time-domain measurement of the output which revealed a series of transform-limited pulses. These results proved that an on-chip comb source can be built in silicon with a conventional low-cost ring modulator that benefits from a small footprint, provided some complexity in the electronics is allowed in the design of the RF input (a dual-tone signal).

Chapter 5 focused on the parameter of linearity in MZI-based modulators. The advantages of the highly-linear MZM that was fabricated and characterised were verified through the transmission of data in medium-reach links via advanced modulation format signals. In particular, PAM-4 and DMT data were transmitted over 20 and 40 km of SMF and recovered by a direct detection receiver, showing BERs below the FEC limit ($3.8 \cdot 10^{-3}$). These transmissions corresponded to datarates of 40 Gb/s and 49.6 Gb/s respectively, exhibiting the highest spectral efficiency value (5 b/s/Hz) in an IM-DD link served by a silicon photonic modulator for the case of DMT modulation. A subsequent study of a tunable-linearity modulator design based on the RAMZI configuration was reported through analytical modelling. In its comparison to the conventional MZM topology with the same modulation depth, a ∼10 dB increase in SFDR was observed, while its implementation on the SOI platform was discussed.

Finally, Chapter 6 studied the use of silicon nonlinearity to implement all-optical wavelength conversion in a communication system. This was conducted by experimentally demonstrating the conversion in a silicon waveguide and by proposing an extended version of such an integrated device with an additional filtering operation. The effect of Four-Wave Mixing in a silicon rib waveguide allowed an optical signal containing 16-QAM data at a rate of 40 Gb/s to be copied to another wavelength by launching a high-power pump into the structure. BER measurements of the original and the converted signal showed an OSNR penalty of 1.4 dB at a BER value of 10^{-5} at the receiver. These rib-type structures that show relatively low sensitivity and low cost in their fabrication were proven to be good choices for the implementation of nonlinear processing of complex modulated data. An additional novel design for an integrated wavelength converter was presented, where the FWM-based conversion is accompanied by a filtering operation, so that the pump and the original signal components are not present at the output of the final device, for direct use in a communication application. This was

presented in the form of fabrication layouts for the two elements. The first one consisted of a rib-type nonlinear waveguide equipped with a p-i-n junction to extract the free carriers that introduce nonlinear loss at high powers. As regards the filter, several types of Vernier ring filters were proposed, based on their modelled transfer functions and the required specifications.

7.1 Future Work

The work reported in this thesis is part of the larger SPFS project and the investigation of the reported applications is tied to the on-going device development processes that are carried out in numerous successive cycles. Considering the relatively long fabrication lead time for silicon photonic components, especially when active circuit elements are involved, several design activities were not finalised within the time constraints of this PhD project. Therefore, there is room for further study and experimental testing in the research topics that were described in this thesis.

Regarding the grating coupler work in Chapter 3, the first step that could be tested would be to incorporate the grating into a mode multiplexing circuit composed of multimode waveguides. A number of on-chip mode multiplexers have already been reported [74–76] and the mode-converting grating interface can be used to provide the excitation of higher-order waveguide modes when operated in a fibre-to-chip configuration. The incorporation of the device into such circuits can open the path for the design of different functionalities, involving switching between modes both on-chip and in a fibre. The challenges in this concept would involve the design of the transition between the 20-μm-wide grating coupler and the multimode waveguides, which are typically 1-μm-wide if the support of only the first two modes is desired. An appropriate taper would have to be designed in order to avoid any mode mixing within the transition section. Lastly, another further step would be the fabrication of mode-converting grating couplers that can excite modes of even higher order (e.g. LP_{21}), such as in the design simulated in [81].

Chapter 4 reported the generation of a frequency comb using a single ring resonator modulator. The obvious next step would be to use a structure containing several ring modulators in cascade. The concept would be to generate a comb with the first RRM and send it to the subsequent modulators, whose resonance wavelengths would be detuned relative to the first RRM and aligned to one of the generated harmonics. This way, the additional RRMs would expand the comb span. Another design that could be envisioned is a ring modulator with a FSR equal to the RF modulating frequency used for the comb generation. This would lead to the generated harmonics successively entering into the ring cavity and experiencing a cascaded modulation effect in a single ring structure. The challenge in this design is that the required FSR value would require a large enough ring,

which would also increase the round-trip losses. However, it has previously been reported in integrated $LiNbO_3$ [87] and would merit investigation in silicon devices. Lastly, the concept proposed in [178] which involves first the generation of a comb through an E/O modulator and then its expansion through the FWM effect in a nonlinear component could be tested on a silicon RRM connected to a nonlinear silicon waveguide. The challenge anticipated in the operation of such a device would be the potential thermal detuning of the ring in case the optical carrier launched to it is relatively high-power in order for the FWM effect to take place in the nonlinear waveguide.

Regarding the topic of linear modulators (Chapter 5), the fabrication process of the RAMZI modulator designs that were reported had not concluded by the time of writing of this thesis. Therefore, when the final devices are fabricated, they will have to be experimentally characterised in terms of linearity to verify the trends of the Fundamental and IMD3 components that were predicted in Section 5.3.2 (Fig. 5.19). The tunability of their linearity can also be tested through operation of the heaters. As a final test, transmission experiments can be carried out using PAM-4- and DMT-modulated data in order to investigate the performance of such modulators in telecommunication systems. Lastly, another research path towards improving the linearity of Mach–Zehnder modulators can be a further optimisation of the p-n junction design through simulations in order to provide a more linear electro-optic conversion function, regardless of the device topology. An investigation on the effect of the p-n junction on modulator linearity has already been reported [67].

Finally, the wavelength converter device proposed in Chapter 6 was not investigated through measurements on a fabricated device. Therefore, characterisation measurements of coupler and single-ring test structures are the first step in implementing the wavelength conversion experiment in order to determine the filter transfer function shapes and the effects of the heaters on them. The experiment can then be conducted by converting QAM data, while the order of the QAM symbols that can be received without errors would be based on the output power level of the idler. The demonstration of an operational wavelength converter that is fully integrated in silicon would be the first report of its kind in the literature.

The following section outlines the scientific contribution of this PhD project to the research literature.

List of Publications and Conference Proceedings

[1] A. Xomalis, D. Piccinotti, A. Karvounis, I. Demirtzioglou, V. Savinov, B. Gholipour, J.-Y. Ou, Y. Jung, E. Plum, P. Petropoulos *et al.*, "Merging photonic metamaterial and optical fiber technologies," in *Integrated Photonics Research, Silicon and Nanophotonics,* (Optical Society of America, 2017), pp. ITh1B–5.

[2] A. Xomalis, Y. Jung, I. Demirtzioglou, V. Nalla, E. Plum, K. F. MacDonald, P. Petropoulos, D. J. Richardson, and N. I. Zheludev, "Dissipative optical switch for coherent fibre networks with 100 thz bandwidth," in *The European Conference on Lasers and Electro-Optics,* (Optical Society of America, 2017), p. CI_5_2.

[3] X. Ruan, K. Li, D. J. Thomson, C. Lacava, F. Meng, I. Demirtzioglou, P. Petropoulos, Y. Zhu, G. T. Reed, and F. Zhang, Optics express **25**, 19332 (2017).

[4] C. Lacava, I. Demirtzioglou, I. Cardea, A. Khoja, K. Li, D. Thomson, X. Ruan, F. Zhang, G. Reed, D. Richardson *et al.*, "Spectrally efficient dmt transmission over 40 km smf using an electrically packaged silicon photonic intensity modulator," in *2017 European Conference on Optical Communication (ECOC),* (IEEE, 2017), pp. 1–3.

[5] C. Lacava, I. Cardea, I. Demirtzioglou, A. Khoja, L. Ke, D. Thomson, X. Ruan, F. Zhang, G. Reed, D. Richardson *et al.*, Optics express **25**, 29798 (2017).

[6] C. Lacava, D. Thomson, K. Li, I. Demirtzioglou, A. Shakoor, D. Richardson, F. Zhang, G. Reed, and P. Petropoulos, "Silicon photonic modulators for high speed optical analog links," in *Photonics in Switching,* (Optical Society of America, 2017), pp. PW2D–3.

[7] A. Xomalis, I. Demirtzioglou, E. Plum, Y. Jung, V. Nalla, C. Lacava, K. F. MacDonald, P. Petropoulos, D. J. Richardson, and N. I. Zheludev, Nature communications **9**, 182 (2018).

[8] I. Demirtzioglou, C. Lacava, K. R. Bottrill, D. J. Thomson, G. T. Reed, D. J. Richardson, and P. Petropoulos, Optics express **26**, 790 (2018).

[9] I. Demirtzioglou, A. Xomalis, E. Plum, Y. Jung, C. Lacava, K. F. MacDonald, P. Petropoulos, D. J. Richardson, and N. I. Zheludev, "A fiberized metamaterial device for ultrafast control of coherent optical signals," in *Optical Fiber Communication Conference,* (Optical Society of America, 2018), pp. Tu2J–3.

[10] A. Xomalis, I. Demirtzioglou, Y. Jung, E. Plum, C. Lacava, P. Petropoulos, D. J. Richardson, and N. I. Zheludev, Applied Physics Letters **113**, 051103 (2018).

[11] A. Xomalis, I. Demirtzioglou, Y. Jung, E. Plum, C. Lacava, P. Petropoulos, D. J. Richardson, and N. I. Zheludev, APL Photonics **4**, 046102 (2019).

[12] I. Demirtzioglou, C. Lacava, A. Shakoor, A. Khokhar, Y. Jung, D. Thomson, and P. Petropoulos, "Silicon grating coupler for mode order conversion," in *CLEO: Applications and Technology,* (Optical Society of America, 2019), pp. JTh2A–74.

[13] I. Demirtzioglou, C. Lacava, A. Shakoor, A. Khokhar, Y. Jung, D. J. Thomson, and P. Petropoulos, Photonics Research **7**, 1036 (2019).

[14] K. R. Bottrill, M. A. Ettabib, I. Demirtzioglou, R. Marchetti, C. Lacava, F. Parmigiani, D. J. Richardson, and P. Petropoulos, Laser & Photonics Reviews p. 1900007.

Bibliography

[1] K. Kao and G. A. Hockham, "Dielectric-fibre surface waveguides for optical frequencies," in *Proceedings of the Institution of Electrical Engineers,* , vol. 113 (IET, 1966), pp. 1151–1158.

[2] T. Miya, Y. Terunuma, T. Hosaka, and T. Miyashita, Electronics Letters **15**, 106 (1979).

[3] R. J. Mears, L. Reekie, I. Jauncey, and D. N. Payne, Electronics Letters **23**, 1026 (1987).

[4] E. Desurvire, J. R. Simpson, and P. Becker, Optics letters **12**, 888 (1987).

[5] A. Chraplyvy, A. Gnauck, R. Tkach, and R. Derosier, IEEE photonics technology letters **5**, 1233 (1993).

[6] P. J. Winzer and R.-J. Essiambre, Journal of Lightwave Technology **24**, 4711 (2006).

[7] F. Derr, Journal of Lightwave Technology **10**, 1290 (1992).

[8] H. Sun, K.-T. Wu, and K. Roberts, Optics Express **16**, 873 (2008).

[9] E. Agrell, M. Karlsson, A. Chraplyvy, D. J. Richardson, P. M. Krummrich, P. Winzer, K. Roberts, J. K. Fischer, S. J. Savory, B. J. Eggleton *et al.*, Journal of Optics **18**, 063002 (2016).

[10] P. Sillard, Optical Fiber Technology **17**, 495 (2011).

[11] D. Richardson, J. Fini, and L. E. Nelson, Nature Photonics **7**, 354 (2013).

[12] P. J. Winzer and D. T. Neilson, Journal of Lightwave Technology **35**, 1099 (2017).

[13] R. Soref and J. Lorenzo, Electronics Letters **21**, 953 (1985).

[14] G. T. Reed, W. R. Headley, and C. J. Png, "Silicon photonics: The early years," in *Optoelectronic Integration on Silicon II,* , vol. 5730 (International Society for Optics and Photonics, 2005), pp. 1–18.

[15] A. Rickman, Nature Photonics **8**, 579 (2014).

[16] X. Chen, M. M. Milosevic, S. Stanković, S. Reynolds, T. D. Bucio, K. Li, D. J. Thomson, F. Gardes, and G. T. Reed, Proceedings of the IEEE **106**, 2101 (2018).

[17] D. Thomson, A. Zilkie, J. E. Bowers, T. Komljenovic, G. T. Reed, L. Vivien, D. Marris-Morini, E. Cassan, L. Virot, J.-M. Fédéli *et al.*, Journal of Optics **18**, 073003 (2016).

[18] H. Yu, J. Doylend, W. Lin, K. Nguyen, W. Liu, D. Gold, A. Dahal, C. Jan, R. Herrick, G. A. Ghiurcan *et al.*, "100gbps cwdm4 silicon photonics transmitter for 5g applications," in *Optical Fiber Communication Conference,* (Optical Society of America, 2019), pp. W3E–4.

[19] P. De Dobbelaere, G. Armijo, J. Balardeta, B. Chase, Y. Chi, A. Dahl, Y. De Koninck, S. Denton, M. Eker, S. Fathpour *et al.*, "Silicon-photonics-based optical transceivers for high-speed interconnect applications," in *Next-Generation Optical Networks for Data Centers and Short-Reach Links III,* , vol. 9775 (International Society for Optics and Photonics, 2016), p. 977503.

[20] L. Chen, C. Doerr, R. Aroca, S. Park, J. Geyer, T. Nielsen, C. Rasmussen, and B. Mikkelsen, "Silicon photonics for 100g-and-beyond coherent transmissions," in *Optical Fiber Communication Conference,* (Optical Society of America, 2016), pp. Th1B–1.

[21] F. Bœuf, S. Cremer, E. Temporiti, M. Fere, M. Shaw, N. Vulliet, B. Orlando, D. Ristoiu, A. Farcy, T. Pinguet *et al.*, "Recent progress in silicon photonics r&d and manufacturing on 300mm wafer platform," in *2015 Optical Fiber Communications Conference and Exhibition (OFC),* (IEEE, 2015), pp. 1–3.

[22] I. Demirtzioglou, C. Lacava, A. Shakoor, A. Khokhar, Y. Jung, D. Thomson, and P. Petropoulos, "Silicon grating coupler for mode order conversion," in *CLEO: Applications and Technology,* (Optical Society of America, 2019), pp. JTh2A–74.

[23] I. Demirtzioglou, C. Lacava, A. Shakoor, A. Khokhar, Y. Jung, D. J. Thomson, and P. Petropoulos, Photonics Research **7**, 1036 (2019).

[24] I. Demirtzioglou, C. Lacava, K. R. Bottrill, D. J. Thomson, G. T. Reed, D. J. Richardson, and P. Petropoulos, Optics express **26**, 790 (2018).

[25] C. Lacava, I. Demirtzioglou, I. Cardea, A. Khoja, K. Li, D. Thomson, X. Ruan, F. Zhang, G. Reed, D. Richardson *et al.*, "Spectrally efficient dmt transmission over 40 km smf using an electrically packaged silicon photonic intensity modulator," in *2017 European Conference on Optical Communication (ECOC),* (IEEE, 2017), pp. 1–3.

[26] C. Lacava, I. Cardea, I. Demirtzioglou, A. Khoja, L. Ke, D. Thomson, X. Ruan, F. Zhang, G. Reed, D. Richardson *et al.*, Optics express **25**, 29798 (2017).

[27] I. Demirtzioglou, C. Lacava, W. Yang, M. Ettabib, Y. Yu, and P. Petropoulos, (2016).

[28] G. P. Agrawal, *Fiber-optic communication systems*, vol. 222 (John Wiley & Sons, 2012).

[29] L. Chrostowski and M. Hochberg, *Silicon photonics design: from devices to systems* (Cambridge University Press, 2015).

[30] T. Barwicz and H. A. Haus, Journal of Lightwave Technology **23**, 2719 (2005).

[31] L. Jia, M. Geng, L. Zhang, L. Yang, P. Chen, and Y. Liu, Chinese Optics Letters **8**, 485 (2010).

[32] R. Marchetti, V. Vitali, C. Lacava, I. Cristiani, B. Charbonnier, V. Muffato, M. Fournier, and P. Minzioni, Optics express **25**, 9761 (2017).

[33] G. P. Agrawal, "Nonlinear fiber optics," in *Nonlinear Science at the Dawn of the 21st Century,* (Springer, 2000), pp. 195–211.

[34] Q. Lin, O. J. Painter, and G. P. Agrawal, Optics express **15**, 16604 (2007).

[35] R. Soref and B. Bennett, IEEE journal of quantum electronics **23**, 123 (1987).

[36] K. Hammani, M. A. Ettabib, A. Bogris, A. Kapsalis, D. Syvridis, M. Brun, P. Labeye, S. Nicoletti, D. J. Richardson, and P. Petropoulos, Optics express **21**, 16690 (2013).

[37] C. Lacava, S. Stankovic, A. Z. Khokhar, T. D. Bucio, F. Gardes, G. T. Reed, D. J. Richardson, and P. Petropoulos, Scientific Reports **7**, 22 (2017).

[38] B. B. Bakir, A. V. De Gyves, R. Orobtchouk, P. Lyan, C. Porzier, A. Roman, and J.-M. Fedeli, IEEE Photonics Technology Letters **22**, 739 (2010).

[39] P. Cheben, J. H. Schmid, S. Wang, D.-X. Xu, M. Vachon, S. Janz, J. Lapointe, Y. Painchaud, and M.-J. Picard, Optics express **23**, 22553 (2015).

[40] R. Marchetti, C. Lacava, L. Carroll, K. Gradkowski, and P. Minzioni, Photonics Research **7**, 201 (2019).

[41] P. P. Ewald, Annalen der physik **369**, 253 (1921).

[42] D. Vermeulen, Y. De Koninck, Y. Li, E. Lambert, W. Bogaerts, R. Baets, and G. Roelkens, "Reflectionless grating coupling for silicon-on-insulator integrated circuits," in *8th IEEE International Conference on Group IV Photonics,* (IEEE, 2011), pp. 74–76.

[43] N. Na, H. Frish, I.-W. Hsieh, O. Harel, R. George, A. Barkai, and H. Rong, Optics letters **36**, 2101 (2011).

[44] D. Taillaert, P. Bienstman, and R. Baets, Optics letters **29**, 2749 (2004).

[45] S. K. Selvaraja, D. Vermeulen, M. Schaekers, E. Sleeckx, W. Bogaerts, G. Roelkens, P. Dumon, D. Van Thourhout, and R. Baets, "Highly efficient grating coupler between optical fiber and silicon photonic circuit," in *2009 Conference on Lasers and Electro-Optics and 2009 Conference on Quantum electronics and Laser Science Conference,* (IEEE, 2009), pp. 1–2.

[46] F. Van Laere, G. Roelkens, M. Ayre, J. Schrauwen, D. Taillaert, D. Van Thourhout, T. F. Krauss, and R. Baets, Journal of lightwave technology **25**, 151 (2007).

[47] W. S. Zaoui, A. Kunze, W. Vogel, M. Berroth, J. Butschke, F. Letzkus, and J. Burghartz, Optics express **22**, 1277 (2014).

[48] Y. Ding, C. Peucheret, H. Ou, and K. Yvind, Optics letters **39**, 5348 (2014).

[49] G. Roelkens, D. Van Thourhout, and R. Baets, Optics Express **14**, 11622 (2006).

[50] R. Marchetti, C. Lacava, A. Khokhar, X. Chen, I. Cristiani, D. J. Richardson, G. T. Reed, P. Petropoulos, and P. Minzioni, Scientific reports **7**, 16670 (2017).

[51] G. T. Reed, G. Mashanovich, F. Y. Gardes, and D. Thomson, Nature photonics **4**, 518 (2010).

[52] G. Cocorullo and I. Rendina, Electronics Letters **28**, 83 (1992).

[53] J. Roth, O. Fidaner, E. Edwards, R. Schaevitz, Y.-H. Kuo, N. Helman, T. Kamins, J. Harris, and D. Miller, Electronics Letters **44**, 49 (2008).

[54] J. E. Roth, O. Fidaner, R. K. Schaevitz, Y.-H. Kuo, T. I. Kamins, J. S. Harris, and D. A. Miller, Optics Express **15**, 5851 (2007).

[55] J. Liu, M. Beals, A. Pomerene, S. Bernardis, R. Sun, J. Cheng, L. C. Kimerling, and J. Michel, Nature Photonics **2**, 433 (2008).

[56] P. Chaisakul, V. Vakarin, J. Frigerio, D. Chrastina, G. Isella, L. Vivien, and D. Marris-Morini, "Recent progress on ge/sige quantum well optical modulators, detectors, and emitters for optical interconnects," in *Photonics,* , vol. 6 (Multidisciplinary Digital Publishing Institute, 2019), p. 24.

[57] L. Mastronardi, M. Banakar, A. Khokhar, N. Hattasan, T. Rutirawut, T. D. Bucio, K. Grabska, C. Littlejohns, A. Bazin, G. Mashanovich *et al.*, Optics express **26**, 6663 (2018).

[58] R. S. Jacobsen, K. N. Andersen, P. I. Borel, J. Fage-Pedersen, L. H. Frandsen, O. Hansen, M. Kristensen, A. V. Lavrinenko, G. Moulin, H. Ou *et al.*, Nature **441**, 199 (2006).

[59] K. Alexander, J. P. George, J. Verbist, K. Neyts, B. Kuyken, D. Van Thourhout, and J. Beeckman, Nature communications **9**, 3444 (2018).

[60] W. Bogaerts, P. De Heyn, T. Van Vaerenbergh, K. De Vos, S. Kumar Selvaraja, T. Claes, P. Dumon, P. Bienstman, D. Van Thourhout, and R. Baets, Laser & Photonics Reviews **6**, 47 (2012).

[61] J. E. Heebner, V. Wong, A. Schweinsberg, R. W. Boyd, and D. J. Jackson, IEEE journal of quantum electronics **40**, 726 (2004).

[62] G. T. Reed, G. Z. Mashanovich, F. Y. Gardes, M. Nedeljkovic, Y. Hu, D. J. Thomson, K. Li, P. R. Wilson, S.-W. Chen, and S. S. Hsu, Nanophotonics **3**, 229 (2014).

[63] J. G. Proakis and M. Salehi, *Digital communications*, vol. 4 (McGraw-hill New York, 2001).

[64] J. M. Cioffi, Stanford online repository (2002).

[65] C. H. Cox, *Analog optical links: theory and practice* (Cambridge University Press, 2006).

[66] R. Soref and B. Bennett, IEEE Journal of Quantum Electronics **23**, 123 (1987).

[67] S. Yu and T. Chu, Photonics Research **5**, 124 (2017).

[68] H. Al-Raweshidy and S. Komaki, *Radio over fiber technologies for mobile communications networks* (Artech House, 2002).

[69] D. Marpaung, University of Twente (2009).

[70] K. Saitoh and S. Matsuo, Journal of Lightwave Technology **34**, 55 (2016).

[71] Y. Weng, X. He, and Z. Pan, Optical Fiber Technology **36**, 155 (2017).

[72] B. Wohlfeil, G. Rademacher, C. Stamatiadis, K. Voigt, L. Zimmermann, and K. Petermann, IEEE Photonics Technology Letters **28**, 1241 (2016).

[73] Y. Yu, M. Ye, and S. Fu, IEEE Photonics Technology Letters **27**, 1957 (2015).

[74] L.-W. Luo, N. Ophir, C. P. Chen, L. H. Gabrielli, C. B. Poitras, K. Bergmen, and M. Lipson, Nature communications **5**, 3069 (2014).

[75] B. Stern and M. Lipson, "High-bandwidth link with single laser input using silicon modulators and mode multiplexing," in *CLEO: Science and Innovations,* (Optical Society of America, 2016), pp. STu4G–5.

[76] X. Wu, K. Xu, C. Huang, C. Shu, and H. K. Tsang, "Mode division multiplexed 3× 28 gbit/s on-chip photonic interconnects," in *CLEO: Science and Innovations,* (Optical Society of America, 2016), pp. STu4G–6.

[77] A. Koonen, H.-S. Chen, H. van den Boom, and O. Raz, "Silicon photonic integrated mode multiplexer," in *2012 IEEE Photonics Society Summer Topical Meeting Series,* (IEEE, 2012), pp. 240–241.

[78] N. K. Fontaine, C. R. Doerr, M. A. Mestre, R. R. Ryf, P. J. Winzer, L. L. Buhl, Y. Sun, X. Jiang, and R. Lingle, "Space-division multiplexing and all-optical mimo demultiplexing using a photonic integrated circuit," in *OFC/NFOEC,* (IEEE, 2012), pp. 1–3.

[79] Y. Ding, H. Ou, J. Xu, and C. Peucheret, IEEE Photonics Technology Letters **25**, 648 (2013).

[80] C. R. Doerr, N. Fontaine, M. Hirano, T. Sasaki, L. Buhl, and P. Winzer, "Silicon photonic integrated circuit for coupling to a ring-core multimode fiber for space-division multiplexing," in *European Conference and Exposition on Optical Communications,* (Optical Society of America, 2011), pp. Th–13.

[81] M. Zhang, H. Liu, B. Wang, G. Li, and L. Zhang, IEEE Journal of Selected Topics in Quantum Electronics **24**, 1 (2018).

[82] C. T. Nadovich, W. D. Jemison, D. J. Kosciolek, and D. T. Crouse, Optics express **25**, 26861 (2017).

[83] D. J. Richardson, Science **330**, 327 (2010).

[84] A. Moscoso-Mártir, J. Müller, J. Hauck, N. Chimot, R. Setter, A. Badihi, D. E. Rasmussen, A. Garreau, M. Nielsen, E. Islamova *et al.*, Scientific reports **7**, 13857 (2017).

[85] A. Martin, J. Luff, D. Feng, and M. Asghari, "Technical challenges for 100gb/s silicon photonics transceivers for data center applications," in *Optical Fiber Communication Conference,* (Optical Society of America, 2016), pp. Th1F–1.

[86] A. L. Gaeta, M. Lipson, and T. J. Kippenberg, Nature Photonics **13**, 158 (2019).

[87] M. Zhang, B. Buscaino, C. Wang, A. Shams-Ansari, C. Reimer, R. Zhu, J. M. Kahn, and M. Lončar, Nature **568**, 373 (2019).

[88] T. J. Kippenberg, R. Holzwarth, and S. A. Diddams, science **332**, 555 (2011).

[89] J. Pfeifle, V. Brasch, M. Lauermann, Y. Yu, D. Wegner, T. Herr, K. Hartinger, P. Schindler, J. Li, D. Hillerkuss *et al.*, Nature photonics **8**, 375 (2014).

[90] P. Marin-Palomo, J. N. Kemal, M. Karpov, A. Kordts, J. Pfeifle, M. H. Pfeiffer, P. Trocha, S. Wolf, V. Brasch, M. H. Anderson *et al.*, Nature **546**, 274 (2017).

[91] C. Wang, M. Zhang, M. Yu, R. Zhu, H. Hu, and M. Loncar, Nature communications **10**, 978 (2019).

[92] Y. Okawachi, K. Saha, J. S. Levy, Y. H. Wen, M. Lipson, and A. L. Gaeta, Optics letters **36**, 3398 (2011).

[93] M. H. Pfeiffer, C. Herkommer, J. Liu, H. Guo, M. Karpov, E. Lucas, M. Zervas, and T. J. Kippenberg, Optica **4**, 684 (2017).

[94] S. Kim, K. Han, C. Wang, J. A. Jaramillo-Villegas, X. Xue, C. Bao, Y. Xuan, D. E. Leaird, A. M. Weiner, and M. Qi, Nature communications **8**, 372 (2017).

[95] P. Del'Haye, A. Schliesser, O. Arcizet, T. Wilken, R. Holzwarth, and T. J. Kippenberg, Nature **450**, 1214 (2007).

[96] P. Del'Haye, T. Herr, E. Gavartin, M. Gorodetsky, R. Holzwarth, and T. J. Kippenberg, Physical Review Letters **107**, 063901 (2011).

[97] B. Hausmann, I. Bulu, V. Venkataraman, P. Deotare, and M. Lončar, Nature Photonics **8**, 369 (2014).

[98] D. J. Wilson, K. Schneider, S. Hoenl, M. Anderson, T. J. Kippenberg, and P. Seidler, arXiv preprint arXiv:1808.03554 (2018).

[99] D. J. Wilson, S. Hönl, K. Schneider, M. Anderson, T. J. Kippenberg, and P. Seidler, "Gallium phosphide microresonator frequency combs," in *2018 Conference on Lasers and Electro-Optics (CLEO),* (IEEE, 2018), pp. 1–2.

[100] H. Jung, C. Xiong, K. Y. Fong, X. Zhang, and H. X. Tang, Optics letters **38**, 2810 (2013).

[101] X. Liu, C. Sun, B. Xiong, L. Wang, J. Wang, Y. Han, Z. Hao, H. Li, Y. Luo, J. Yan *et al.*, Applied Physics Letters **113**, 171106 (2018).

[102] N. Dupuis, C. R. Doerr, L. Zhang, L. Chen, N. J. Sauer, P. Dong, L. L. Buhl, and D. Ahn, Journal of Lightwave Technology **30**, 466 (2011).

[103] R. Slavík, S. G. Farwell, M. J. Wale, and D. J. Richardson, IEEE Photonics Technology Letters **27**, 217 (2014).

[104] A. M. Kaplan, A. Greenblatt, G. Harston, P. S. Cho, Y. Achiam, and I. Shpantzer, "Tunable frequency comb generator based on linbo3 ring resonator," in *Coherent Optical Technologies and Applications,* (Optical Society of America, 2006), p. CFC3.

[105] M. Yamamoto, Y. Tanaka, T. Shioda, T. Kurokawa, and K. Higuma, "Optical frequency comb generation using dual frequency optical phase modulation," in *Integrated Photonics Research and Applications,* (Optical Society of America, 2005), p. ITuF5.

[106] M. A. Soto, M. Alem, M. A. Shoaie, A. Vedadi, C.-S. Brès, L. Thévenaz, and T. Schneider, Nature communications **4**, 2898 (2013).

[107] M. Zhang, B. Buscaino, C. Wang, A. Shams-Ansari, C. Reimer, R. Zhu, J. Kahn, and M. Lončar, (2019).

[108] R. Wu, V. Supradeepa, C. M. Long, D. E. Leaird, and A. M. Weiner, Optics letters **35**, 3234 (2010).

[109] S. Ozharar, F. Quinlan, I. Ozdur, S. Gee, and P. Delfyett, IEEE Photonics Technology Letters **20**, 36 (2007).

[110] T. Sakamoto, T. Kawanishi, and M. Izutsu, Optics letters **32**, 1515 (2007).

[111] T. Sakamoto, T. Kawanishi, and M. Izutsu, Electronics Letters **43**, 1039 (2007).

[112] C. Weimann, P. Schindler, R. Palmer, S. Wolf, D. Bekele, D. Korn, J. Pfeifle, S. Koeber, R. Schmogrow, L. Alloatti *et al.*, Optics express **22**, 3629 (2014).

[113] Y. Xu, J. Lin, R. Dubé-Demers, S. LaRochelle, L. Rusch, and W. Shi, Optics letters **43**, 1554 (2018).

[114] J. Lin, H. Sepehrian, Y. Xu, L. A. Rusch, and W. Shi, IEEE Photonics Technology Letters **30**, 1495 (2018).

[115] L. R. Chen, "On-chip devices for optical and microwave signal processing," in *2018 Asia Communications and Photonics Conference (ACP),* (IEEE, 2018), pp. 1–3.

[116] K. Nagarjun, P. Raj, V. Jeyaselvan, S. K. Selvaraja, and V. Supradeepa, "Observation of novel optical and microwave power dependent effects in silicon microring modulator based frequency comb generators," in *Laser Resonators, Microresonators, and Beam Control XXI,* , vol. 10904 (International Society for Optics and Photonics, 2019), p. 109040S.

[117] P. Rabiei, arXiv preprint arXiv:1710.00770 (2017).

[118] K. R. Bottrill, M. A. Ettabib, I. Demirtzioglou, R. Marchetti, C. Lacava, F. Parmigiani, D. J. Richardson, and P. Petropoulos, Laser & Photonics Reviews p. 1900007.

[119] K. R. Bottrill, G. D. Hesketh, F. Parmigiani, P. Horak, D. J. Richardson, and P. Petropoulos, IEEE Photonics Technology Letters **26**, 2074 (2014).

[120] K. Bottrill, M. A. Ettabib, J. C. Gates, C. Lacava, F. Parmigiani, D. J. Richardson, and P. Petropoulos, "Flexible scheme for measuring chromatic dispersion based on interference of frequency tones," in *2017 Optical Fiber Communications Conference and Exhibition (OFC),* (IEEE, 2017), pp. 1–3.

[121] S. Preußler, N. Wenzel, and T. Schneider, IEEE Photonics Journal **6**, 1 (2014).

[122] S. Liu, K. Wu, L. Zhou, L. Lu, B. Zhang, G. Zhou, and J. Chen, IEEE Journal of Selected Topics in Quantum Electronics **26**, 1 (2019).

[123] G. Li, D. Lambert, J. Zyskind, J. Spann, M. Askari, G. Pickrell, M. Sodagar, and S. Krasulick, "100gb/s cwdm transmitter and receiver chips on a monolithic si-photonics platform," in *2016 IEEE 13th International Conference on Group IV Photonics (GFP),* (IEEE, 2016), pp. 164–165.

[124] H. Füser, A. L. Giesecke, A. Prinzen, S. Suckow, C. Porschatis, D. Schall, H. Lerch, M. M. Tarar, J. Bolten, T. Wahlbrink *et al.*, "56 gb/s wdm transmitter module based on silicon microrings using comb lasers," in *CLEO: QELS_Fundamental Science,* (Optical Society of America, 2015), pp. JTh2A–66.

[125] P. J. Winzer and R.-J. Essiambre, "Advanced optical modulation formats," in *Optical Fiber Telecommunications VB,* (Elsevier, 2008), pp. 23–93.

[126] C. R. Doerr, Frontiers in Physics **3**, 37 (2015).

[127] B. Jalali and S. Fathpour, Journal of lightwave technology **24**, 4600 (2006).

[128] H. Yu, M. Pantouvaki, J. Van Campenhout, D. Korn, K. Komorowska, P. Dumon, Y. Li, P. Verheyen, P. Absil, L. Alloatti *et al.*, Optics express **20**, 12926 (2012).

[129] T.-Y. Liow, K.-W. Ang, Q. Fang, J.-F. Song, Y.-Z. Xiong, M.-B. Yu, G.-Q. Lo, and D.-L. Kwong, IEEE Journal of Selected Topics in Quantum Electronics **16**, 307 (2010).

[130] N.-N. Feng, S. Liao, D. Feng, P. Dong, D. Zheng, H. Liang, R. Shafiiha, G. Li, J. E. Cunningham, A. V. Krishnamoorthy *et al.*, Optics express **18**, 7994 (2010).

[131] R. Ding, Y. Liu, Q. Li, Y. Yang, Y. Ma, K. Padmaraju, A. E.-J. Lim, G.-Q. Lo, K. Bergman, T. Baehr-Jones *et al.*, Optics communications **321**, 124 (2014).

[132] H. Yang, S. J. Lee, E. Tangdiongga, C. Okonkwo, H. P. van den Boom, F. Breyer, S. Randel, and A. Koonen, Journal of Lightwave Technology **28**, 352 (2010).

[133] I. Neokosmidis, T. Kamalakis, J. W. Walewski, B. Inan, and T. Sphicopoulos, Journal of Lightwave technology **27**, 4970 (2009).

[134] A. Khilo, C. M. Sorace, and F. X. Kärtner, Optics express **19**, 4485 (2011).

[135] S. Zhou, X. Li, L. Yi, Q. Yang, and S. Fu, Optics letters **41**, 1805 (2016).

[136] C. Zhang, P. A. Morton, J. B. Khurgin, J. D. Peters, and J. E. Bowers, Optica **3**, 1483 (2016).

[137] J. Cardenas, P. A. Morton, J. B. Khurgin, A. Griffith, C. B. Poitras, K. Preston, and M. Lipson, Optics express **21**, 22549 (2013).

[138] A. Gutierrez, J. Galan, J. Herrera, A. Brimont, D. Marris-Morini, J. Fedeli, L. Vivien, and P. Sanchis, "High linear ring-assisted mzi electro-optic silicon modulators suitable for radio-over-fiber applications," in *The 9th International Conference on Group IV Photonics (GFP),* (IEEE, 2012), pp. 57–59.

[139] A. Ayazi, T. Baehr-Jones, Y. Liu, A. E.-J. Lim, and M. Hochberg, Optics express **20**, 13115 (2012).

[140] J. Ding, S. Shao, L. Zhang, X. Fu, and L. Yang, Optics express **24**, 24641 (2016).

[141] X. Luo, X. Tu, J. Song, L. Ding, Q. Fang, T.-Y. Liow, M. Yu, and G.-Q. Lo, Optics express **21**, 16570 (2013).

[142] M. Streshinsky, A. Ayazi, Z. Xuan, A. E.-J. Lim, G.-Q. Lo, T. Baehr-Jones, and M. Hochberg, Optics express **21**, 3818 (2013).

[143] U. Gliese, S. Norskov, and T. Nielsen, IEEE Transactions on microwave theory and techniques **44**, 1716 (1996).

[144] H. Schmuck, Electronics Letters **31**, 1848 (1995).

[145] P. Merritt, R. P. Tatam, and D. A. Jackson, Journal of lightwave technology **7**, 703 (1989).

[146] P. Dong, J. Lee, Y.-K. Chen, L. L. Buhl, S. Chandrasekhar, J. H. Sinsky, and K. Kim, Journal of Lightwave Technology **34**, 79 (2016).

[147] Y. Kai, M. Nishihara, T. Tanaka, R. Okabe, T. Takahara, J. C. Rasmussen, H. Ishihara, K. Goi, and K. Ogawa, "130-gbps dmt transmission using silicon mach-zehnder modulator with chirp control at 1.55-μm," in *Optical Fiber Communication Conference,* (Optical Society of America, 2015), pp. Th4A–1.

[148] R. Li, D. Patel, E. El-Fiky, A. Samani, Z. Xing, M. Morsy-Osman, and D. V. Plant, Optics express **25**, 13222 (2017).

[149] Z. Liu, M. S. Erkilinc, B. Kelly, J. O'Carroll, R. Phelan, B. C. Thomsen, R. I. Killey, D. J. Richardson, P. Bayvel, and R. Slavík, "49 gbit/s direct-modulation and direct-detection transmission over 80 km smf-28 without optical amplification or filtering," in *ECOC 2016; 42nd European Conference on Optical Communication,* (VDE, 2016), pp. 1–3.

[150] P. Dong, X. Chen, K. Kim, S. Chandrasekhar, Y.-K. Chen, and J. H. Sinsky, Optics express **24**, 14208 (2016).

[151] X. Ruan, K. Li, D. J. Thomson, C. Lacava, F. Meng, I. Demirtzioglou, P. Petropoulos, Y. Zhu, G. T. Reed, and F. Zhang, Optics express **25**, 19332 (2017).

[152] B. B. Dingel, R. Madabhushi, and N. Madamopoulos, "Super-linear optical modulator technologies for optical broadband access network: Development and potential," in *Optical Transmission Systems and Equipment for WDM Networking IV,* , vol. 6012 (International Society for Optics and Photonics, 2005), p. 60120R.

[153] Q. Zhang, H. Yu, H. Jin, T. Qi, Y. Li, J. Yang, and X. Jiang, Journal of Lightwave Technology **36**, 3318 (2018).

[154] Y. Zhou, L. Zhou, M. Wang, Y. Xia, Y. Zhong, X. Li, and J. Chen, IEEE Photonics Journal **8**, 1 (2016).

[155] X. Xie, J. Khurgin, J. Kang, and F.-S. Chow, IEEE Photonics Technology Letters **15**, 531 (2003).

[156] B. Dingel, N. Madamopoulos, A. Prescod, and R. Madabhushi, Optics Communications **284**, 5578 (2011).

[157] B. Zhang, J. B. Khurgin, and P. A. Morton, IEEE Photonics Technology Letters **21**, 1621 (2009).

[158] H. Tazawa and W. H. Steier, IEEE Photonics Technology Letters **17**, 1851 (2005).

[159] R. Li, D. Patel, A. Samani, E. El-Fiky, Y. Wang, Z. Xing, L. Xu, and D. V. Plant, IEEE Photonics Journal **9**, 1 (2017).

[160] C. Doerr, L. Chen, T. Nielsen, R. Aroca, L. Chen, M. Banaee, S. Azemati, G. McBrien, S. Park, J. Geyer *et al.*, "O, e, s, c, and l band silicon photonics coherent modulator/receiver," in *2016 Optical Fiber Communications Conference and Exhibition (OFC),* (IEEE, 2016), pp. 1–3.

[161] D. Feng, B. J. Luff, S. Jatar, and M. Asghari, "Micron-scale silicon photonic devices and circuits," in *Optical Fiber Communication Conference,* (Optical Society of America, 2014), pp. Th4C–1.

[162] A. Ramaswamy, J. Roth, E. Norberg, R. Guzzon, J. Shin, J. Imamura, B. Koch, D. Sparacin, G. Fish, B. Lee *et al.*, "A wdm 4× 28gbps integrated silicon photonic transmitter driven by 32nm cmos driver ics," in *Optical Fiber Communication Conference,* (Optical Society of America, 2015), pp. Th5B–5.

[163] P. Minzioni, C. Lacava, T. Tanabe, J. Dong, X. Hu, G. Csaba, W. Porod, G. Singh, A. E. Willner, A. Almaiman *et al.*, Journal of Optics **21**, 063001 (2019).

[164] J. Wang and Y. Long, Sci. Bull **63**, 1267 (2018).

[165] S. Aleksić, Journal of Optical Communications and Networking **1**, 245 (2009).

[166] S. B. Yoo, Journal of Lightwave Technology **14**, 955 (1996).

[167] R. Adams, M. Spasojevic, M. Chagnon, M. Malekiha, J. Li, D. V. Plant, and L. R. Chen, Optics express **22**, 4083 (2014).

[168] M. Ettabib, C. Lacava, Z. Liu, A. Bogris, A. Kapsalis, M. Brun, P. Labeye, S. Nicoletti, D. Syvridis, D. Richardson *et al.*, Optics express **25**, 3252 (2017).

[169] D.-X. Xu, J. H. Schmid, G. T. Reed, G. Z. Mashanovich, D. J. Thomson, M. Nedeljkovic, X. Chen, D. Van Thourhout, S. Keyvaninia, and S. K. Selvaraja, IEEE Journal of Selected Topics in Quantum Electronics **20**, 189 (2014).

[170] C. Lacava, V. Pusino, P. Minzioni, M. Sorel, and I. Cristiani, Optics express **22**, 5291 (2014).

[171] R. Stolen and J. Bjorkholm, IEEE Journal of Quantum Electronics **18**, 1062 (1982).

[172] CORNERSTONE, https://www.cornerstone.sotonfab.co.uk/.

[173] A. Gajda, L. Zimmermann, M. Jazayerifar, G. Winzer, H. Tian, R. Elschner, T. Richter, C. Schubert, B. Tillack, and K. Petermann, Optics express **20**, 13100 (2012).

[174] A. Gajda, F. Da Ros, D. Vukovic, L. Zimmermann, C. Peucheret, B. Tillack, and K. Peterman, "High efficiency wavelength conversion of 40 gbps signals at 1550 nm in soi nano-rib waveguides using pin diodes," in *10th International Conference on Group IV Photonics,* (IEEE, 2013), pp. 160–161.

[175] R. Jones, H. Rong, A. Liu, A. W. Fang, M. J. Paniccia, D. Hak, and O. Cohen, Optics Express **13**, 519 (2005).

[176] H. Rong, A. Liu, R. Jones, O. Cohen, D. Hak, R. Nicolaescu, A. Fang, and M. Paniccia, Nature **433**, 292 (2005).

[177] R. Orta, P. Savi, R. Tascone, and D. Trinchero, IEEE Photonics Technology Letters **7**, 1447 (1995).

[178] M. Zhang, C. Reimer, L. He, R. Cheng, M. Yu, R. Zhu, and M. Loncar, "Microresonator frequency comb generation with simultaneous kerr and electro-optic nonlinearities," in *CLEO: QELS_Fundamental Science,* (Optical Society of America, 2019), pp. FF2D–3.